โครงสร้างทางอิเล็กทรอนิกส์สองมิติบนพื้นผิววัสดุโลหะทรานซิชันไดแชลโคเจไนด์โดยเทคนิคโฟโตอิมิชชันสเปกโทสโกปี

นายธนชาติ เอกนภากุล

TWO DIMENSIONAL ELECTRONIC STRUCTURES AT THE SURFACES OF TRANSITION METAL DICHALCOGENIDES MEASURED BY PHOTOEMISSION SPECTROSCOPY

Tanachat   Eknapakul

A Thesis Submitted in Partial Fulfillment of the Requirements for the

Degree of Doctor of Philosophy in Physics

Suranaree University of Technology

Academic Year 2015

TWO DIMENSIONAL ELECTRONIC STRUCTURES AT THE SURFACES OF TRANSITION METAL DICHALCOGENIDES MEASURED BY PHOTOEMISSION SPECTROSCOPY

Suranaree University of Technology has approved this thesis submitted in partial fulfillment of the requirements for the Degree of Doctor of Philosophy.

Thesis Examining Committee

_____

(Prof. Dr. Santi Maensiri)

Chairperson

_____

(Asst. Prof. Dr. Worawat Meevasana)

Member (Thesis Advisor)

_____

(Assoc. Prof. Dr. Prayoon Songsiriritthigul)

Member

_____

(Assoc. Prof. Dr. Sirichok Jungthawan)

Member

_____

(Assoc. Prof. Dr. Udomsilp Pinsook)

Member

_____

(Dr. Montree Sawangphruk)

Member

_____   _____

(Prof. Dr. Sukit Limpijumnong)   (Prof. Dr. Santi Maensiri)

Vice Rector for Academic Affairs   Dean of Institute of Science

and Innovation

ธนชาติ เอกนภากุล : โครงสร้างทางอิเล็กทรอนิกส์สองมิติบนพื้นผิววัสดุโลหะทรานซิชัน
ไดแชลโคเจไนด์โดยเทคนิคโฟโตอิมิชชันสเปกโทสโกปี (TWO DIMENSIONAL
ELECTRONIC STRUCTURES AT THE SURFACES OF TRANSITION METAL
DICHALCOGENIDES MEASURED BY PHOTOEMISSION SPECTROSCOPY)
อาจารย์ที่ปรึกษา : ผู้ช่วยศาสตราจารย์ ดร.วรวัฒน์ มีวาสนา, 146 หน้า.

โครงสร้างทางอิเล็กทรอนิกส์สองมิติที่เกิดในวัสดุแบบก้อนใหญ่ถูกพบว่าจะแสดงสมบัติ
แปลกใหม่ เช่น การแยกออกของสปินกับวงโคจรแบบรัชบาและแก๊สอิเล็กตรอนสองมิติ หลังจาก
การค้นพบกราฟีนในปี พ.ศ. 2548 มีการเพิ่มขึ้นของการศึกษาวัสดุสองมิติและวัสดุแบบชั้นเพื่อ
ค้นหาวัสดุที่สามารถนำมาประยุกต์ใช้งานได้เหนือกว่าอุปกรณ์ในปัจจุบัน วิทยานิพนธ์นี้แบ่ง
ออกเป็นสองส่วน คือ การศึกษาโครงสร้างทางอิเล็กทรอนิกส์สองมิติในวัสดุโลหะทรานซิชัน
ออกไซด์และการศึกษาเกี่ยวกับวัสดุโลหะทรานซิชันไดแชลโคเจไนด์แบบชั้น โครงสร้างทาง
อิเล็กทรอนิกส์ของวัสดุถูกศึกษาโดยใช้เทคนิคโฟโตอิมิชชันแบบแยกแยะเชิงมุมและการคำนวณ
ทางทฤษฎีถูกศึกษาโดยใช้ทฤษฎีฟังก์ชันความหนาแน่น

ส่วนแรกจะเน้นไปที่การศึกษาโครงสร้างทางอิเล็กทรอนิกส์สองมิติของวัสดุโลหะทรานซิ
ชันออกไซด์ ซึ่งการศึกษาในส่วนนี้มีความสำคัญเกี่ยวกับการทำความเข้าใจเทคนิคโฟโตอิมิชชัน
และเป็นพื้นฐานสำหรับโครงสร้างที่ซับซ้อนขึ้นในวัสดุโลหะทรานซิชันไดแชลโคเจไนด์ ในส่วนนี้
ได้ทำการศึกษาเกี่ยวกับการสร้างและควบคุมสมบัติของแก๊สอิเล็กตรอนสองมิติและการประยุกต์
เกี่ยวกับเซนเซอร์แสงของวัสดุ $SrTiO_3$ ประกอบกับการศึกษาโครงสร้างชั้นย่อยของแก๊สอิเล็กตรอน
สองมิติในวัสดุ $KTaO_3$ โดยผลการศึกษาพบว่าช่องว่างของออกซิเจน การสะสมของอิเล็กตรอนบน
พื้นผิวและสมบัติการมีขั้ว/ไม่มีขั้ว เป็นปัจจัยสำคัญเกี่ยวกับการเกิดโครงสร้างทางอิเล็กทรอนิกส์
สองมิติ

ส่วนที่สองจะมุ่งเน้นไปที่การศึกษาเกี่ยวกับวัสดุโลหะทรานซิชันไดแชลโคเจไนด์ ซึ่ง
ประกอบไปด้วยวัสดุ MoS_2 WSe_2 $PdTe_2$ และ $HfSe_2$ โดยเริ่มจากวัสดุ MoS_2 ซึ่งเป็นส่วนหลักของ
วิทยานิพนธ์และมีสมบัติที่น่าสนใจคือ วัสดุชนิดนี้มีการเปลี่ยนสมบัติจากประเภทช่องว่าง
แถบพลังงานแบบไม่ตรงเป็นประเภทช่องว่างแถบพลังงานแบบตรงเมื่อถูกทำให้บางลงจนเป็นแบบ
ผิวชั้นเดียว งานวิจัยนี้ได้แสดงกลวิธีใหม่ที่อาจจะสามารถใช้ในการเตรียมวัสดุผิวชั้นเดียวขนาด
ใหญ่โดยการสอดแทรกของโพแทสเซียมเข้าไปในพื้นผิวของวัสดุ MoS_2 จากการทดลองพบว่า
โครงสร้างทางอิเล็กทรอนิกส์มีการเปลี่ยนแปลงหลังจากการเจือด้วยโลหะแอลคาไลน์ ผลการ

ทดลองในวัสดุตัวอย่างแรกเริ่มแสดงให้เห็นว่าไม่มีหลักฐานการมีอยู่ของแถบตัวนำ และมีการ
ค้นพบการแยกออกของสปินกับวงโคจรขนาดใหญ่ที่แถบวาเลนซ์ประมาณ 180 มิลลิอิเลกตรอน
โวลท์ โดยหลังจากการเจือโพแทสเซียมลงบนผิวของวัสดุ MoS_2 แถบตัวนำสองมิติได้ถูกทำให้
ปรากฏขึ้นและสิ่งที่น่าสนใจอย่างมากคือ แถบตัวนำที่เกิดขึ้นอยู่ที่โมเมนตัมใกล้เคียงอย่างมากกับ
แถบวาเลนซ์ กล่าวได้ว่าวัสดุนี้มีการเปลี่ยนแปลงจากประเภทช่องว่างแถบพลังงานแบบไม่ตรงเป็น
ประเภทช่องว่างแถบพลังงานแบบตรง จากการศึกษาด้วยเทคนิคเอกซเรย์โฟโตอิมิชชัน สเปกโทส
โกปีควบคู่กับการคำนวณพลังงานก่อเกิดชี้ให้เห็นว่า อะตอมของโพแทสเซียมได้สอดแทรกเข้าไป
ในชั้นบนสุดของวัสดุ MoS_2 และแสดงสภาพเสมือนของผิวชั้นเดียว นอกจากนี้ยังพบว่าการคำนวณ
โดยใช้แบบจำลองการขยายตัวของระยะห่างระหว่างชั้นมีความสอดคล้องอย่างมากกับผลการ
ทดลอง ในส่วนที่สองจะเป็นการนำเสนอผลการทดลองเกี่ยวกับวัสดุโลหะทรานซิชันไดแชลโคเจ
ไนด์ชนิดต่างๆ ที่ได้เป็นส่วนหนึ่งของโครงการวิจัย เริ่มจากการศึกษาการแยกออกของสปินกับวง
โคจรในระบบที่ไม่มีสมมาตรแบบกลับและสมบัติการบีบอัดอิเล็กตรอนเชิงลบโดยการเจือด้วย
โลหะแอลคาไลน์ในวัสดุ WSe_2 นอกจากนี้ ผลการทดลองเบื้องต้นเกี่ยวกับการค้นพบจุดดิแรกสาม
มิติและการแยกออกของรัชบาแบบกลับในวัสดุ $PdTe_2$ ประกอบกับการพบแถบพลังงานสองมิติ
ของโซเดียมบนผิวของวัสดุ $HfSe_2$ จะถูกนำเสนอในลำดับสุดท้าย

สาขาวิชาฟิสิกส์   ลายมือชื่อนักศึกษา_____

ปีการศึกษา 2558   ลายมือชื่ออาจารย์ที่ปรึกษา_____

TANACHAT EKNAPAKUL : TWO DIMENSIONAL ELECTRONIC
STRUCTURES AT THE SURFACES OF TRANSITION METAL
DICHALCOGENIDES MEASURED BY PHOTOEMISSION
SPECTROSCOPY. THESIS ADVISOR : ASST. PROF.
WORAWAT MEEVASANA, Ph.D. 146 PP.

TWO-DIMENSIONAL ELECTRONIC STRUCTURE/TRANSITION METAL
DICHALCOGENIDES/ANGLE-RESOLVED PHOTOEMISSION
SPECTROSCOPY

Two-dimensional (2D) electronic structure detected in many materials are known to exhibit exotic properties, including the emergence of Rashba spin-orbit splitting and two-dimensional electron gases (2DEGs). Interestingly, after graphene was discovered in 2005, there have been a number of studies on 2D materials focusing on 2DEGs and layered compounds, searching for novel applications beyond the conventional ones. This thesis has been divided into two main parts; the study of 2D electronic structure observed in transition metal oxides (TMOs) and the study of layered-transition metal dichalcogenides (Layered-TMDs). The electronic structure of materials has been studied by the angle-resolved photoemission spectroscopy (ARPES) and the theoretical calculation has been done by density functional theory (DFT).

The first part focuses on the study of 2D electronic structure on TMOs. This study is very important which gives the essential knowledge prompting us to understand the electronic structures of TMDs. In this part, the creation and control of 2DEGs at the surface of $SrTiO_3$ have been studied. The subband structure of 2DEGs observed in $KTaO_3$ has also be studied to understand surface electron accumulation, and the polar/non-polar surface properties.

In the second part, the study of the layered-TMDs including MoS_2, WSe_2, $PdTe_2$ and $HfSe_2$ has been performed. Firstly, I will present the study of MoS_2 which is the main part of this thesis. MoS_2 exhibits a striking crossover from indirect to direct band gap while being thinned down to a monolayer. Here, we present the new way to prepare a large scale monolayer on MoS_2 surfaces by using potassium intercalation. Our ARPES result shows the change of electronic structure after dosing alkali metal at the sample surfaces. In pristine sample, we found the Fermi energy inside the gap and the large spin-orbit splitting at the valence band maximum (VBM) to be around 180 meV. After dosing of potassium, the 2D like state at the conduction band has emerged. Surprisingly, the conduction band minimum (CBM) appears to be nearly at the same momentum as the VBM, indicating the transition from indirect to direct band gap. The x-ray photoemission spectroscopy (XPS) data and the formation energy calculation claims the potassium intercalation process near the top layer giving the quasi-freestanding MoS_2 monolayer. Furthermore, the DFT calculation with c/a expansion is also in good agreement with the ARPES data. Secondly, I will give the brief information about the other layered-TMDs which I have participated as a part of projects. The strong spin-orbit spitting on inversion asymmetry system and the negative electron compressibility (NEC) by alkali metal doping have been described in WSe_2. The preliminary result of the discovery of 3D-Dirac point and inverted-Rashba splitting in $PdTe_2$ and the observation of 2D sodium bands formed at the surface of $HfSe_2$ have also been included.

School of Physics	Student's Signature _____
Academic Year 2015	Advisor's Signature _____

ACKNOWLEDGEMENTS

My thesis could not be accomplished without much help and support from many people. First and foremost, I am grateful to my advisor, Asst. Prof. Dr. Worawat Meevasana. It was my fortunate that I had a great chance to talk with him before I graduated with a bachelor's degree. This important time made me decide to join his research group for the Ph.D. program at SUT. It has been almost 6 years from that time up to now, I am very enjoyable and feel like the most luckiest student under his supervision as he is a very nice advisor for his kindness, dedication, and encouragement. I really appreciate for what he has given to me; for example, he gave me a chance to do the experiment in USA and learn many things from the top facilities in the world. Thus, I explored the wider world. With his understanding and patient, he always push me with the good attitude and scientific ideas to make me better. I will never regret for what I have learned so far.

I would like to thank Prof. Dr. Santi Maensiri, dean of institute of Science (SUT) and also my former advisor of undergraduate research project at Khon Kaen university. I think I may not be what I am today without him. He gave me an opportunity to work in the field of the condense matter. He always give me the right direction and positive aspect.

I am thankful to my co-advisor, Assoc. Prof. Dr. Sirichok Jungthawan. My work cannot be fulfilled without a great help from him. He always gives the advice for computational models. Surprisingly, he can perform all of the computational calculations in many aspects as we have discussed. Moreover, he also advises and suggests me many things about the work.

CONTENTS

CONTENTS (Continued)

CONTENTS (Continued)

CONTENTS (Continued)

LIST OF FIGURES

LIST OF FIGURES (Continued)

LIST OF FIGURES (Continued)

LIST OF FIGURES (Continued)

LIST OF FIGURES (Continued)

LIST OF FIGURES (Continued)

LIST OF FIGURES (Continued)

LIST OF FIGURES (Continued)

LIST OF FIGURES (Continued)

LIST OF FIGURES (Continued)

LIST OF ABBREVIATIONS

1D, 2D, 3D	One-dimension, Two-dimension, Three-dimension
2DEG	Two-Dimensional Electron Gas
ARPES	Angle-resolved photoemission spectroscopy
CBM	Conduction band minimum
CVD	Chemical vapor deposition
DFT	Density functional theory
EDC	Energy distribution curve
FET	Field effect transistor
IS	Inversion symmetry
LEED	Low energy electron diffraction
MBE	Molecular beam epitaxy
MDC	Momentum distribution curve
PES	Photoemission spectroscopy
SOI	Spin-orbit interaction
SOS	Spin-orbit splitting
TRS	Time-reversal symmetry
TMD	Transition metal dichalcogenide
TMO	Transition metal oxide
UHV	Ultra high vacuum

LIST OF ABBREVIATIONS (Continued)

UV   Ultraviolet light

VBM   Valence band maximum

vdW   Van der Waals

XPS   X-ray photoemission spectroscopy

XRD   X-ray diffraction
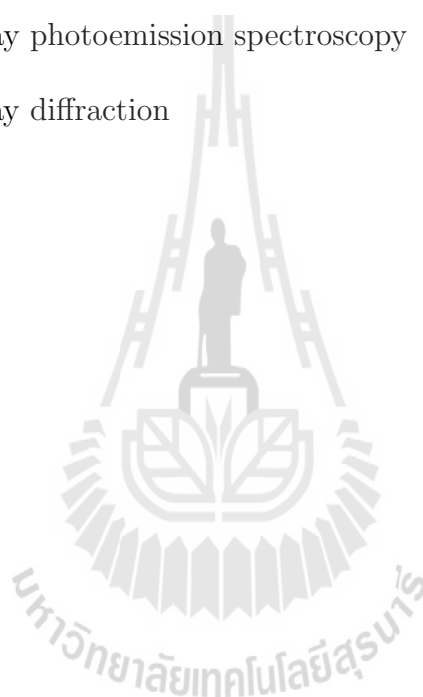
LIST OF SYMBOLS

E_{kin} Kinetic energy

E_B Binding energy

ϕ Work function

θ Emission angle or Bragg angle

Λ Wavelegth of incident photon

$I(k, \omega)$ Photoemission intensity or photo current

$k_\perp$ Perpendicular or out-of-plane momentum

$k_{//}$ Paralel or in-plane momentum

k_x, k_y, k_z Momentum in x, y and, z direction

$\hbar$ Plank constant

$h\nu$ Photon energy

$A(k, \omega)$ Spectral function

m^* Electron effective mass

m_e Electron mass

E_F Fermi energy

E_i Initial energy

E_f Final energy

ψ_i Initial state wave function

ψ_f Final state wave function

V_0 Inner potential

w Transition probability

$\mathbf{p}$ Electron momentum (operator)

CHAPTER I

INTRODUCTION

1.1 Motivation

Since the discovery of graphene in 2005, there have been more and more research not only on carbon-based materials but also other two-dimensional (2D) materials and layered compounds. Rapid progress of several research works have promised new-generation 2D-materials-based nanoelectronics (Wang et al., 2012; Ponomarenko et al., 2008). In the present, graphene gains much research attention due to its excellent properties and promises many applications such as semitransparent electronics, solar cells, and energy storage (Eda et al., 2008; Wang et al., 2008; Yoo et al., 2008). However, even though graphene has many unique properties, how to open the band gap of a graphene sheet, which is necessary for transistor application, is not trivial. Although several research works report the success of opening the gap in graphene in lab scale, the methods are mostly expensive with low successful rate (Zhou et al., 2007; Balog et al., 2010). From this aspect, transition metal dichalcogenides (TMDs) such as MoS_2, WSe_2, $HfSe_2$, which have the 2D semiconducting materials with the similar structure as graphene but exhibit some unique properties (Wang et al., 2012; Zhu et al., 2011) can be the great candidates for replacing silicon in new generation electronics and optoelectronics (Mak et al., 2010). Currently, there are many research works on semiconducting TMDs already in both the fundamental and applied directions. For example, the thickness modulated of MoS_2 optical energy gap has been used as a very sensitive nanosheet phototransistor (Lee et al., 2012). Interestingly, Zeng et al. and Cao et al. dis-

cover a possibility to control the valley and spin degree of freedom by using optical pumping in MoS_2. This suggests rich opportunities in making a valleytronic device (controlling the number of electrons at the energy-degenerated at different corners of the Brillouin zone) rather than controlling charge (electronics) or spin (spintronics) of electrons (Zeng et al., 2012; Cao et al., 2012).

1.2   Approach of the two-dimensional materials study

Nowadays, the studies of 2D materials go far beyond the graphene studies. There are many intensive studies including atomic crystal (in h-BN, representing the outstanding dielectric property and a good substrate), several transition metal oxides (TMOs, representing functional properties), and TMDs (exhibiting excellent semiconductor and suitable for scaled electronics). In this work, we focus only TMDs whose bulk form have been used in catalyst and optoelectronics for more than 40 years (Frindt and Yoffe, 1963; Wilson and Yoffe, 1969). MoS_2 is a layered semiconductor with high mobility which could be good for functional nanoelectronic devices. Bulk MoS_2 exhibits an indirect band gap of 1.8 eV (Ellis et al., 2011) with potential use in place of silicon. Few-layer MoS_2 samples have been studied as field effect transistors (FETs) and sensors (Radisavljevic et al., 2011; Li et al., 2012).

For a long time, researchers thought that a monolayer of MoS_2 does not exist (Landau, 1937) in the free-standing form due to the prediction of an unstable state at finite temperature. Until in 2005, Novoselove et al. (Novoselov et al., 2005b) published the isolated graphene and 2D atomic crystals led to unusual electronic properties. This is the origin of widely-spread research for 2D materials. MoS_2 and some TMDs exhibit a striking cross over from indirect to direct band gap semiconductors as they are thinned down to a single monolayer (figure 1.1).
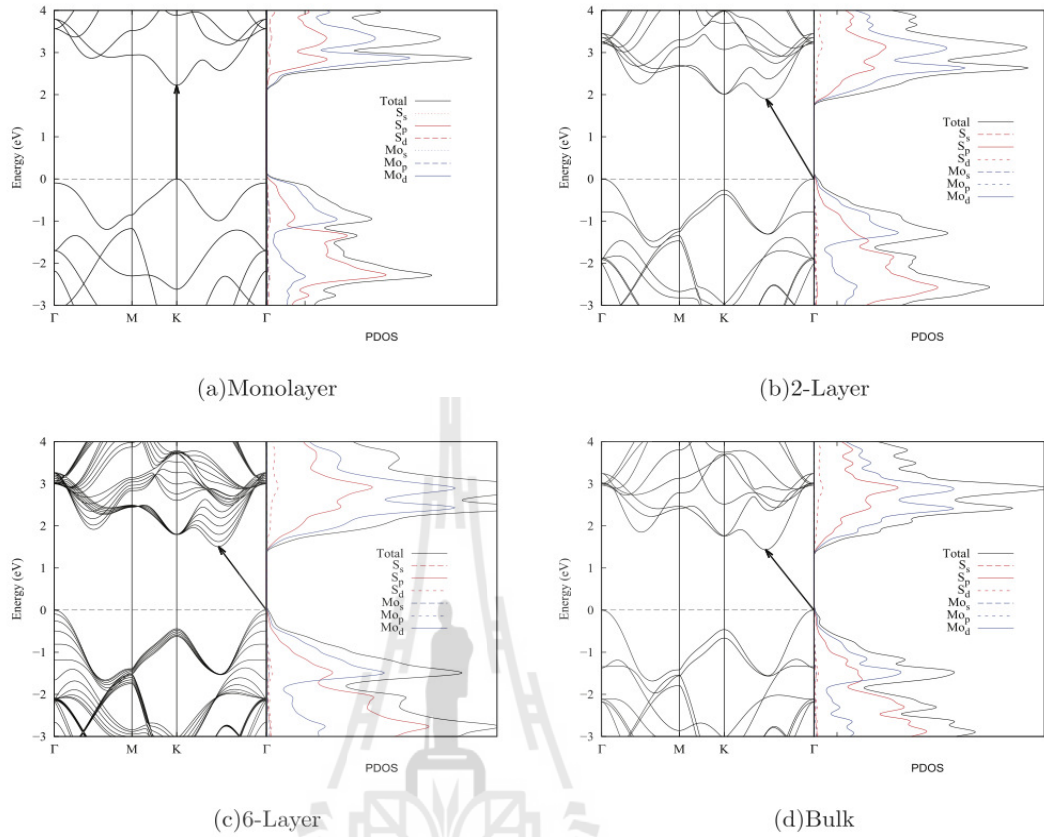
Figure 1.1 a)-d) DFT-calculated band structure of layered MoS_2 in various number of layers. There is a strong shift in the VBM from $\bar{\Gamma}$ to $\bar{K}$ resulting to the crossover from the direct to indirect band gap when the layer is thicker than monolayer (Ellis et al., 2011)

.

This transition has been predicted correctly by the calculation (Cappelluti et al., 2013; Ellis et al., 2011) which is resulted from the quantum confinement and inversion asymmetry (Mak et al., 2010; Splendiani et al., 2010). Layered TMDs consist of the sandwiches of metal layer and two chalcogen layers with weak van der Waals forces (vdW) (Wilson and Yoffe, 1969). These layered materials can be mechanically exfoliated to a monolayer as obtained in graphene or MoS_2 (Coleman

et al., 2011; Novoselov et al., 2005b). The direct band gap in MoS_2 monolayer can be measured by using photoluminescence reported by K.F. Mak et al. (Mak et al., 2010). Recently, Y. Zhang et al. can observe the direct transition from indirect to direct band gap in atomically thin epitaxial $MoSe_2$ by ARPES (Zhang et al., 2014c).
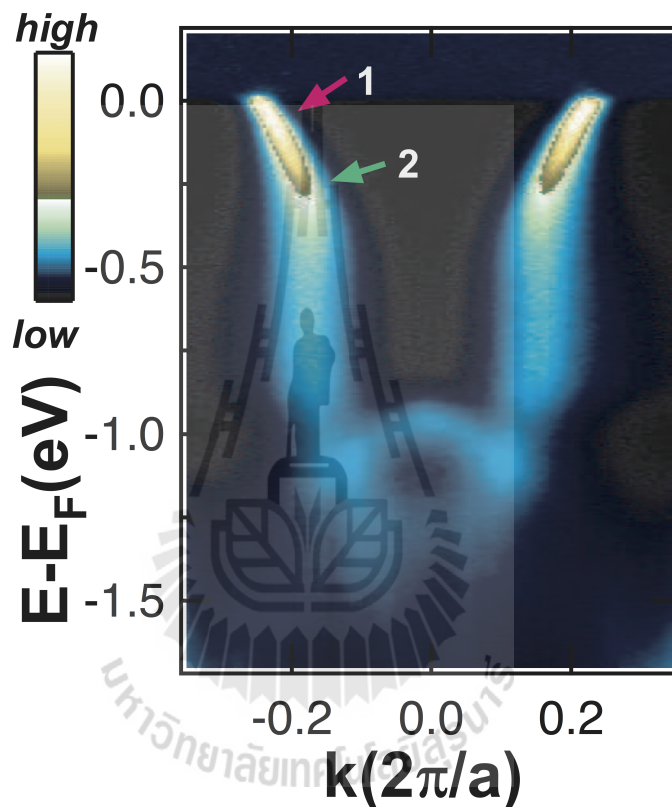
Figure 1.2 Energy scales in nodal band dispersion of a cuprate. Region 1 is low-energy anomaly (kink) at approximately 30 - 90 meV. Region 2 is high-energy anomaly at approximately 300 - 500 meV (Meevasana et al., 2007).

The objective of this study can be divided to be two main parts. First. I would like to understand the electronic properties of some TMDs by using angled-resolved photoemission spectroscopy (ARPES). The main TMD used in this study is MoS_2 while other TMD compounds such as $HfSe_2$, $PdTe_2$ and WSe_2 are par-

tially studied. We aim to study the electronic structure modified by using alkali metal (such as Na, K). My goal is to understand its behaviour from the electronic structure measured by ARPES while the density functional theory (DFT) calculation is also performed to cross-check our assumptions. In particular, I try to understand the mechanism of potassium evaporated on MoS_2 by exploiting the DFT calculation of layered dependence, potassium favorable, and vdW expansion. For the second goal, I would like to adapt our fundamental property measured by ARPES to other macroscopic measurement by using terms of spin-orbit coupling, two dimensional electron gases (2DEGs), and the band gap modification.
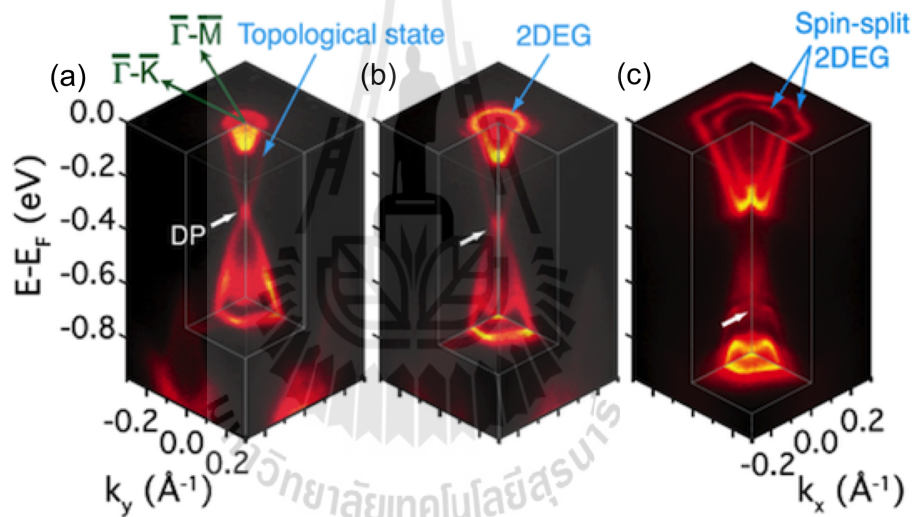
Figure 1.3 a)-c) Electronic structure of Bi_2Se_3 measured using time-of-flight ARPES at increasing times after cleaving the sample ($h\nu = 19.2$ eV, T = 10 K). (King et al., 2011)

.

ARPES is a unique technique that can directly probe the electronic structure of materials. This is a powerful tool that can be used to study wide range of interesting properties especially in condense matter physics. This led us to understand an important role of emergence novel properties such as high temperature

superconductivity, colossal magnetoresistance and other unconventional phenomena in complex quantum system. For example, Meevasana et al. (Meevasana et al., 2007) have been studying high-T_c superconductivity in cuprates. They can probe the low-energy kink of 0.03 - 0.09 eV (Region 1) which is regarded to the interaction of electron to sharp bosonic mode (Damascelli et al., 2003) as well as the high-energy anomaly of 0.3 - 0.5eV (shown in figure 1.2). King et al. (King et al., 2011) can measure the band variation in topological insulator Bi_2Se_3. figure 1.3 shows the evolution of Bi_2Se_3 band structure from linearly-dispersing, then the appearance of 2DEG state, and then a well-defined spin splitting state after increasing times. They suggest that such band evolution comes from the quantum confinement at the surface (Bianchi et al., 2010). Moreover, Meevasana et al. (Meevasana et al., 2011) applied an irradiation dose of UV light to create and probe the 2DEGs at the surfaces of bare $SrTiO_3$. This shows the scientific impact of ARPES measurements in studying novel phenomena of quantum materials.

We can also study the effect of alkali metal or transition metal dosing at the material surfaces to the electronic structure of the materials of our interest. The technique is to use the *in situ* evaporation source. There are three possible outcomes: adsorption, intercalation, or sandwich-breaking chemical reaction, depending on evaporated-elements and substrates (figure 1.4). Because of the weak vdW forces in layered TMDs, TMDs have been widely studied in the terms of intercalation process. As mentioned, monolayer TMDs have been successfully fabricated by many methods such as exfoliation and molecular beam epitaxy (MBE) (Novoselov et al., 2005b; Zhang et al., 2014c). This yield novel and ultimate properties from those not found in bulk TMDs (Zeng et al., 2012). By carrier doping, superconductivity in MoS_2 can be observed in the temperature-carrier density diagram (Ye et al., 2012). Quasi-freestanding epitaxial graphene

on SiC obtained by hydrogen intercalation was observed by ARPES (Riedl et al., 2009). Our discovery of quasi-freestanding MoS_2 layer was also achieved by alkali metal evaporation where the electronic structure of that was measured by ARPES. This intercalation provides another possible way to effectively create the large area monolayer of TMDs on bulk samples.
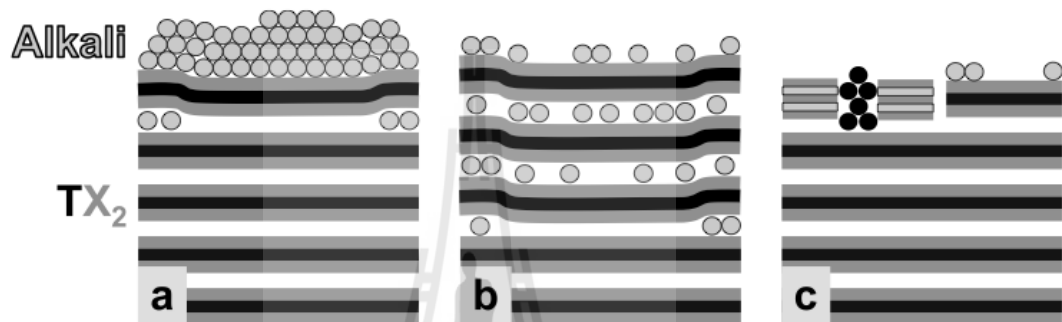
Figure 1.4 Schematic illustration of three distinct outcomes of *in situ* alkali deposition on TMD surfaces (TX_2): (a) layer-by-layer growth of the alkali metal, (b) intercalation of the alkali atoms in between the interlayer gaps and (c) sandwich-breaking chemical reaction (Rossnagel, 2010).

1.3 Thesis outline

This thesis is organized as following. In chapter II, the technical background of photoemission spectroscopy including photoelectric effect, ARPES, photoemission process, and Fermi golden rule will be reviewed. The preparation before using ARPES, system requirements, and the techniques performed during ARPES have also been demonstrated in this chapter. In chapter III, the theory of semiconductors, alkali metal intercalation, spin-orbit interaction, and band bending will

be described. The viewpoint of two-dimensional electronic structures will be discussed in chapter IV. I will also talk about our study of 2DEG at the surface of $KTaO_3$ which relates to this system in this chapter. Then, I would like to describe about graphene and its electronic structure which is the original study of other TMDs. Moreover, the introduction of 2D TMDs especially in MoS_2 among physical and electronic properties as well as some techniques to investigate the sample and the preparation before measurement will be discussed in this chapter. Besides MoS_2, the interesting properties in other TMDs ($HfSe_2$, $PdTe_2$, and WSe_2) regarding band splitting, new 2D topological state, and orbital character dependence will be mentioned.

Chapter V represents my main work on MoS_2. In this chapter, the effect of potassium evaporation on the MoS_2 electronic structure will be presented. The experimental observation of band splitting in the valence band, 2DEG-like state at the conduction band and the implication of potassium intercalation will be discussed in this chapter. The conclusion and my future direction will be given in chapter VI. In appendix A, I will show the example for extracting the important quantities from ARPES data. This part will also discuss about the DFT calculation performed in this study.

Besides the main work on MoS_2 samples, in appendix B, I will explain about how to apply the information obtained by ARPES to other macroscopic measurements. In this part, I will show the dielectric enhancement in $CaCu_3Ti_4O_{12}$ (CCTO) and possible light sensor made from $SrTiO_3$ (STO). In these studies, the effect of oxygen vacancies induced by irradiation is purposed to be the origin of such changes. In Appendix C, the window applications (C++ program) used for monitoring and commanding the temperature controller of an ARPES system will be described. I will provide the further programming which will be able to perform

the full measurement at low temperature.

Finally, I would like to emphasize that my main work is the photoemission study of MoS_2. In this work, I have done a major contribution on the measurement, data analysis, and manuscript writing. The calculation part has been done by my coauthor. There are three more works introduced in this thesis which I was a coauthor. Firstly, I have contributed on the ARPES measurement on the photoemission study of $KTaO_3$ (presented in chapter 4.1.2). Secondly, regarding on the CCTO work, I contributed in the experimental parts including capacitance, photoemission and resistance measurement. Lastly, I cooperated on the sample preparation and resistance measurement in STO work.
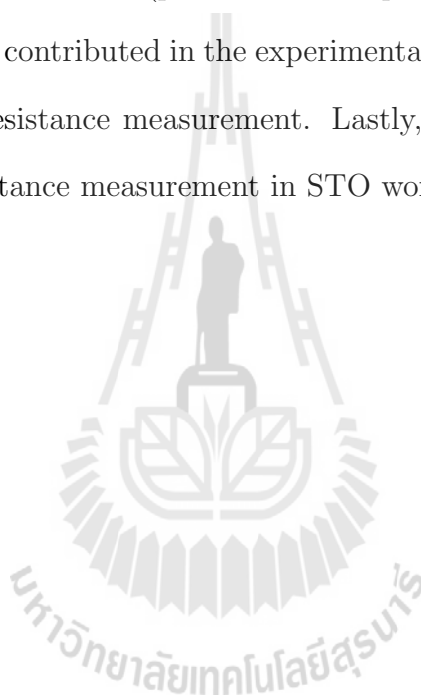
CHAPTER II

PHOTOEMISSION SPECTROSCOPY

Photoemission spectroscopy and angle-resolved photoemission spectroscopy (AR(PES)) have unique advantage of directly probing band structure of materials which widely used to study the single crystal solid materials. In this chapter, firstly, the introduction of ARPES with the original view of photoelectric effect and some simple equations will be provided. Then, the simple physical pictures of photoemission process called three- and one-step model are presented. The intensive explanation of photoemission theory is described in section 2.4. The additional sections about the ARPES system including sample preparation, ARPES apparatus, and related techniques are discussed in section 2.5-2.7.

2.1   Photoelectric effect

Photoemission spectroscopy (PES) is the technique used to probe the electronic structure of the materials based on the photoelectric effect. The photoelectric effect was discovered by Hertz in 1887 (Hertz, 1887) and explained as the quantum nature of light by Einstein in 1905. By exposing the light with photon energy ($h\nu$) the electrons are kicked out from the surface of the material with the minimum kinetic energy (E_{kin}) when the photon energy larger than work function (Φ). The E_{kin} of electron ejected out of materials depends on its binding energy (E_B) and Φ, where their relation can be written as

$$E_B = h\nu - \Phi_A - E_{kin} \qquad (2.1)$$

In general, the work function of the analyzer (Φ_A) is larger than the work function of measured sample. Therefore, Φ_A is usually respected as the reference work function relating to the Fermi level in all experiments (using the same analyzer).

2.2 Angle-resolved photoemission spectroscopy

Here, we determine the electronic structure which can be represented as the relation of energy (E) and momentum (k) in the materials. Regarding to the photoelectric effect, electrons with different E_{kin}, ejected out of the sample surfaces which were excited from the incident photon, will be analyzed as a function of the emission angle (θ) of the analyzer. As the in-plane momentum ($k_{//}$) is conserved in crystal surface, $k_{//}$ is related to the θ with this simple equation

$$k_{//} = \sqrt{\frac{2m_e E_{kin}}{\hbar^2}} sin\theta \qquad (2.2)$$

In the past, we must rotate the analyzer every time to obtain the information against different momentum. Fortunately, the modern setup of PES called angle-resolved photoemission spectroscopy (ARPES) has been established with the line electron collector. This produces a lot of benefits to shorten the experiment time in the order of $\frac{1}{1000}$ and makes the experiment much easier. Nowadays, the results from ARPES measurement are expressed in photocurrent term ($I(E, k_x, k_y)$). We can gain information of in-plane dispersion of the occupied bands by tracing the peaks in the photocurrent. A plot of photocurrent for a fixed momentum is called "energy distribution curve (EDC)" while a plot of photocurrent with a fixed energy is called "momentum distribution curve (MDC)". The out-of-plane or perpendicular momentum denoted as $k_\perp$, cannot be directly measured from ARPES because the $k_\perp$ is large relative to the vacuum level. The $k_\perp$ is not conserved due to the lack of translation symmetry along out-of-plane direction. This is well known as

"$k_\perp$ problem" in photoemission. However, the $k_\perp$ can be obtained by applying the nearly-free electron description for final bulk Bloch states which is expressed as

$$E_f = \frac{\hbar^2(k_{//}^2 + k_\perp^2)}{2m_e} - V_0 \tag{2.3}$$

where V_0 is called the inner potential of the material which is typically in the order of 10 eV for most materials. To get the $k_\perp$ value, the final energy ($E_f = E_{kin} + \Phi_A$) and $k_{//}$ have to be inserted into eq. 2.3. Finally, we get

$$k_\perp = \frac{1}{\hbar}\sqrt{2m(E_f cos^2(\theta) + V_0)} \tag{2.4}$$

Nevertheless, this $k_\perp$ problem is not an issue for 2D system because there is no dispersion along the z-direction.

2.3 The photoemission process

The photoemission process can simply be described as following; after shining the light on the sample surface, electrons are ejected out to the vacuum described by the photoelectric effect. From now on, we can exploit the energy and momentum conservation from eq. 2.1 and 2.2 to determine the behaviour of these electrons. However, the correction of the photoemission with this simple relation is certainly insufficient. So, in this part, the appropriate and necessary description including three-step model and the more realistic of one-step model will be discussed.

2.3.1 Three-step model

The three-step model is commonly used to describe the simple view of the photoemission process. The three important steps and description of this model are displayed in figure 2.1 (left). The three steps of photoexcitation, transport, and escape of photoelectron are shown below.

I) Photoexcitation of electron inside the sample

This step occurs when an occupied electronic state (initial state) is excited by the photon to an unoccupied state. Then, the photon is adsorbed and an electron-hole pair is created inside the crystal with the transition probability (w) given by the Fermi golden rule. This rule will be explained in the next section. As photons have very little momentum, the electron momentum is also unchanged in this state.

II) Transport of photoelectron to the surface

This process can be described in terms of an effective-mass-mean-free-path of any materials. This term relates to the probability of the excited electron travel through the surface without scattering. In this process, some inelastic scattering electrons give some needless background continuous spectra which is usually subtracted.

III) Escape of the photoelectron into the vacuum:

The excited electron in the surface requires the energy which is higher than work function of the materials to escape from the surface. In this process, the momentum perpendicular to the surface is not conserved depending on excited energy and the sample surface. Consequently, this step provides the information of the transmission probability out of the surface depending on the excited energy and work function.

2.3.2 One-step model

One-step model considers the whole photoemission process as one single step. The whole process can be described as; the excited electron from an initial Bloch state go to a damped final state near the surface. This damping state of electron takes care the whole process traveling through the surface of solid with

a short mean free path. In contrast to the three-step model, the one-step model replaces three artificial step of three-step model as a single coherent process shown in figure 2.1 (right).

Correction of the photoemission process is based on Fermi's Golden rule with proper function for initial and final state. This problem can not be solved rigorously. However, the key to attempt the solution is the simplification within the sudden approximation which is extensively used in many body calculation of the photoemission spectra. This approximation works by assuming no post-collisional interaction between photoelectron and system left behind and no relaxation from the excitation. This approximation serves well for relatively-high kinetic energy photoelectrons.
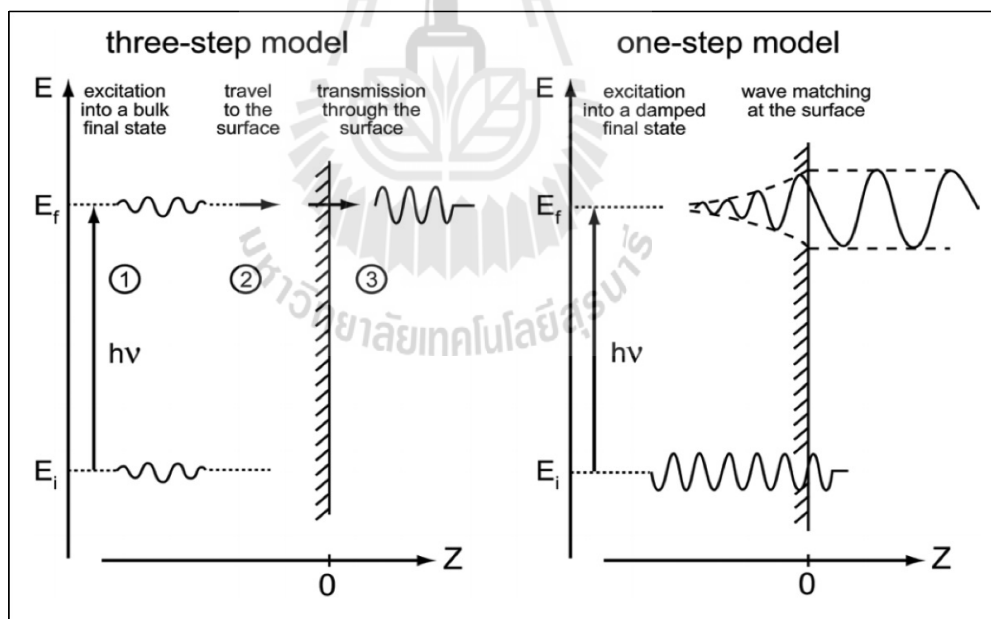
Figure 2.1 Illustration of three-step and one-step model crucially use for describing the possible photoemission process (Hüfner, 1995).

2.4 Photoemission theory

This section will provide more intensive interpretation of photoemission rather than the previous discussion of simple physical picture of photoemission process. Start with the very famous quantum physics rule called "Fermi's golden rule", which is the probability approximation about the transition from the N-electron ground state into one of the possible final states by photoexcitation using the perturbation theory. The Fermi's golden rule has the general formula as

$$w_{f,i} = \frac{2\pi}{\hbar} | < \psi_f^N | H_{int} | \psi_i^N > |^2 (E_f^N - E_i^N - h\nu) \tag{2.5}$$

where Ψ_i^N and Ψ_f^N are the initial- and final- state energies of the N-particle system. The photon field gives rise to photoemission process via a perturbing term in the Hamiltonian given by

$$H_{int} = -\frac{e}{2mc}(2\mathbf{A} \cdot \mathbf{p} - i\hbar\nabla \cdot \mathbf{A}) \tag{2.6}$$

where $\mathbf{p}$ and $\mathbf{A}$ are the electronic momentum operator and the electromagnetic vector potential, respectively. In the bulk or continuous region, where $\mathbf{A}$ is constant over atomic dimension and therefore $\nabla \cdot \mathbf{A} = 0$. Then, the direct transition term $(\mathbf{A} \cdot \mathbf{p})$ exhibits dominant contribution to the photoemission intensity preserving the crystal momentum of the electron during the photoexcitation while the second term $(\nabla \cdot \mathbf{A})$ is ignored. However, at the surface, we should concern about $\nabla \cdot \mathbf{A}$ term which is important where the electromagnetic field may have a strong spatial dependence and can be compared to the direct transition term. Next, the initial state wave function is assumed to be the product of one-electron orbital (ϕ_i^k) and an (N-1)-particle term from the single determinant. This relation can be expressed as

$$\Psi_i^N = A\phi_i^k \Psi_i^{(N-1)} \tag{2.7}$$

where A is the properly N-electron wave function antisymmetric operator, ϕ_i^k is the wave function of the initial state with momentum k before photoexcitation, and $\Psi_i^{(N-1)}$ is the wave function of the remaining (N-1) electrons.

By the sudden approximation, the final state can also be written as

$$\Psi_f^N = A\phi_f^k \Psi_f^{(N-1)} \tag{2.8}$$

Here, ϕ_f^k is the wave function after photoexciteation, and $\Psi_f^{(N-1)}$ is the final state wave function of the (N-1) electrons left behind. Two equations above are substituted into Eq. 2.5 and the solution can be then written as

$$< \Psi_f^N|H_{int}|\Psi_i^N > = M_{f,i}^k < \Psi_s^{N-1}|\Psi_i^{N-1} > \tag{2.9}$$

By looking into this immediate formula. The $< \phi_f^k|H_{int}|\phi_i^k > \equiv M_{f,i}^k$ term is the one-electron matrix element (resulted from eq. 2.7 and 2.8). The second term is the (N-1)-electron overlap integral, and the $\Psi_f^{(N-1)}$ is replaced by the eigenstate ($\Psi_s^{(N-1)}$). To define the real system, considering the ejected electron from ϕ_i^k to ϕ_s^k scatters with the remaining (N-1) electrons system. The system organizes to reach its minimum energy allowing many possible transitions from wave functions (Ψ_s^{N-1}) and energies (E_s^{N-1}) to the final state of (N-1)-electrons system. Then, the total photoemission intensity measured as a function of E_{kin} at any k, namely $I(k, E_{kin}) = \sum_{f,i} W_{f,i}$, is equal to

$$I(k, E_{kin}) = \sum_{f,i} |M_{f,i}^2| \sum_s |c_s^2|\delta(E_{kin} + E_s^(N-1) - E_N^i - h\nu) \tag{2.10}$$

where $|c_s^2| = | < \Psi_s^{N-1}|\Psi_i^{N-1} > |^2$ is the probability that electron from initial state i can be removed from (N-1) electrons systems into excited state s. In non-interacting system with $\Psi_i^{N-1} = \Psi_{s_0}^{N-1}$ and for one particular $s = s_0$, where $|c_{s_0,i}|^2$ and all others are vanished, the ARPES spectra is formed as a delta function at the Hartree-Fock orbital energy. In contrast, for strongly-correlated systems, many of

the $|c_{s,i}|^2$ are non-zero because any Ψ_i^{N-1} overlaps with many of the eigenstates Ψ_s^{N-1}. Hence, the ARPES spectra is not only the single but also many delta functions according to the number of excited state created in the process. By invoking sudden approximation, we can now obtain the ARPES intensity for a 2D single-band system which can be written as

$$I(k,\omega) = I_0(k,\nu,\mathbf{A})f(\omega)A(k,\omega) \tag{2.11}$$

where $k=k_{//}$ is the in-plane electron momentum, ω is the electron energy respect to the Fermi level, ν is the electron energy, and A is the polarization of incoming photon. Term of $I_0(k,\nu,\mathbf{A})$ is proportional to the squared one-electron matrix element $|M_{f,i}^k|^2$. The Fermi Dirac function $(f(\omega) = (e^{\omega/k_B T} + 1)^{-1})$ can probe only occupied states. The $A(k,\omega)$ term will be introduced later as spectral function. In some cases, for example, in many 2D systems, the $I_0(k,v,\mathbf{A})$ is slowly varying respect to the energy and momentum. Hence, photoemission can directly probe the spectral function which is directly related to the Green's function introduced by

$$A(k,\omega) = \frac{ImG(k,\omega)}{\pi} \tag{2.12}$$

In strongly-correlated-electron system, the correction of the Green's function $(G(k,\omega))$ may be described in terms of electron self energy $\Sigma(k,\omega) = \Sigma'(k,\omega) + i\Sigma''(k,\omega)$. The real and imaginary parts of the self energy carry the information of the energy renormalization and lifetime of an electron with non-interacting band (ϵ_k) and k. Thus, the Green's function can be expressed in term of self energy as

$$G(k,\omega) = \frac{1}{\omega - \epsilon_k - \Sigma(k,\omega)} \tag{2.13}$$

Substituting eq. 2.13 to eq. 2.12 , the corresponding spectral function is

$$A(k,\omega) = -\frac{1}{\pi}\frac{Im\Sigma(k,\omega)}{[\omega - \epsilon_k - Re\Sigma(k,\omega)]^2 + [Im\Sigma(k,\omega)]^2} \tag{2.14}$$

Note that ϵ_k is the bare band of the electron, we can see that when $\Sigma(k,\omega) = 0$, the spectral function is a delta function, or assuming no electron-electron correlation, the function will distribute as a Lorentzian function.

In general, many systems always have electron-electron correlation but remain at equilibrium itself. Disturbing the system by adding one extra electron into Bloch state causes the excitation into the whole system. This process will then result in the creation of additional electron-hole pairs. Hence, all of energy and electron lifetimes are changed because of the Fermi sea (discontinuous of momentum distribution). To simplify this matter, we introduce "quasiparticle" to describe that the correlated electrons are dressed by virtual excitations and move coherently with the electron through the crystal. Thus, the spectral function in the correlated electron system will be determined by Lorentzian function based on energy and lifetime of introduced quasiparticle.

2.5 Sample characterization

2.5.1 Single crystal x-ray diffraction: Laue method

The x-ray diffractometer or x-ray diffraction (XRD) is a common technique to determine the crystal structure in solid materials. The well-known equation for XRD is Bragg's law which has been established since 1912. This equation describes the relation between diffraction angle and the point position in the reciprocal space which can be expressed as

$$2dsin\theta_x = n\lambda \tag{2.15}$$

where n is the integer according to the number of scattering plane which is usually denoted as 1, d is the plane spacing in the atomic lattice, λ is wavelength of incident x-ray wave and Bragg angle (θ_x) is the angle between incident and the reflection plane.

On the other hand, the oldest x-ray diffraction method is Laue method (LM) which serves as a powerful tool to study the layered materials, single crystals, and polycrystallines. This technique is very helpful in my work as it is used to check the perfection of our single crystal before the ARPES measurement. LM uses the graphical method to determine the Laue spots on the photograph. LM have been divided into transmission and back-reflection modes. The perfection of the crystal can be determined by the spots on the photograph. The spots from perfect crystal are sharp while the spots are diffused or elongated for the imperfect or polycrystalline. The practical formula of LM introduced by E. Schiebold (Schiebold, 1932) expresses how to calculate the important value for the standard setup as shown in figure 2.2.

The position of any spots away from the center of the incident light can be determined using the geometry in figure 2.2. In the simplest case, if the incident x-ray beam is perpendicular to the principal crystal plane and the photographic plane (c-axis or (001) plane). A distance of Laue spot on the film (r) can be expressed according to the θ_x as

$$r = D \cdot \tan 2\theta_x \qquad (2.16)$$

where D is the distance between the crystal and the photographic plate. The azimuthal angle (ψ) and θ_x are independent of the wavelength and can be expressed in terms of unit cell dimension. The ψ represents the possible spot away from the reference orientation related to the angle between a- and b-axis while the reflection

Figure 2.2 Geometrical relationship between the position of the Laue spots and the reflecting plane (Kedesy, 1954)

angle (γ) represents the distance away from the center. The relation between ψ and γ can be given by

$$\tan \psi = \frac{1}{\sin \gamma} (\frac{b}{a} \cdot \frac{h}{k} - \cos\gamma) \qquad (2.17)$$

If the ratio between h and k is the same, this condition gives the discrete spots lining straight from the center of the pattern. In the hexagonal lattice crystal (i. e. MoS_2), the final formula of ψ and θ_x have been calculated and expressed as

$$\sin \theta_x = d_{hkl} \cdot \frac{l}{c} \qquad \tan \psi = \frac{1}{3}\sqrt{3}(2\frac{h}{k} + l) \qquad (2.18)$$

As mentioned above, D, ψ, and θ_x are very important values in Laue method. If we have the Laue pattern, the atomic structure of any materials can be easily determined. The Laue photographs of my samples will be discussed later.

2.5.2 Low energy electron diffraction

Low energy electron diffraction (LEED) is the ideal tool to investigate the atomic structure at a crystal surface. LEED can either be used to carry out the qualitative information of size, symmetry, and rotational alignment or take the quantitative values of various diffracted beams recorded as the function of the incident electron beam energy (I-V curves). The LEED experiment is operated at well-defined low energy (typically in 20-200 eV) and shined perpendicular to the sample surface. The fluorescent screen is placed in the opposite direction of the sample in order to take the picture of the scattered electron. The illustration of LEED components are shown in figure 2.3 (a) including specific sample holder, an electron gun, and hemispherical fluorescent screen. In particular cases, some additional components such as sputtering gun and Auger-Electron spectroscopy are used for cleaning or determining the purity of the surface. To get the the right scattered diffraction pattern, the sample have to be a single crystal. Because of the sensitive surface, LEED is usually performed in UHV to keep the sample clean. In our system, the effect of dosing is determined by this condition as well.

LEED consists of three main theoretical components which are surface sensitivity, kinematics, and interpretation. The surface sensitivity is commonly treated by the exponential decay of primary electron beam intensity through the penetration depth. For low-energy electrons, they lose the ability to penetrate through the sample causing by inelastic scattering. The mean free path of low-energy electron is around 5 - 10 $\mathring{A}$ in effective of a few atomic layers (Oura et al., 2003). The kinematic of LEED can be determined by de Broglie relation while the light acts as wave-particle duality expressed as

$$\lambda = \frac{h}{p} \tag{2.19}$$

Then, we can substitute the relation of $p = m \cdot v = \sqrt{2mE}$ to get the relation between wavelength and acceleration voltage (V) as

$$\lambda = \frac{h}{\sqrt{2mV}} \qquad (2.20)$$

The spots obtained from LEED will be determined in the reciprocal space when the Bragg's condition is satisfied. LEED pattern is controlled by the incident electron energy and the real space lattice. The example of LEED pattern of simple cubic structure is illustrated in figure 2.3 (b).
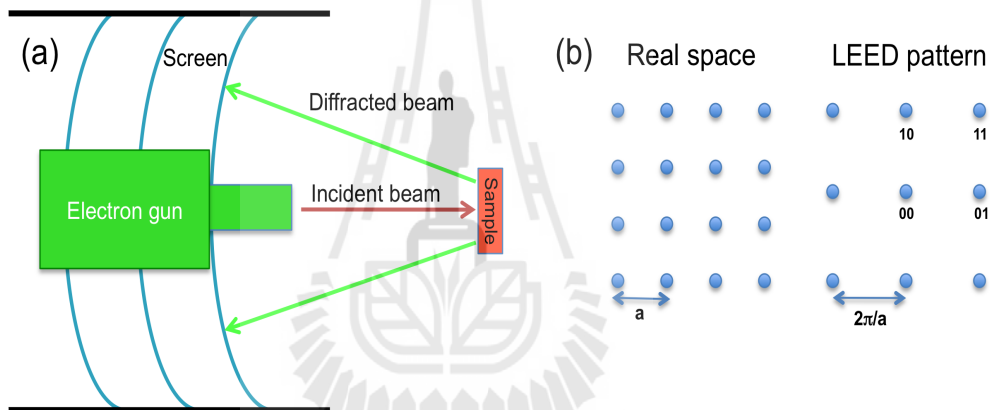
Figure 2.3 a) Schematic of LEED equipment. (b) Equivalent between real space lattice and obtainable LEED pattern.

2.6   ARPES system

In the past, ARPES studies were restricted by the intensity of light source and electron analyzer which are the major components in ARPES system. Nowadays, the development of both components together with the sample manipulating and cooling system gives the energy resolution in the order of 10 meV which can be used to detect much of interesting physics phenomenon. Synchrotron light source

which contains wide spectral range of high intensity and continuous spectrum is commonly used for ARPES measurement. Other sources such as gas discharge lamps (monochromatic light with low intensity but high angular solution) and newly-developed lasers are also available.

The synchrotron light radiation is generated by bending magnet holding electrons inside storage ring. The light is originated by controlling the classical electrondynamics states causing the charged particles by acceleration which emit electromagnetic radiation. In order to enhance the output of photon flux, many insertion devices such as wigglers or undulators are installed along the storage ring until reaching the desired spot size. In ARPES, the multi-wavelength light passes through the grating for wavelength selection making the monochromatic photon. The photon energy in ultraviolet (UV) regime is commonly used for surface sensitive ARPES due to the typical atomic-layer-mean-free-path. Photon energy of 40 - 80 eV is used in our experiment. For synchrotron light (beamline resolution), the resolution is controlled by the exit slit before the sample. Note that most of ARPES experiments in this thesis were carried out at beamline 10.0.1 (high energy resolution) of the Advanced Light Source (ALS), USA.

The electron analyzer is one of major components for ARPES consisting of an electrostatic lens, hemispherical deflector, entrance slit, exit slit, and electron detector. Firstly, the traditional hemispherical analyzer is discussed in order to understand the simple view of electron collection. The excited electrons from the sample are focused and retarded by electrostatic lens to the entrance slit. This allows some electrons with right kinetic energies within a narrow range center at

$$E_{pass} = \frac{e\Delta V}{\frac{R_2}{R_1} - \frac{R_1}{R_2}} \tag{2.21}$$

These electrons which satisfy this equation can reach the exit slit and then the

detector without colliding with the analyzer wall. Where ΔV is a potential difference, R_1 and R_2 are radius of two hemispheres. The energy resolution of measured electron can be calculated by

$$\Delta E_a = E_{pass}(\frac{d_w}{R_0} + \frac{\alpha^2}{4}) \tag{2.22}$$

where d_w is the width of the entrance slit, $R_0 = \frac{R_1+R_2}{2}$, and α acceptance angle. The photoemission intensity can be recorded as a function of kinetic energy by scanning the electrostatic lens.

In the present, our ARPES system employs new innovation of electron analyzer with 2D detector. The energy distribution curves (EDCs) are obtained simultaneously at wide angular range with the great advantages of shorten measurement time and better quality. The 2D state-of-the-art analyzer consists of two micro-channel plates and a phosphor plates in series, followed by a CCD camera. The electrons travel through the analyzer are determined simultaneously as a function of E_{kin} and θ. The 2D matrix data typically contain three axis of E_{kin}, θ, and the photoelectric intensity. In my work, our detector typically allows an energy resolution of a few meV. The accepted emission angle is $\pm 15°$ with resolution $0.3°$. By Applying parallel momentum equation (eq. 2.2), the angular scale is well defined for measuring across the first Brillouin zone of TMDs (i.e. $2pi/a \approx 1.327 \mathring{A}^{-1}$ for MoS$_2$). This 2D detector is very convenient as it can visualize the electronic structure as well as some more technical data in our work.

2.7 Related techniques

2.7.1 Photon energy dependence

Electronic structure probed at various photon energy is related to the different probing of the $k_\perp$ as described in the energy conservation in eq. 2.5. Photon
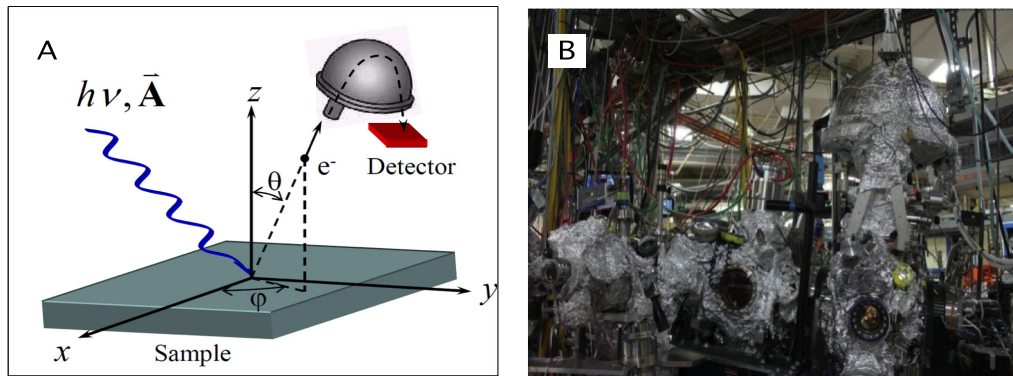
Figure 2.4 a) Schematic illustration of ARPES system, consisting of incident photon light, sample and analyzer. b) Real apparatus of high energy resolution ARPES at ALS, USA.

energy dependence is the method using to prove the 2D property in the material. The k_z momentum is not conserved in 3D material and can be varied by changing the energy of incident photon during the measurement. In our experimental part (chapter V), we performed the constant Fermi wavevectors during photon energy of about 40-65 eV in MoS_2 (shown later in figure 5.4). These energies cover more than one brillouin zone indicating the 2D nature in our sample. This evidence can be used to prove our assumption of quasi-freestanding monolayer on bulk MoS_2 in our measurement using potassium evaporation which will be discussed later in chapter V.

2.7.2 Core level spectroscopy

Core level spectroscopy is a proper tool which is used to investigate the chemical composition and assign a chemical state in any elements on the material surfaces. Soft x-ray photoemission spectroscopy (XPS) is used as a base technique to investigate the elemental compositions on the sample surfaces by irradiating
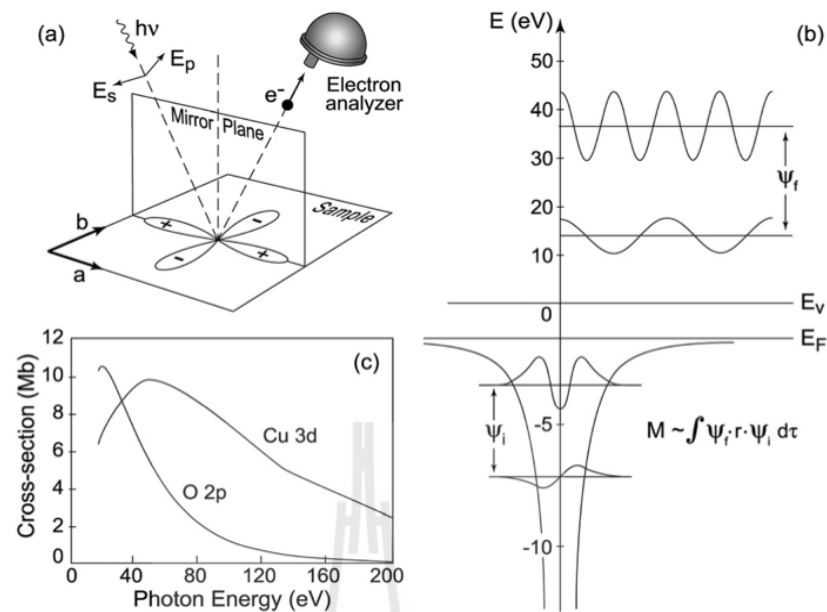
Figure 2.5 a) Mirror plane emission from a d_x^2-d_y^2 orbital indicates the opposite sign of initial wave function from each direction. b) Sketch of the optical transition between atomic orbital with different angular momentum results to the intensity variation of outcoming electron. c) Calculated photoionization-cross-section of Cu 3d and O 2p as a function of photon energy (Damascelli, 2004).

soft x-rays to the sample. The photoelectrons are ejected out of the surfaces and will be analyzed respect to their kinetic energies. Because each element has a characteristic set of binding energies, the peak positions can be used to identify the elements with respect to the surface of detected material. The concentration of particular element can be determined by integrating area under significant peaks based on the Shirley background (inelastic scattering event) which already has the standard ratio used to compare in any individual element. There will be some small shifts of the binding energies of a particular peak containing information of the chemical state of atoms. Apart from photoelectrons, the photoemission
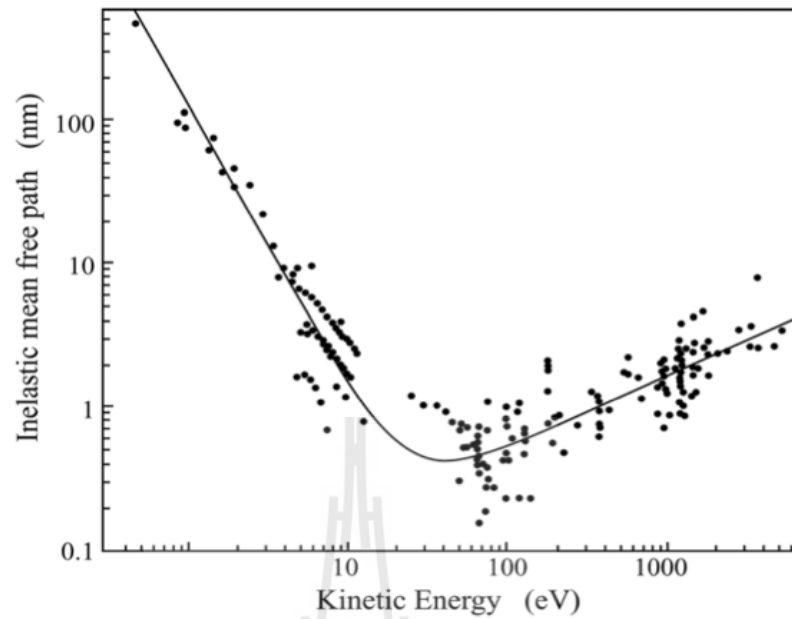
Figure 2.6 The standard 'Universal' electron-mean-free-path in solids as a function of kinetic energy (Seah and Dench, 1979).

process may excite the Auger electrons caused by empty state filled by electron from higher shell, particularly in the core level. However, the Auger electrons manifest the same kinetic energy so they can be clarified by changing the photon energy during experiment.

2.7.3 Matrix elements and finite resolution effects in ARPES

From above discussion, we can see that ARPES can directly probe the quantitative intensity of each spectra by the term of spectral function $(A(k, \omega))$. The intensity of each spectra is strongly dependent on the matrix element $(I_0(k, v, \mathbf{A}))$. However, some factors are taking into account to the ARPES intensity in the real experiment. The main factors are the finite resolution and intrinsic background
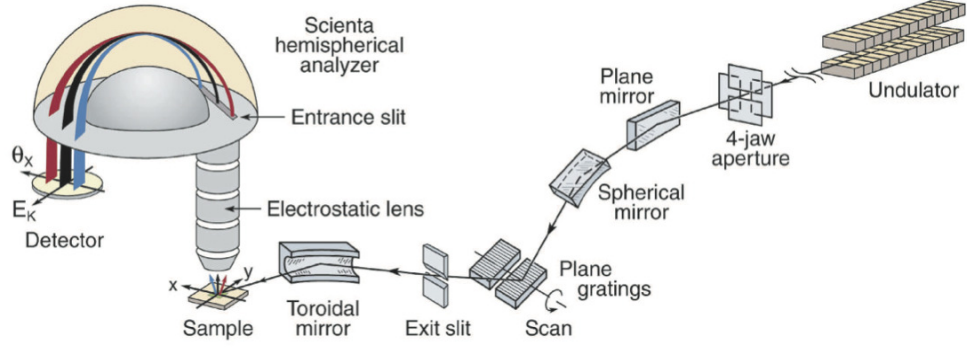
Figure 2.7 The diagram of beamline equipment consisted of a plane grating monochromator, optical slits, and electron analyzer (Damascelli, 2004).

from the secondary electrons (electrons escaping from the surface by inelastic scattering). The new expression of ARPES photocurrent ($I(k, \omega)$) can be rewritten as

$$I(k, \omega) = \int d\omega' dk' I_0(k', v, \mathbf{A}) f(\omega') A(k', \omega') R(\omega - \omega') Q(k - k') + B \qquad (2.23)$$

The presence of additional terms of energy convolution (R), momentum convolution (Q), and background function (B) indicates the effect of finite experimental resolution and the intrinsic continuous background of the secondary electrons in real experiment. The energy convolution is typically expressed in Gaussian function. The momentum convolution is more complicated, and the background is derived from the step-edge background (E_F step) or Shirley background (measured photocurrent). The effect of Matrix element can suppress or yield the intensity depending on the photon energy or experiment geometry. The variation of photoemission intensity with photon energy can be described in term of $|M_{f,i}^k|^2 \propto |(\epsilon \cdot k) < \phi_i^k|e^{ikr} > |^2$ which is strongly dependent on the initial state wave function. As shown in figure 2.5 (c), the photon energy dependence of Cu 3d and O 2p atomic levels cross section does not exhibit the same tendency. By

exploiting the commutation relation $\hbar \mathbf{p}/m = -i[\mathbf{x}, H]$, we can write the Matrix element in this form

$$I_0(k, v, \mathbf{A}) \propto |M_{f,i}^{\mathbf{k}}|^2 \propto |<\phi_f^k|\epsilon \cdot \mathbf{x}|\phi_i^k>|^2 \propto |<\phi_f^k|\mathbf{A} \cdot \mathbf{p}|\phi_i^k>|^2 \qquad (2.24)$$

where ϵ is the unit vector depending on the polarization direction of vector potential ($\mathbf{A}$). In order to have the photoemission intensity, the whole integrand must be an even function. Normally, the final state wave function (ϕ_f^k) always be even function. Then, the $\mathbf{A} \cdot \mathbf{p}|\phi_i^k>$ must be an even function. The result of $\mathbf{A} \cdot \mathbf{p}$ can be odd or even depending on the light polarization (odd is normal to the mirror plane and even is parallel to the plane). Moreover, the initial state wave function can be either even or odd depending on the orbital symmetry in each state. The overall even function which result to the photoemission intensity can be expressed as

$$<\phi_f^k|\mathbf{A}.\mathbf{p}|\phi_i^k> = \begin{cases} <+|+|+>: \phi_i^k \text{ and } \mathbf{A} \cdot \mathbf{p} \text{ are even} \\ <+|-|->: \phi_i^k \text{ and } \mathbf{A} \cdot \mathbf{p} \text{ are odd} \end{cases}$$

2.7.4 Charging effect

In ARPES, after the sample is irradiated by the pulsed light, the escaping photoelectrons will experience the energy redistribution from the Coulomb interaction. This is called charging effect which causes the energy shift and broadening in order of 10 meV for conducting sample in high resolution synchrotron light source. Figure 2.8 (a) shows the Fermi edge broadening and Fermi edge shift of gold as a function of sample current (Zhou et al., 2005). This indicates a large uncertainty caused by charging effect even measuring in good conducting environment. This might be the main obstacle for fundamental studies especially in high-temperature-superconductors or strongly-correlated system (Damascelli,

2004). In the present, to aid such studies requires very high resolution in range of few meV. In the photoemission process, because of the Coulomb interaction, the fast electrons is likely to be pushed by the electrons behind them while the slow one is being retarded. This reason will distort the intrinsic information by broadening the distribution of the encountered electrons. The systematic shift in energy is strongly dependent on the kind of accumulation on the surface. The typical accumulation is introduced as hole accumulation which drive the valence band to lower binding energy.
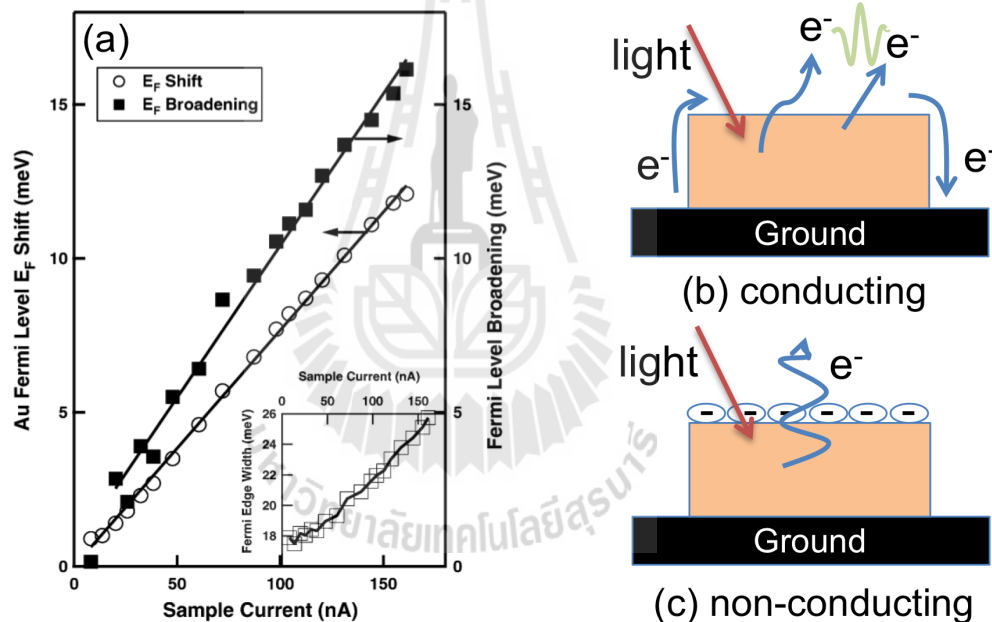
Figure 2.8 a) Fermi edge broadening and the Fermi edge shift of gold as a function of sample current (Zhou et al., 2005). b) and c) Schematic Illustration of how charging effect happened in non-conducting and conducting samples.

According to a large number of materials can be measured using ARPES. From the previous report, the minimum of 10 meV resolution is introduced by charging effect in the third-generation synchrotron. However, in fact, charging

effect is one of the major problem in ARPES especially in non-conducting materials. This effect may give the energy shift up to hundreds meV caused by charge accumulation on the surface. In conducting material, this should not be a problem because the electrons move freely in the sample and fill the missing electron. However, for non-conducting material, the electrons are accumulated on the sample surface induced the electric field (summarized in figure 2.8 (b) and (c)). This electric field will block the photoemission process and sometimes interrupt all information. Grounding is the best way to prevent the sample from charging effect. The sample has to be mounted with conducting holder (copper is typically used) by conducting glues. Commonly, the bounding process can be done by spraying the graphite covering all the sample to ensure that the sample is electrical contacted with the holder. During the measurement, some charging evidences like unsteady binding energy or blurred spectrum may happen. There are two typical techniques to suppress the charging effect. Firstly, reducing the light exposure will help to decrease the number of photoelectron (reducing the surface accumulation.) Secondly, increasing the temperature which help the sample to be more conducting by its nature. Anyway, the data quality may be worse because lower photoelectrons are ejected out compared with the presence of Fermi-Dirac distribution. Adding the alkali ions such as K^+ may help to restore the charged-surface with electron donation as well.

2.7.5 Potassium evaporation in ultra high vacuum

Potassium is the chemical element of group IA in the periodic table which has been known as very reactive element. In this work, the high purity of potassium source (potassium SAES-dispenser) is placed in UHV to avoid the air exposure. To evaporate the potassium, firstly, we turn the current to be around 3
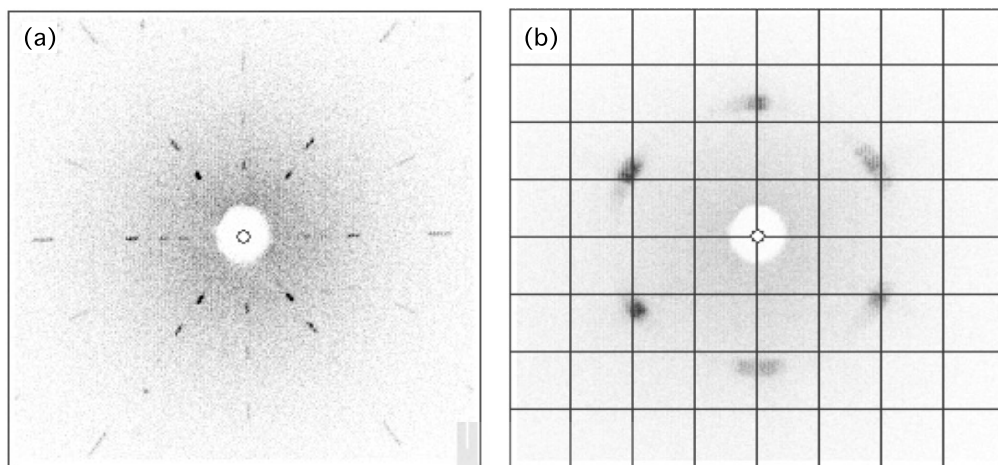
Figure 2.9 a) Laue pattern of STO (110) reflecting to the perfect rectangle shape with sharp spots. b) Hexagonal pattern of MoS_2, vertically align along $\bar{\Gamma} - \bar{K}$ direction.

A for about a minute to clean some contaminations from the source (degassing). Then, the sample is moved to face the potassium dispenser. We then apply the current of more than 4 A (evaporation rate depends on the applied current) which is the exact calibrated value to heat the dispenser above the potassium's boiling point. After the current is more than boiling point of potassium, the pressure enhances dramatically in this progress. This evidence confirms that potassium source has already produced the heat inside the chamber and evaporated out of the dispenser to the sample surface. Other alkali metal evaporation in UHV will also be operated with this similar process.

2.7.6 Preparation of MoS_2 for ARPES measurement

2H-MoS_2 single crystals (from Prof. Takao Sasagawa) were grown using flux growth method. To prepare the sample for measuring, first of all, we mounted the
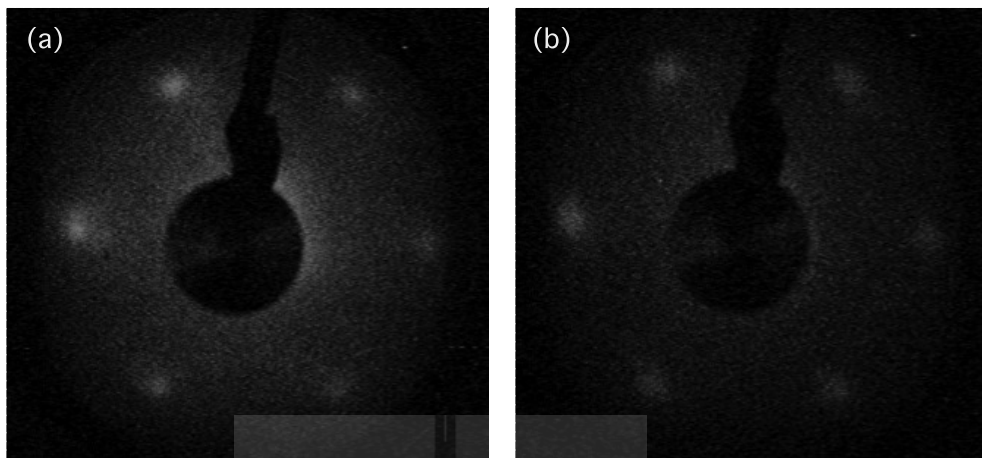
Figure 2.10 a) and b) LEED pattern of MoS_2 carried out at voltage of 173 V before and after potassium evaporation. The blurred image of (b) supports the coverage of potassium on MoS_2 right after the evaporation.

MoS_2 samples on the copper posts and ground them by using silver epoxy (EPO-TEK H21) which is electrically conductive and vacuum compatible. Then, we checked the sample orientation, crystal structure, and the type of crystal (single- or poly-crystals) by exploiting the Laue-x-ray diffraction measurement with 25 kV and 20 mA. This step is very helpful to reduce the measuring time because the geometry and perfection of the sample (multiple or single domain) is revealed in this state. Figure 2.9 shows the example of the Laue-diffraction pattern of the STO (110) perfect crystal and the MoS_2 single crystal which have been aligned in $\bar{\Gamma}$–$\bar{K}$. After Laue measurement, the sample is then recognizably marked and pinned with an alumina post for cleaving in UHV. After the sample is cleaved, the sample orientation can be checked again by the surface sensitive diffraction (LEED). Finally, XPS, LEED, and ARPES can be performed before and after Potassium evaporation.

CHAPTER III

OTHER RELATING THEORETICAL

ASPECTS

In this chapter, I would like to explain about the semiconductors and their dopings (extrinsic semiconductors) which are related to the property of some TMDs (semiconducting TMDs) in my research. The intercalation reaction process in the ambient pressure and ultra high vacuum will be discussed in this chapter. The electronic structure derived from reciprocal lattice as well as spin-orbit interaction and band bending will also be presented.

3.1 Semiconductor

3.1.1 Indirect and direct band gap semiconductors

The band gap represents the energy difference between the valence band maximum (VBM) and the conduction band minimum (CDM). The direct band gap semiconductor is the material that the VBM and CBM are located at the same electron momentum. On the other hand, if the VBM and CBM are not located at the same momentum, this kind of material will be called as "an indirect band gap semiconductor".

The obvious difference between indirect and direct band gap semiconductors are described in term of optical property. Using the equation for light with the quantum nature, the photon with energy (E) will have momentum (p) expressed

in this equation

$$p = \frac{E}{c}, \tag{3.1}$$

where c is the velocity of light $= 3 \times 10^8$ m/s. Estimated optical energy of light has an energy in order of 10^{-19} J; therefore the momentum of photon is very small.

In general, exposing photon into the material produces some electron-hole pairs in the material. These pairs can easily be occurred in direct band gap semiconductors because the electron does not need a momentum transfer in such process. However, the electron-hole pair could also be produced in an indirect band gap semiconductor but requires additional factor of momentum translation caused by a lattice vibration called "phonon". This factor makes the process of electron-hole pairs much more complicated and less probable. Types of band gap and the band gap value can be determined using absorption spectroscopy. The absorption peak will be observed when the incident photon starts to have energy a little higher than the band gap of the probed semiconductor; this photon energy at the onset will be equal to the band gap. We can predict the type of semiconductor by plotting the absorption coefficient (α). If a plot of $h\nu$ versus α^2 in the material is a straight line, we can conclude that there is a direct band gap nature. In the other hand, if a plot of $h\nu$ versus $\alpha^{1/2}$ forms a straight line, it can normally be inferred that there is an indirect band gap semiconductor (Pankove, 1971; Rosencher and Vinter, 2002).

3.1.2 Extrinsic semiconductors

Semiconductors can be divided into two types. The undoped semiconductor is called as "intrinsic semiconductor" while the doped semiconductor is called as "extrinsic semiconductor". In this section, I will focus only the extrinsic semiconductors (ESs). ESs have gained much of scienctific interest because

their properties can be enhanced after various doping to the intrinsic semiconductor (Thongbai et al., 2009; Jiamprasertboon et al., 2014). Many ESs have been used as components of many common electrical devices such as diodes (allowing current in one direction), transistors (switching current) and field effect transistors. They have also been applied in the use of lasers, solar cell, and photodetectors. The ESs have been classified as either p-type or n-type semiconductor depending on the additional doping. P-type semiconductor is introduced by doping with the acceptor to the intrinsic semiconductor; this give extra holes in the system (e.g. B(III) doped in Si(IV)). On the other hand, n-type semiconductor refers to the adding of donor impurity which gives the extra electron into the system (e.g. As (V) doped in Si (IV)). Both of p- and n-type doping can move the Fermi level or chemical potential in the semiconductor expressed by this equation

$$E_F = E_v + kT \ln \frac{n_D}{n_A} \tag{3.2}$$

E_F is referred to the Fermi level. E_v stands for the valence band energy and n_D (n_A) is referred to the donor (acceptor) impurity in the semiconductor. From above equation, we can conclude that the Fermi level can move toward valence band in p-type semiconductor while the Fermi level of n-type semiconductor enters the valence band. So, the Fermi level of semiconductors can be tuned by adding some extra impurity which may effect to the material property.

3.2 The intercalation reaction

Some crystal structures which have free spaces allowing atoms, ions or molecules, can be inserted into the compounds of layered structure generally defined as intercalation (Papageorgopoulos and Jaegermann, 1995). The intercalated systems give rise the emergence of novel properties especially in layered materials.

The superconductivity has been observed in alkali metal doped MoS_2 (Ye et al., 2012) and the outstanding properties such as electrochemical energy storage have also been observed in intercalation of Li-MoS_2 (Friend and Yoffe, 1987; Jacobson and Whittingham, 1982). As mentioned, this method is very promising in order to create the large area monolayer TMDs using for novel ultimate applications and fundamental studies. C. Riedl et al. discovered the quasi-freestanding of graphene which is caused by the reconstruction of initial carbon layer on SiC using hydrogen intercalation (Riedl et al., 2009). The plasmaron in quasi-freestanding doped graphene has also been observed recently (Bostwick et al., 2010).

Depending on crystal dimension in materials, intercalation may result in various cavities, tunnels, and planes. The nature and amount of the intercalated guest compound will result in different chemical and physical properties from the host material. The simple chemical reaction is given when x mol of guest A intercalated in host MX_2 as

$$xA + MX_2 \rightarrow A_xMX_2 \tag{3.3}$$

In an ideal case, if the intercalation process undergoes with no distortion in the host structure, the c-axis expansion is considered to be the main effect in TMDs according to its weak vdW interaction. Several alkali metals or transition metals intercalated in TMDs have been observed with c-axis elongation (Mrstik et al., 1977; Kadowaki and Aika, 1993; Fujimori et al., 1988). Interestingly, the expansion is dependent on the size of intercalated atoms observed in TMDs with 0.5 $\mathring{A}$ and 1.5 $\mathring{A}$ with Li and Na intercalation, respectively (Jacobson and Whittingham, 1982). Moreover, the spatial coordinate transition of host structure may occur in the intercalation process. Particularly, Rouxel et al. have studied about the intercalated alkali metal of group IVb TMDs extensively. They claimed that not only c-axis expansion but also the phase transition will occur in the most of TMD
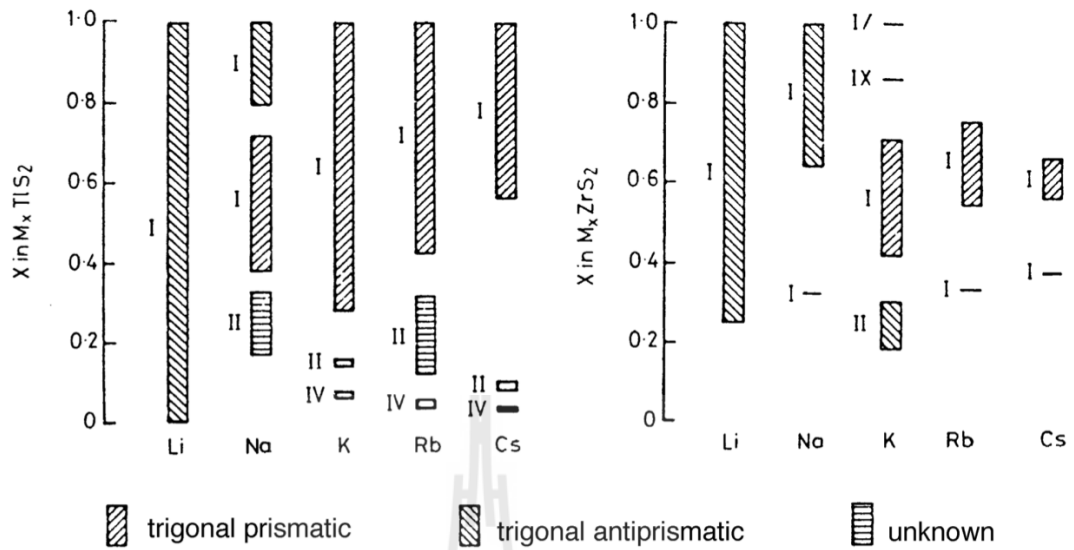
Figure 3.1 Phase formed by different alkali metal intercalation in TiS_2 and ZrS_2 (Rouxel, 1979).

intercalated systems as illustrated in figure 3.1. In TMDs, only donor intercalation is possible for alkali metal intercalation. This donor intercalation reaction can be written as

$$xA + MX_2 \rightarrow A^{x+}(int) + MX_2{}^{x-} \tag{3.4}$$

Intercalation process will change the bond angles and distances in TMDs, resulting in phase transition in some TMDs. For example, Li intercalated in TaS_2 induced a phase transition from 1T to 2H (Ganal et al., 1993), and the transition from 2H to 1T was observed in Li-MoS$_2$ (Imanishi et al., 1992). The intercalation of alkali metal into TMDs causes the donation from the valence electron in s orbital of alkali guest to d orbital of host metal. This has been predicted by rigid band model (Friend and Yoffe, 1987). In this process, the conduction band is filled up, the Fermi level moves upward, and the significant changes of the band dispersion

in the host material are presented. These variation can be directly observed by ARPES (Biagi et al., 2003).

3.2.1   Alkali metal intercalation in ultra high vacuum

The intercalation in ultra high vacuum (UHV) is essential in this work. This technique is rather simple and useful when performing within ARPES system which is already setup in the UHV environment. The *in situ* sample preparation in UHV is required to perform this technique to avoid the air exposure. After TMD single crystals were cleaved in UHV, the alkali metal can be directly evaporated (explained in section 2.7.5) which may induce the adsorption or intercalation process on the sample surface (Rossnagel, 2010). Layered TMDs are one of the simple substrates which can be involved in the intercalation after evaporation process. The deposition rate can be obtained either using the calibration of non-intercalated substrate or deposition time. The intercalated amount is increased directly with the deposition time but the value is limited by the type of crystal substrate. This process allows us to measure the development of band dispersion in the term of deposition time (will be discussed later). Intriguingly, the reversible process of intercalation called "deintercalation" is an interesting technique as well. For example, the reversible process of metal evaporation/air exposure (or putting the sample in electrochemical process) of TMDs allows us to switch on/off the properties in this kind of intercalation system, respectively (Adelsberger et al., 2001a; Adelsberger et al., 2001b).

3.3   Reciprocal lattice

To understand the real space lattice structure or electronic structure requires the knowledge of reciprocal lattice. Methods such as XRD or ARPES can

be built and understood by exploiting the knowledge of reciprocal lattice. Because light behaving like matter-wave, this leads to the relation between spatial and momentum space through the de Broglie relation (previously explained in section 2.5.2). This condition is well known as Bragg's law (further information provideed in XRD section). In crystal, atoms are periodically arranged in three dimensional real space lattice. The characters of the lattice have been defined as unit vectors $\mathbf{a}$, $\mathbf{b}$, and $\mathbf{c}$ with angles α, β, and γ, respectively (see figure 3.2 (a)). All atoms in the perfect lattice are equivalent in one reference point. The neighbouring atoms can be expressed in term of translation vector ($\mathbf{T}$) given by

$$\mathbf{T} = n_1\mathbf{a} + n_2\mathbf{b} + n_3\mathbf{c} \qquad (3.5)$$

where n_1, n_2, and n_3 are integers. We can define the plane and direction of the real space lattice by using this translation vector (eq. 3.5). The defined plane is generally used to indicate the sample orientation. The direction of sample plane can be written in the format of integer triplet $[n_1 n_2 n_3]$. For example, the chosen translation vector ($T_1 = 1\mathbf{a} + 1\mathbf{b} + 1\mathbf{c}$) refers to the integers $n_1 = n_2 = n_3 = 1$. The plane of vector is denoted by [111]. The plane orientation can be specified by the interception of the number straight up to the basis vectors. In case of the [001] plane of cubic lattice, the plane is cut through z-axis giving the xy-plane normal to z-axis.

To understand the relationship between real and reciprocal lattice, we have introduced the reciprocal lattice vector $\mathbf{G}(hkl)$ to describe the lattice behaviour. The real space lattice vector ($\mathbf{R}$) is equivalent to $\mathbf{T}$. The condition of periodic structure will always satisfy the following equation
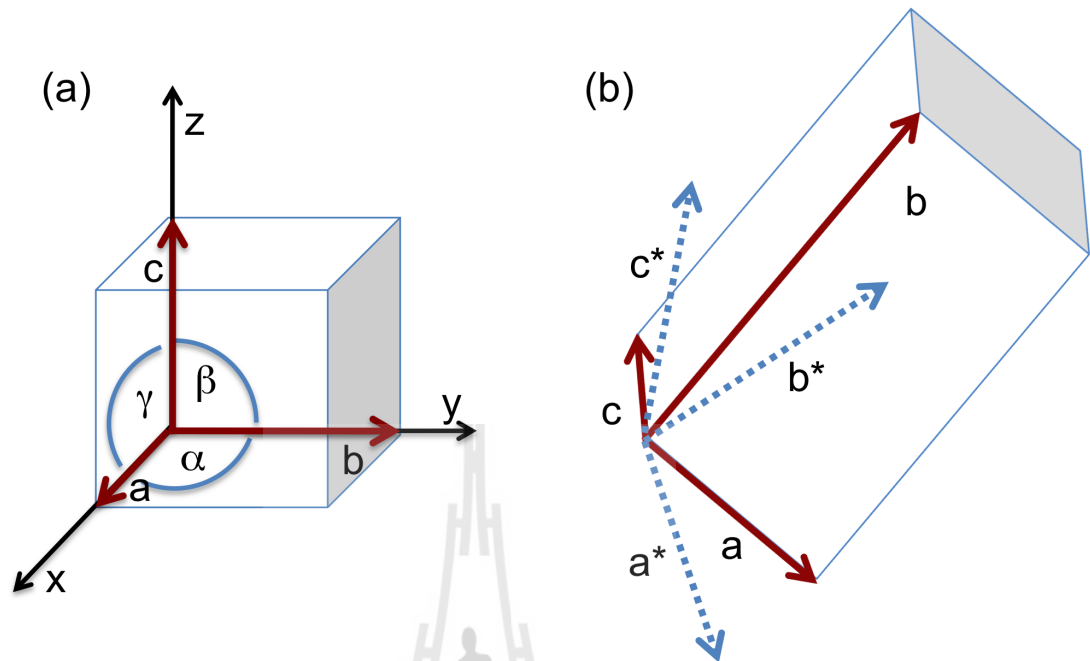
Figure 3.2 a) A unit cell with three basis vectors $\mathbf{a}, \mathbf{b}$, and $\mathbf{c}$ with the respected angles of α, β, and γ. b) Illustration of reciprocal lattice vectors, $\mathbf{a}^*, \mathbf{b}^*$, and $\mathbf{c}^*$ relating to the real space vectors.

$$e^{i\mathbf{G}\cdot\mathbf{R}} = 1$$

$$where \ \mathbf{G} \cdot \mathbf{R} = 2\pi n \tag{3.6}$$

The reciprocal lattice is commonly defined as

$$\mathbf{G}(hkl) = h\mathbf{a}^* + k\mathbf{b}^* + l\mathbf{c}^* \tag{3.7}$$

where h, k, and l are the Miller indices of a crystal plane. The (hkl) is referred to the reciprocal unit vector illustrated in figure 3.2 (b). By mathematical satisfaction, the reciprocal lattice vectors must be in the form of

$$\mathbf{a}^* = 2\pi \frac{\mathbf{b} \times \mathbf{c}}{\mathbf{a} \cdot (\mathbf{b} \times \mathbf{c})}, \ \mathbf{b}^* = 2\pi \frac{\mathbf{c} \times \mathbf{a}}{\mathbf{a} \cdot (\mathbf{b} \times \mathbf{c})}, \ \mathbf{c}^* = 2\pi \frac{\mathbf{a} \times \mathbf{b}}{\mathbf{a} \cdot (\mathbf{b} \times \mathbf{c})} \tag{3.8}$$

In the simple hexagonal lattice, the xy- and z-plane are defined by $\mathbf{a}$ and $\mathbf{c}$. The reciprocal lattice is still be in hexagonal form but its axis is substituted by $\frac{4\pi}{a\sqrt{3}}$ and $\frac{2\pi}{a}$ rotating $30°$ around c-axis respected to the real space lattice. The high symmetry points are generally given to simplify the direction respect to the hexagonal shape shown later in figure 5.1 (a). The electronic structure of the materials are described through the points in reciprocal space.

3.4 Spin-orbit interaction

The spin-orbit interaction (SOI) is an interaction between orbital angular momentum ($\mathbf{L}$) and spin ($\mathbf{S}$) in the particle. When electron moving around the nucleus, this gives the interaction between electron's spin and the magnetic field generated by the electron's orbit around the nucleus. This interaction causes many effects in electronic structure such as shifts of spectral lines in atomic energy level and momentum splitting in 2DEG materials (Rashba effect). SOI plays an important role to manipulate the electron's spin in the materials.

SOI can be derived in many different ways using the knowledge of electrodynamics and quantum mechanics. The simple and quantitative SOI is expressed using the first order perturbation while more precise result would be discussed in terms of Dirac equation and quantum electrodynamics. The derivation of SOI, Rashba effect, significant values, and applications in materials will be introduced in this section. Firstly, the energy of the electron (ΔH) in the magnetic field is given by

$$\Delta H = -\mu \cdot \mathbf{B} \tag{3.9}$$

where μ = electron magnetic moment and $\mathbf{B}$ is the experienced magnetic field. Acquirement of these values are significant and will be expressed sequentially. Secondly, while electron is moving around the nucleus with the velocity (v), it will generate the radial function of electric field ($\mathbf{E}$) in the form of

$$\mathbf{E} = \frac{1}{e}\frac{\vec{r}}{r}\frac{dV}{dr} \tag{3.10}$$

In the electron's rest frame, the recognition magnetic field on electron is transformed from the generated electric field given by

$$\mathbf{B} = -\frac{v \times \mathbf{E}}{c^2} \tag{3.11}$$

where c is speed of light. By using the relationship between electron momentum ($\mathbf{p}$) and angular momentum ($\mathbf{L}$) of $\mathbf{p} = m \cdot v$ and $\mathbf{L} = r \times \mathbf{p}$, we can then substitute eq. 3.10 into eq. 3.11 giving

$$\mathbf{B} = \frac{1}{m_e e c^2}\frac{1}{r}\frac{dV}{dr}\mathbf{L} \tag{3.12}$$

The above equation stands for the magnetic field in which electron is experienced by its motion. Next, the magnetic moment value is given by

$$\vec{\mu} = -g_e \mu_B \frac{\mathbf{s}}{\hbar} \tag{3.13}$$

where g_e is the g-factor of electron = 2.002 (Odom et al., 2006). Bohr magnetron (μ_B) is calculated by $\mu_B = \frac{e\hbar}{2m_e}$. The total interaction energy is contributed from the interaction of the electron's magnetic moment and the nucleus's magnetic field. This interaction is well known as "Larmor interaction energy". Actually, this interaction will always be reduced with the Thomas precession giving the expression of total interaction energy as

$$\Delta H = -\frac{\mu_B}{\hbar m_e e c^2}\frac{1}{r}\frac{dV}{dr}\mathbf{L}.\mathbf{S} \tag{3.14}$$

This equation is equal to the half of the interaction energy which is known as "Thomas half". After above approximation, the energy shift can be evaluated by introducing the total angular momentum ($\mathbf{J}$) which is defined by

$$\mathbf{J} = \mathbf{L} + \mathbf{S} \tag{3.15}$$

After deriving $\mathbf{J}$ terms, finally, we got

$$\Delta H = \frac{\beta}{2}(j(j+1) - l(l+1) - s(s+1)) \tag{3.16}$$

ΔH is the total energy shifts of spin degeneracy ($s = \pm\frac{1}{2}$) where

$$\beta = \beta(n,l) = Z^4 \frac{\mu_0}{4\pi} g_s \mu_B^2 \frac{1}{n^3 a_0^3 l(l+\frac{1}{2})(l+1)} \tag{3.17}$$

On the other hand, the more quantitative approach of SOI is generally described in the term of relativistic behaviour of electron using Dirac equation (Dirac, 1928) which can be expressed as

$$(c\vec{\alpha}\,\vec{p} + \vec{\beta}m_e c^2 + V)\Psi = E\Psi \tag{3.18}$$

where

$$\vec{\alpha} = \begin{pmatrix} 0 & \vec{\sigma} \\ \vec{\sigma} & 0 \end{pmatrix}$$

and

$$\vec{\beta} = \begin{pmatrix} 1 & 0 \\ 0 & -1 \end{pmatrix}$$

The Pauli spin matrices is introduced as, $\vec{\sigma} = (\sigma_x, \sigma_y, \sigma_z)$. The selected wave function is in the form of $\Psi = (\Psi_A, \Psi_B)$. Eq. 3.18 can be rewritten as

$$\vec{\alpha}\,\vec{p}\,\Psi_B = \frac{1}{c}(E - m_e c^2 - V)\Psi_A$$
$$\vec{\alpha}\,\vec{p}\,\Psi_A = \frac{1}{c}(E + m_e c^2 - V)\Psi_B \tag{3.19}$$

From eq. 3.19, we can eliminate Ψ_A (or Ψ_B) by substituting the equation itself. The substituted equation should be expressed in the new form of

$$\overrightarrow{\alpha}\,\overrightarrow{p}\,(\frac{c^2}{E+m_ec^2-V})\overrightarrow{\alpha}\,\overrightarrow{p}\,\Psi_A = (E+m_ec^2-V)\Psi_A \tag{3.20}$$

Finally, by approximation in non-relativistic limit, the Pauli equation for spherically symmetric potential is obtained which can be expressed as

$$(\frac{p^2}{2m_e}+V-\frac{\hbar^2}{4m_e^2c^2}\frac{dV}{dr}\frac{\partial}{\partial\vec{r}}+\frac{1}{2m_e^2c^2}\frac{1}{r}\frac{dV}{dr}\vec{l}\vec{s})\Psi_A = E\Psi_B \tag{3.21}$$

The first two terms represent the total energy of electron under Coulomb potential. The third term is known as Darwin term. The fourth term is Pauli SOI, this is strongly dependent on $\frac{dV}{dr}$ term which is proportional to atomic number (Z). Therefore, the huge SOI is expected to be formed in the heavy element with high atomic number.

3.4.1   Inversion symmetry and time-reversal symmetry

In free atoms, the SOI suggests that the spin degeneracy in energy level can be split into parallel and antiparallel to the orbit according to the spin up and spin down of electron wavefunction. However, this splitting can be neglected in very high symmetry system; i.e. in solids. The time-reversal symmetry (TRS) in the crystal is proposed to the same energy at opposite momentum after flipping the spin of electron. This symmetry plays an important role in the SOI system and can be expressed as

$$E(k,\uparrow) = E(-k,\downarrow) \tag{3.22}$$

Moreover, in the inversion symmetry (IS) case, atomic positions will locate at the same position after operates with $r \rightarrow -r$). In momentum space, we can write an expression to the electronic structure by

$$E(k,\uparrow) = E(-k,\uparrow) \tag{3.23}$$

The inversion symmetry and time-reversal symmetry always exist in the perfect three-dimensional solids. By combining eq. 3.22 and 3.23, this should be implied that there is no spin degeneracy at all momentum space in perfect crystal as

$$E(k, \uparrow) = E(k, \downarrow) \tag{3.24}$$

Breaking symmetry will give the energy splitting in the system which will be discussed in the next section.

3.4.2   The Rashba spin-orbit coupling

The spin degeneracy is suppressed when both of TRS and IS exist. If one of these symmetry is broken, the spin degeneracy can be lifted by SOI. The absence of spatial inversion symmetry can be separate into either bulk inversion asymmetry (Dressslhaus effect) or structural inversion asymmetry (Rashba effect). In 2D case, the structural inversion symmetry is broken in the out of plane direction of semi infinite crystal formed to be the 2D electron gas (2DEG) system. The electron in 2DEG-like system is confined in the (x,y)-plane becoming spin-polarized resulted from inversion asymmetry along the z-direction. The Rashba hamiltonian of this system can be written as

$$H_{RB} = \alpha_R \vec{\sigma}(\vec{k}_{//} \times \vec{e}_z) \tag{3.25}$$

where α_R = Rashba constant, $\vec{\sigma}$ is Pauli matrices, $\vec{k}_{//}$ is the in plane momentum. This Hamiltonian can be analytically solved by using Cartesian coordinate in a nearly free electron model. The analytical solution is given by

$$E_{1,2} = E_0 + \frac{\hbar^2 k_{//}^2}{2m^*} \pm \alpha_R k_{//} = E_0 + \frac{\hbar^2}{2m^*}(k_{//} \pm k_R)^2 \tag{3.26}$$
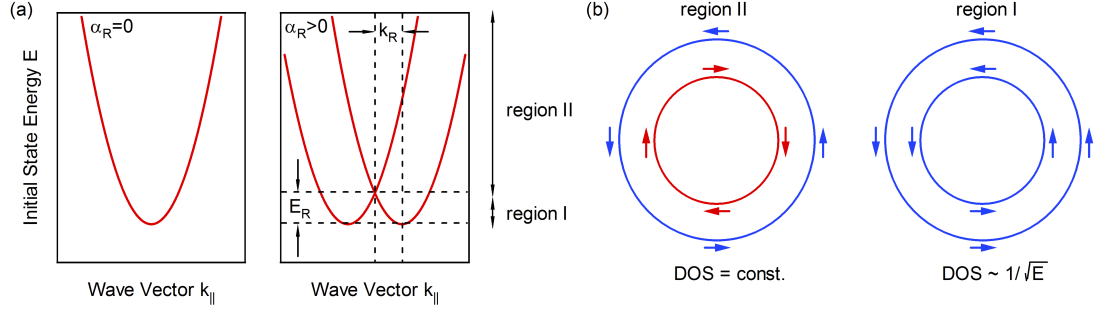
Figure 3.3 a) Dispersion of the 2D free electron gas without (left) and with (right) Rashba SOI. b) Constant energy contours of region II and region I with corresponding spin polarization (Gierz, 2011).

with the associated wave function in energy of

$$\phi_1(r) = e^{i\vec{k}\vec{r}}(|\uparrow> + ie^{i\theta_k}|\downarrow>)$$

$$\phi_2(r) = e^{i\vec{k}\vec{r}}(ie^{-i\theta_k}|\uparrow> + |\downarrow>) \tag{3.27}$$

The above solutions give two electron parabola shifted in k direction offset by factor of $\frac{\alpha_R m^*}{\hbar^2}$ at the same energy. Figure 3.3 (a) shows the band dispersion of 2DEG with and without Rashba SOI. Starting from the non-SOI, the parabolic band is spin degeneracy with spin up and spin down. Breaking TRS can lead to the splitting of two parabolas and constraint two spin-polarized parabola cross at the opposite energy and spin. The behaviours of energy contour are different at the upper and lower critical energy ($E = E_R$). In the case of $E > E_R$, the spins are anti-rotating. While, in the case of $E < E_R$, spins rotate in the same way as shown in figure 3.3 (b).

3.4.3 Simple description of spin-orbit interaction in solids

The spin-orbit interaction is different in each region of the Brillouin zone. When considering at the $\bar{\Gamma}$ point (k=0), TRS and IS do not affect with the band
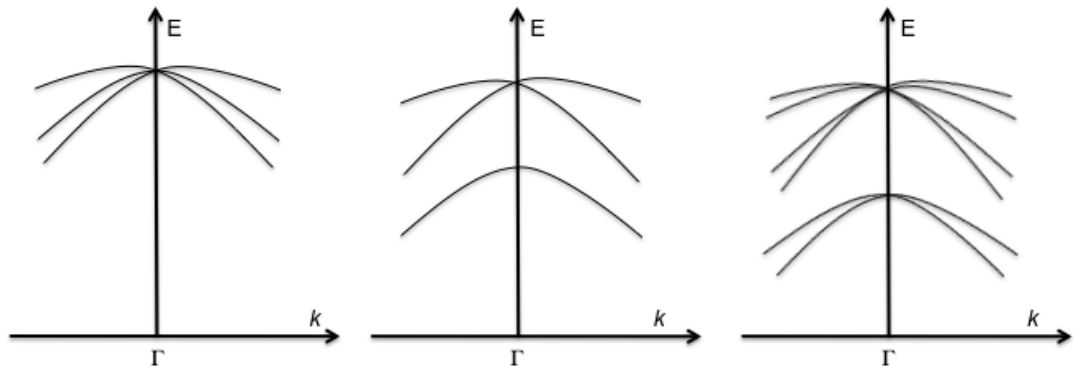
Figure 3.4 Example of spin-orbit interaction on the six-degenerated p orbital. a) Without SOC, only one band are visible due to the degeneracy at Γ point b) SOC causes the splitting of $p_{3/2}$ and $p_{1/2}$ levels. c) SOC with inversion asymmetry, the spin degeneracy is fully removed.

structure. However, at the point far away from the center, these effects will give some splittings in the electronic structure. Here, the spin degeneracy in the simple p orbital model will be discussed. Starting with p wave function, there are three bands with two spin degeneracy each. In a free atom without SOI, these bands are overlapped at the $\bar{\Gamma}$ point (figure 3.4 (a)). The spin degeneracy at $\bar{\Gamma}$ has been generated after the spin-orbit interaction taking into account caused by two subbands of $p_{3/2}$ and $p_{1/2}$ orbital degeneracy (shown in figure 3.4 (b)). Moreover, if the inversion symmetry is breaking (i. e. material surfaces and 2DEGs), the $p_{3/2}$ and $p_{1/2}$ states will be lifted by the spin degeneracy revealing all six bands in the p orbital behaviour (figure 3.4 (c)).

The large spin-orbit coupling in TMDs can occur because these materials consist of the heavy atom from d orbitals. Either 4d or 5d transition elements have been known to have a very strong spin-orbit coupling (SOC) (Pesin and Balents, 2010). SOC removes spin degeneracy in the spin up and spin down states in the

material. The splittings in both conduction band and valence band in TMDs can be occurred if the SOC is strong enough. Especially, TMD monolayers whose exhibit the inversion asymmetry are subjected to have a large spin-orbit splitting. In our interested sample, the spin-orbit splitting of MoS_2 has been theoretical predicted to be about 0.148 eV and 3 meV at valence band and conduction band respectively (Liu et al., 2013).

3.5 Band bending at the surface

At the surface or interface of a material, both bulk and surface states are allowed due to the broken of perfect periodic structure near the junction. The simplified band structure can be derived from one-electron and mean-field approximation written as

$$H = \frac{\mathbf{p}^2}{2m_e} + V_0(\mathbf{r})$$ (3.28)

where $V_0(\mathbf{r})$ stands for the periodic potential, then the solutions of this equation are called Bloch wave functions (Ridley, 1999) introduced by

$$\psi_k(\mathbf{r}) = \mu_{\nu\mathbf{k}}(\mathbf{r})exp(i\mathbf{k} \cdot \mathbf{r})$$ (3.29)

In the bulk (perfect periodic system), only real parts of Bloch wave functions are allowed. The surface electronic states exist within the semiconductor band gap by providing the boundary condition. Since the wave function need to be continuous across the interface between bulk and vacuum, to achieve that, there must be surface state near that interface (Heine, 1965). This will allow the Bloch wave function which is derived from the Schrödinger equation to be complex number (surface state) rather than real number (bulk state). Normally, the density of the surface state is large when compared to the bulk of the semiconductor. Then, the Fermi level of any localized surface/interface systems (Fermi level pin-

ning (Bardeen, 1947)) will be dominated by the surface state. To control this surface state, one way is to control the band bending at the surface. The band bending refers to the local changes of the electronic energy in band structure which was first studied by Schottky and Mott (Schottky, 1938). This band bending which is necessary to create the 2DEG usually affects the band structure especially at the Fermi level of the material. The study of band bending can be applied to ion diffusion in metal oxides, chemicurrent or gate voltage measurement (Cabrera and Mott, 1949; Nienhaus, 2002).
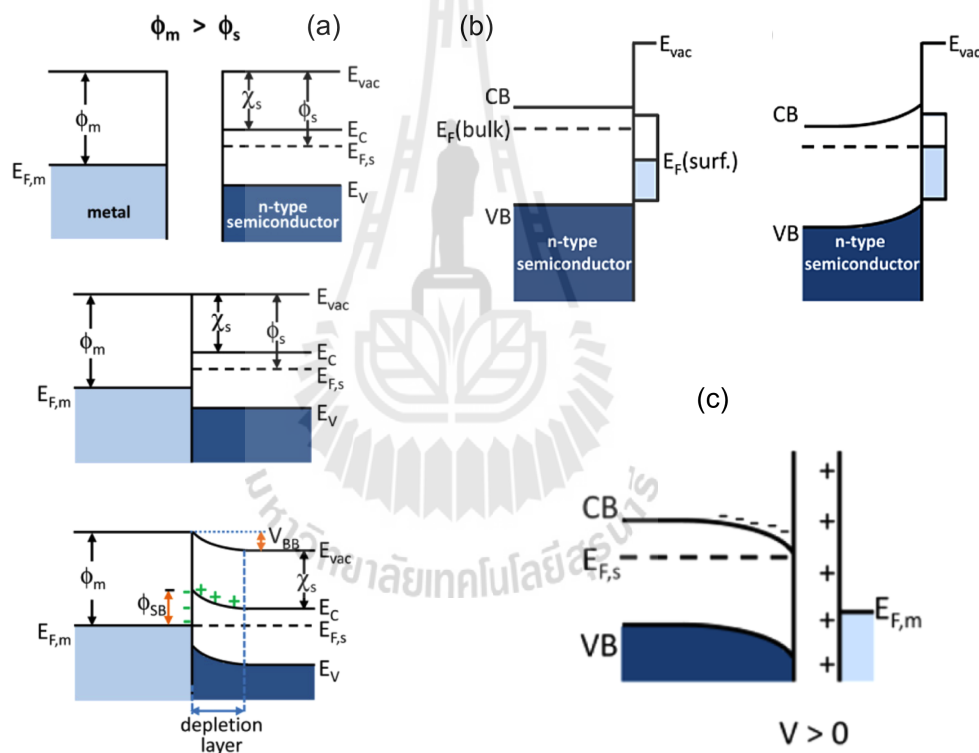
Figure 3.5 Energy band diagram of n-type semiconductor including the appearance of band bending after the perturbation of a) contact to metal with higher work function b) surface state induced band bending and c) positive field effect (adapted from (Zhang and Yates, 2012)).

Because the surface state is always quickly fading through the vacuum

level or the bulk of the semiconductor according to the screening effect, the good conditions used to optimize the screening factor are required to manipulate the 2DEGs. Band bending can occur when there is a change of carrier density at the surface/interface of the semiconductor. Carrier exchanges are the bending of the band when electrons or holes transferred from one to another junction which can be presented in many ways. For example in the contact of metal/n-type semiconductor with metal work function greater than semiconductor ($\phi_m > \phi_s$) (figure 3.5 (a)), electrons will flow from semiconductor to metal leading to the upward band bending. The Fermi level also shifts downward until both ends having the same Fermi level. Band bending can be occurred under applying field effect (downward band bending when applying $V > 0$ (figure 3.5 (b))). Essentially, surface state or adsorption can be induced band bending which is strongly related to our researches. Figure 3.5 (c) represents the schematic of n-type semiconductor (related to the electron surface adsorption). The Fermi level of bulk material is get higher than Fermi level of the surface. Then, electrons will move from bulk to surface state until equilibrium. We may see the 2DEG state (surface state) if they are occupied at the Fermi level.

However, band bending can also be derived by the space charge effect. This will support or suppress the band bending effect depending on the study system. The screening length is high in order of $\sim 100 \; \mathring{A}$ in semiconductor with a carrier density $\sim 10^{17} cm^{-3}$ and is ascended in less density semiconductor. Figure 3.6 (a) shows the electron accumulation (left) and depletion (right) of n-type semiconductor. In case of the positive charged-surface states, negative space-charge will be accumulated in the semiconductor near the surface to maintain the charge neutrality respected to the bulk. This is achieved by a downward band bending and vice versa for the depletion layer. We can measure the band bending
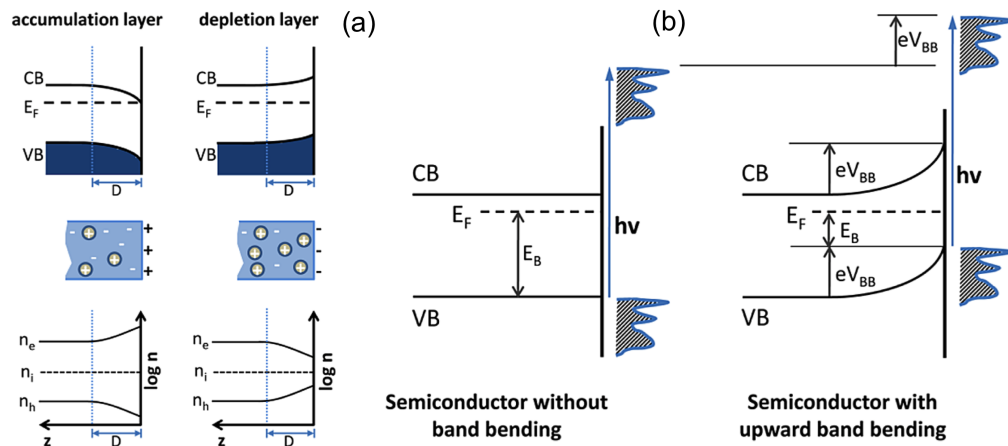
Figure 3.6 a) Schematic illustration of space charge region including the band bending resulting from charge accumulation and depletion layer from the n-type semiconductor. b) Diagram of binding energy shifting obtained by photoemission spectra resulting from the upward band bending (Zhang and Yates, 2012).

and also 2DEGs by ARPES. This is an ideal tool to probe the band structure and the band variation caused by the band bending in the semiconductor. Figure 3.6 (b) shows the diagram before and after upward band bending process of a semiconductor. If the upward band bending occurs near the surfaces, we may see the binding energy shift towards the Fermi level. In contrast, for downward band bending, the shift will be in opposite direction. Moreover, if the bending is large enough, we can also measure 2DEGs from the bulk or surface state which is very interesting topic in the current researches.

CHAPTER IV

TWO-DIMENSIONAL ELECTRONIC

STRUCTURES

In this chapter, I will describe our relating studies of the 2D electronic structure of transition metal oxides focusing on $SrTiO_3$ and $KTaO_3$. In this study, I have collaborated with the famous research group led by Asst. Prof. Worawat Meevasana from Suranaree University of technology and Dr. Philip King from the University of St Andrews. The knowledge gained from this project is very important to understand the more complicated electronic structure of layered-TMDs which will be described in the next chapter.

2D materials, such as two-dimensional electron gases (2DEGs), graphene, and two-dimensional transition metal dichalcogenides (2D-TMDs), gain so much attention in multidisciplinary field across Physics, Chemistry, Engineering, and Biology (Xia et al., 2014; Leroux et al., 2015). These materials have been extensively studied in a wide range of research from fundamental sciences to applications (Kaul, 2013; Wang et al., 2014). Two-dimensional property of the materials, which exhibits extraordinary electronic and optical properties, can be formed in at least two cases. Firstly, layers of solids are thinned down to the optimum thickness with the form of single or few sheets. This is known for graphene formed on graphite (Falkovsky, 2008; Apell et al., 2012). Secondly, when the spatial expansion of materials becomes smaller than the wavelength of the conduction electrons. Therefore, electrons will be confined at the surfaces of material resulting to the quantization of energy and momentum. The quantized energy dominated by

quantum size effect can generate two-dimensional nature in the materials which is known as 2DEGs. The scientific backgrounds including crystal structures, physical and electronic properties of the materials which exhibit two-dimensional electronic structures will be described.

4.1 Two-dimensional electron gases (2DEGs)

The basic idea of 2DEGs can be derived by a simple particle in a 1D box. Assuming electrons are confined in the box of width L, the potential describing the box can be given by

$$\mathbf{V}_x = 0, \quad 0 < x < L$$
$$\mathbf{V}_x = \infty, \quad otherwise \tag{4.1}$$

Solving the Schrödinger equation of this quantum well (Eq. 4.1) gives the energy eigenvalues of

$$E_{\mathbf{k}} = \frac{\hbar^2 \mathbf{k}^2}{2m} \tag{4.2}$$

where m is the mass of the particle, $\mathbf{k} = \frac{2\pi}{L}$, n = quantized number. Generally, electrons can be confined in different spatial dimension depending on the system, for example, one dimension in quantum well, two dimensions in quantum wire, and three dimensions in quantum dot. In 2DEGs, electrons are allowed to move freely on the plane (x-y direction) but confined along one direction perpendicular to the surface (z-direction). This behaviour gives rise to the observation of quantum Hall effect which makes 2DEGs very interesting (Von Klitzing, 1985). 2DEG property can be practically measured by Hall effect measurement or surface sensitive technique such as ARPES.

Most 2DEGs, which offer a system of extremely high electron mobilities (reported up to 32×10^6 cm^2/V.s (Kumar et al., 2010)) especially at low temperature, are found in semiconductor. Then, the engineering of 2DEGs is very promising to be used in high mobility transistor. In general, 2DEGs can be formed in many systems. In this part, however, I will describe only the creation of 2DEGs related to my study. Firstly, I will give an example of 2DEGs formed at the interface of two transition metal oxide (TMO) semiconductors. A high mobility electron gas can be created at the interfaces of LaAlO$_3$/SrTiO$_3$. Both LaAlO$_3$ and SrTiO$_3$ are wide band gap semiconductors (E$_g \approx 5.6$ eV and 3.2 eV for LaAlO$_3$ and SrTiO$_3$, respectively). They also have lattices which reasonably well matched with one another (3.789 $\mathring{A}$ and 3.905 $\mathring{A}$, respectively) (Ohtomo and Hwang, 2004). LaAlO$_3$/SrTiO$_3$ interfaces are usually grown in ultrahigh vacuum with pulsed laser deposition method, i.e., evaporating LaAlO$_3$ on SrTiO$_3$ (001) single crystal substrates.

Figure 4.1 (c) shows the schematic of the resulting (LaAlO$_3$)$^+$/(TiO$_2$)^0 interface, the composition and the ionic charge state of each layer. The carrier concentration could be controlled by growing an interface at different oxygen partial pressure. The results show that electron carriers can change the conductive property from strongly localized (insulator) at low carrier concentration to metallic at higher carrier concentration. Figure 4.1 (a) and (b) show the temperature dependence of the hall electron mobility ($\mu_H(T)$) measured at the LaAlO$_3$/SrTiO$_3$ interface. Interestingly, the Hall mobility was measured up to 10,000 cm^2 V^{-1}S^{-1} at low temperature.

Electron transport at the LaAlO$_3$/SrTiO$_3$ interface has also been reported for heterostructure grown on silicon. The room temperature mobility and carrier concentration of LaAlO$_3$/SrTiO$_3$ heterointerfaces can be measured to be around 350 cm^2/V.s and 8×10^{14} cm^{-2}, respectively, which are comparable with a SrTiO$_3$
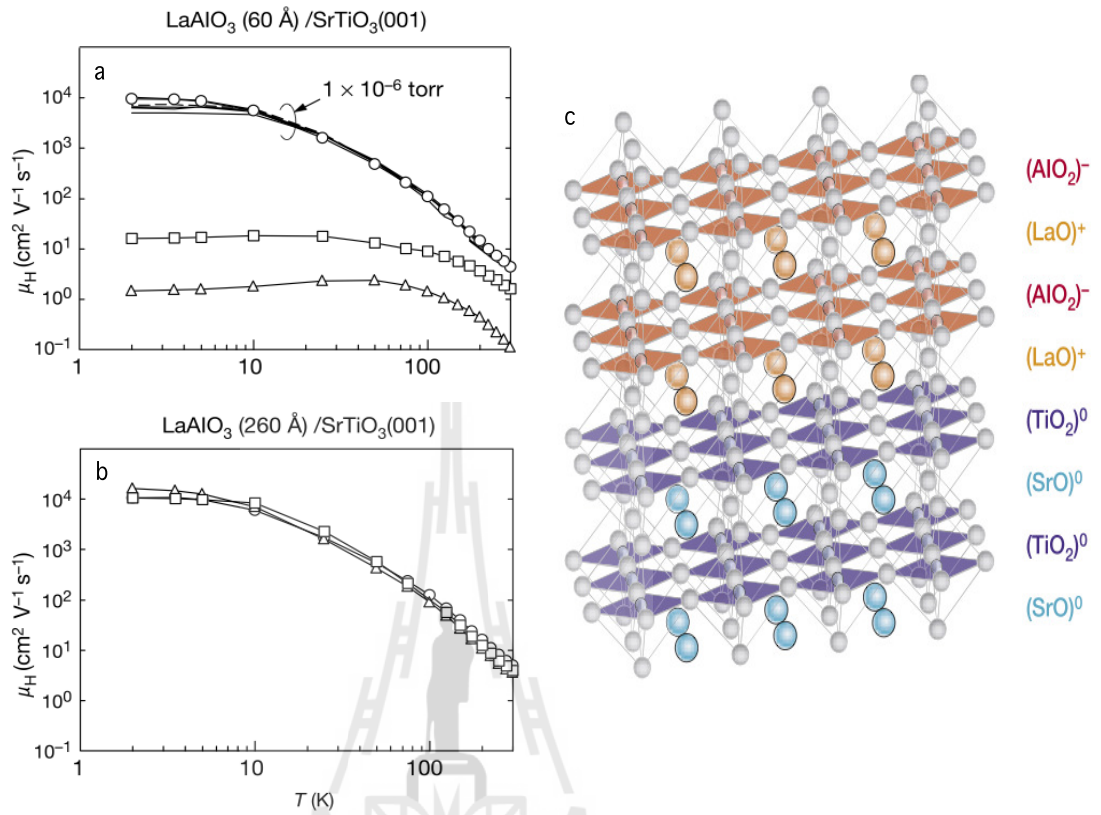
Figure 4.1 a) and b) Temperature dependence of $\mu_H(T)$ for the interface between a layer of 60 and 260 $\mathring{A}$ thick of LaAlO$_3$ on SrTiO$_3$ substrate, respectively. c) Schematic of the resulting of $(LaAlO_3)^+/(TiO_2)^0$ interface (Ohtomo and Hwang, 2004).

bulk single crystal (Park et al., 2010). In particular, the LaAlO$_3$/SrTiO$_3$ thin film heterostructure was grown on various single crystal substrates and measured their carrier concentration. In their research, they found that the strain effect of different substrates plays an important role for the carrier concentration at the interfaces (Bark et al., 2011). After this finding, Meevasana et al. have reported the creation and control of 2DEGs at the bare SrTiO$_3$ surfaces (Meevasana et al., 2011). Their research opens the study of the two-dimensional electronic structure

on bulk material which will be discussed below.

4.1.1 Creation and the study of spin-orbital texture of the SrTiO$_3$ two-dimensional electron gas

SrTiO$_3$ is one of the most interesting many-body interaction TMOs since it exhibits a wide range of functional properties such as multiferroicity, superconductivity, and optoelectronics (Bednorz and Muller, 1988; Von Helmolt et al., 1993; Kimura et al., 2003). The high electron mobility has been investigated in SrTiO$_3$ based-interface but the microscopic origin remains unexplored. Meevasana et al., utilized ARPES to study the 2DEG property on SrTiO$_3$. The clean surface of SrTiO$_3$ is insulating which is expected to have no spectral weight at Fermi energy. Interestingly, as shown in figure 4.2, they can probe the 2DEG density (at the Fermi level) which have been developed as a function of UV irradiation doses. The corresponding 2DEG charge densities as a function of dosing have been shown in figure 4.2 (f). This means some surface-localized state occurring after light doses. These 2DEG states could be the effect of band bending driven by electron accumulation at the surfaces (Meevasana et al., 2011). The two-dimensional state can be proven by measuring the state at Fermi level with various photon energies as shown in figure 4.3.

There are many experimental observations of 2DEG at the surfaces of SrTiO$_3$ but the theoretical understanding is remained elusive. Here, the study of quasiparticle dynamics and spin-orbital texture of SrTiO$_3$ two-dimensional electron gas is purposed with me as a coauthor contributed mainly in the experimental part. (King et al., 2014) By exploiting ARPES measurement and self-energy calculation, we uncover how quantum confinement and inversion symmetry breaking collectively tune the delicate interplay of charge, spin, orbital, and lattice de-

grees of freedom in this system. We demonstrate how they lead to pronounced orbital ordering, mediate an orbitally-enhanced Rashba splitting with complex subband-dependent spin textures and markedly change the character of electron-phonon coupling, co-operatively shaping the low-energy electronic structure of the 2DEG. Our results allow for a unified understanding of spectroscopic and transport measurements across different classes of $SrTiO_3$-based 2DEGs, and yield new microscopic insights on their functional properties (figure 4.4).
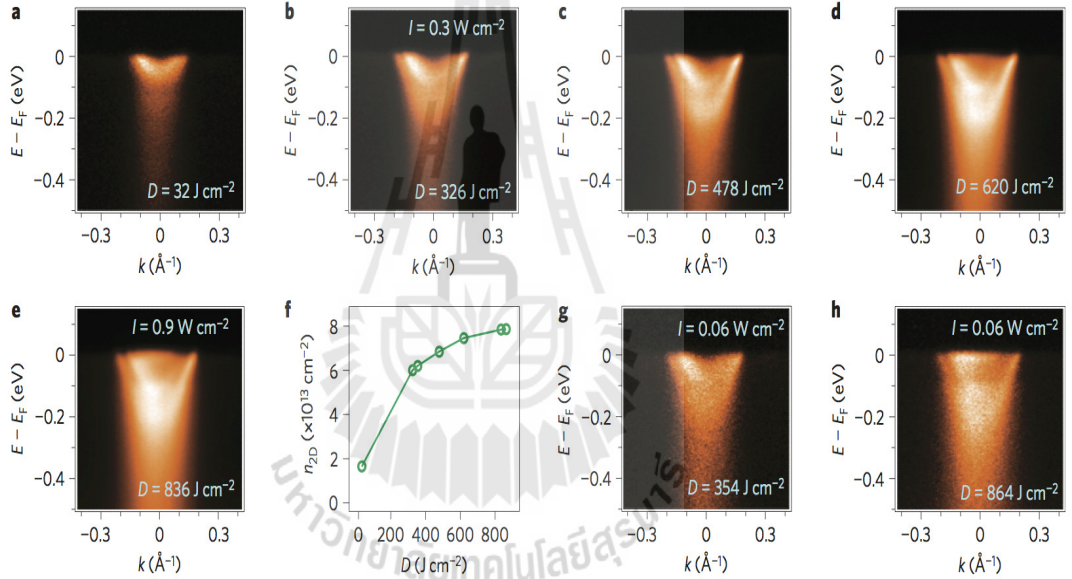
Figure 4.2 Variation of 2DEG charge density with exposure to different UV irradiation doses. a)-e), g), and h) The conduction band states probed by ARPES with different light irradiation doses. f) The number of electrons in a function of irradiation doses (Meevasana et al., 2011).
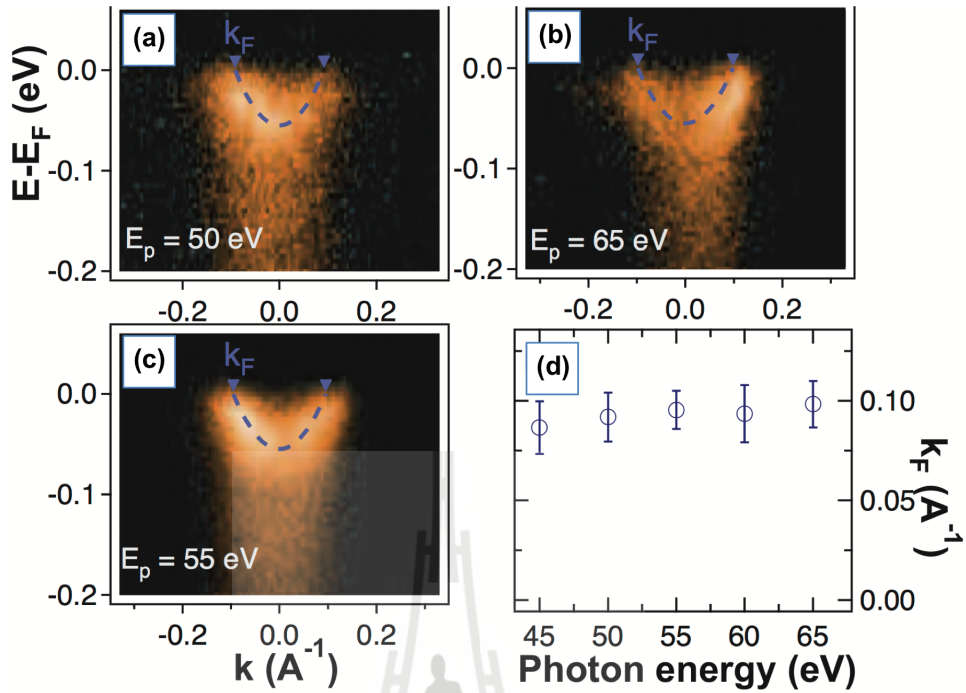
Figure 4.3 Photon energy dependence of ARPES data indicating negligible k_z dispersion. a)-c) show ARPES data measured with low photon flux at various photon energies. d) summarizes the Fermi momenta k_F extracted from a)- c). The range of photon energies corresponds to estimated k_z values from 2.6 - 3.8π/a. (Meevasana et al., 2011)

4.1.2 Subband structure of a two-dimensional electron gas formed at the polar surface of $KTaO_3$

KTaO$_3$ is one of the 5d TMOs which is particularly interesting because of their large spin-orbit interactions predicted by the unconventional ground state (Pesin and Balents, 2010). KTaO$_3$ offers the potential to incorporate new schemes of semiconductor electronics and novel 2D electron systems which is an essential toward the practical application. I was a coauthor contributed in the ARPES measurement of this work which presented the study of 2DEG state at
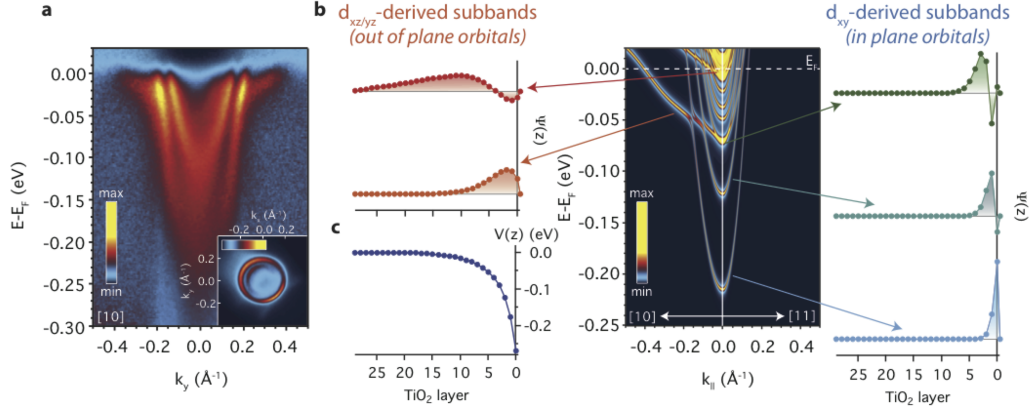
Figure 4.4 a) The 2DEG state of SrTiO$_3$ measured along the [10] direction, revealing multi-orbital subbing structure. b) The d orbital derived-subbands as a function of TiO$_2$ layer. c) Band bending near the surface. (King et al., 2014)

the surface of insulating KTaO$_3$ single crystal by ARPES. This work has been published by (King et al., (2012)). Figure 4.4 (a) and (b) show our observed 2DEG state with light effective masses at the highest binding energy (band 1 and 2) of about 0.3 m$_e$ which is smaller than the one observed in SrTiO$_3$ (Meevasana et al., (2011). This suggests that KTaO$_3$ could develop high mobility oxide electronics rather than SrTiO$_3$. We can also see the different bands using different light polarization as illustrated in the bottom right of these figures. The number of electrons can be extracted to be around 2×10^{14} cm^{-2} in the equivalent Fermi map in both polarizations (figure 4.6 (c) and (d)). Figure 4.5 (a) shows the increasing of Fermi wave vectors of both KTaO$_3$ and SrTiO$_3$. The 2DEG states in KTaO$_3$ exists right from the initial state, which is different from the observation in SrTiO$_3$. Fig 4.6 (c) illustrates the non-polar and polar nature of SrTiO$_3$ and KTaO$_3$, respectively. Each planes of SrTiO$_3$ are non-polar but KTaO$_3$ planes consists of polar plane of TaO$_2^+$ and KO$^-$. Hence, after KTaO$_3$ samples were cleaved, about half of KO$^-$ layer on TaO$_2^+$ surface was left. Holes and electrons are allowed to form at the
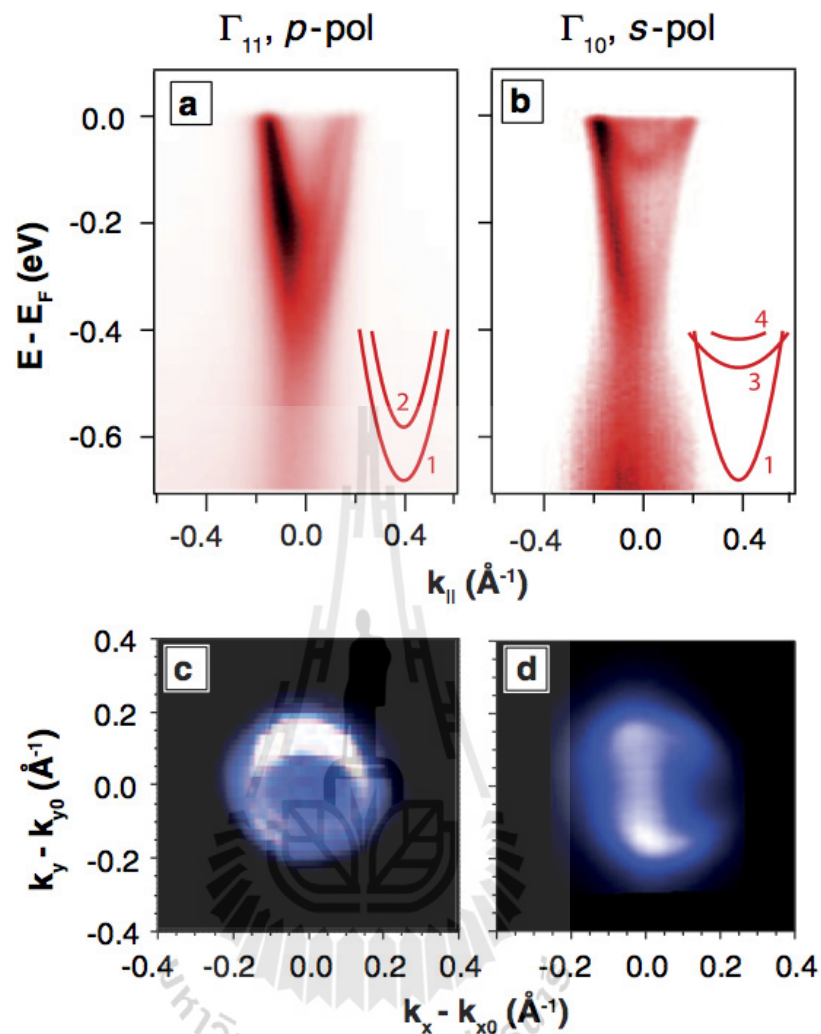
Figure 4.5 The electronic structure of KTaO$_3$. a) and b) Saturated 2DEG state along Γ-X direction. c) and d) Equivalent occupied Fermi surface of a) and b), respectively (King et al., 2012).

surfaces and initial 2DEG state can be created much more rapidly on KTaO$_3$. Figure 4.6 (b) shows the O$_{2p}$ valence band shifting to higher binding energy. This suggests that the density of the 2DEG in KTaO$_3$ and SrTiO$_3$ may be driven by controlling the positive surface charges caused by UV light irradiation.
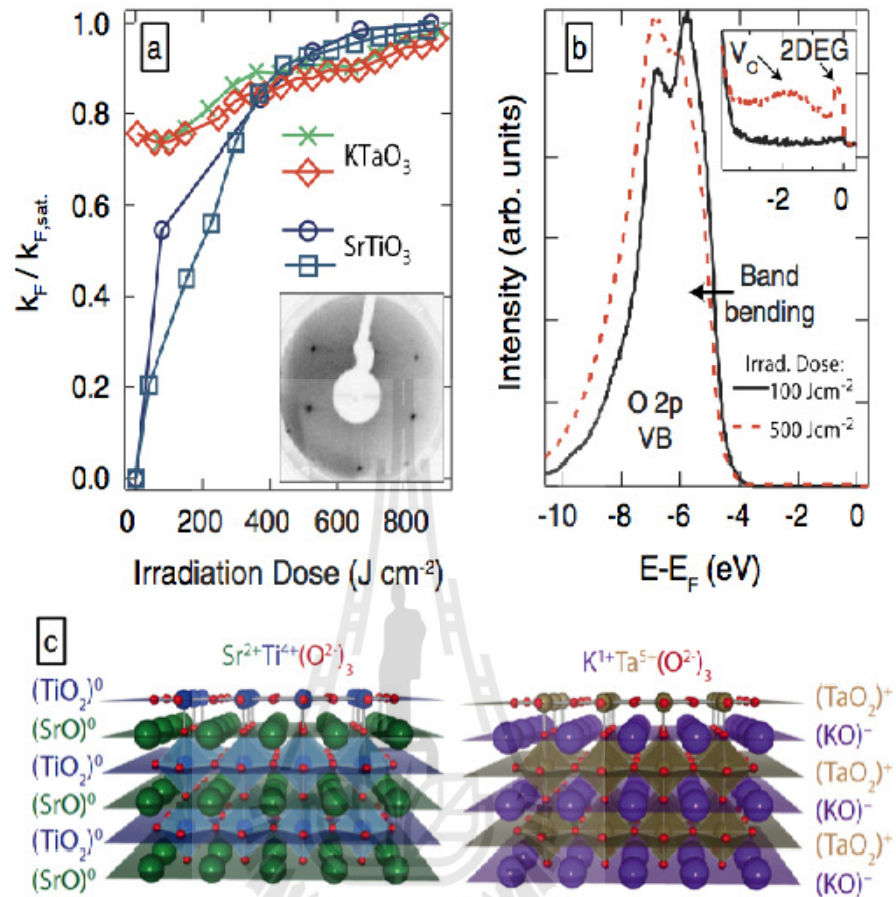
Figure 4.6 a) Light irradiation dose dependence on $SrTiO_3$ and $KTaO_3$. b) Band bending resulted from oxygen vacancy. c) Diagram of non-polar and polar surface of $SrTiO_3$ and $KTaO_3$, respectively (King et al., 2012).

4.1.3 Application of 2DEG state

The 2DEG state gained from ARPES can be applied to other macroscopic system. In this section, I will give two published results which I am one of the coauthors contributed in the experimental part. The anomalous change in dielectric constant of $CaCu_3Ti_4O_{12}$ and the resistivity change in $SrTiO_3$ upon light

irradiation have been discussed which is the result from 2DEG created at the surfaces caused by oxygen vacancies. The sample preparation, measurement and discussion are available in appendix B.

CHAPTER V

TWO-DIMENSIONAL GRAPHENE AND BEYOND

5.1 Graphene

Graphene is the first example of stable 2D crystal. This breaks the role of many scientific researches for both fundamental studies and applications (Novoselov et al., 2005b). Graphene is a single layer of carbon atoms arranged in a honey comb structure. It exhibits remarkable crystalline qualities with extremely high carrier mobilities of 15,000 cm^2/V.s (Geim and Novoselov, 2007), heat conductivity, and strength (100 times stronger than steel). Besides being as a very promising material in novel electronics, it has also been studied in spintronic research by applying gate voltage to its spin (Zhang, 2014). Graphene is an ideal 2D crystal whose electrons are bounded in a single layer. This is in contrast with the previously mentioned of 2DEGs. Interestingly, graphene is a zero band gap semiconductor with a linear dispersion near the Fermi energy. The charge carriers in graphene act as 2D massless relativistic Dirac particles (Novoselov et al., 2005a), The quantum Hall effect was also observed in room temperature (Novoselov et al., 2007). By neglecting many-body effect, the electronic structure of graphene can be accurately derived in term of Dirac equation for massless particles

$$v_F \vec{\sigma} \cdot \nabla \psi(r) = E \psi(r) \tag{5.1}$$

where $v_F = 10^6$ m/s is the Fermi velocity. $\vec{\sigma} = (\sigma_\uparrow, \sigma_\downarrow)$ are the Pauli matrices called "Pseudospin" which can be clearly observed in relativistic analogue of the integer quantum Hall effect. This hamiltonian leads to the linear dispersion relation between energy and momentum as

$$E = \hbar v_F \sqrt{k_x^2 + k_y^2} \tag{5.2}$$

Although an unusual linear spectrum in graphene is important, this is not the main feature describing the quantum transport of graphene. Exploting quantum electrodynamics (QED), the conical spectrum of graphene can be described as a result of intersection between energy bands originating from sublattice pseudospin $A(\uparrow)$ and $B(\downarrow)$ of two pi-bands. The electron and hole with opposite energy $\pm E$ propagate in the opposite direction yielding accumulated pseudospin pointing to the same direction. This allows one to introduce chirality which is normally a projection of pseudospin on the direction of motion. Hence, the electron has to change the sign when it moves along the pi-closed contour.

The main concerning topic of graphene is the mass production process since it is the excellent candidate for the new generation application. Graphene can be produced by several methods in the present. For example, by mechanical exfoliation technique which is the cleavage of graphite to be the monolayer thickness of graphene. This fabrication has still not produced graphene in a large scale yet but provides the fundamental study for a lab scale. Another method is the reduction of graphene oxide; putting a mild ultrasonic treatment of graphite oxide in water to produce graphene oxide sheet which can easily depose to the appropriate substances. This technique provides the low cost and mass production, however, it has less efficiency. The most promising method used to produce a large scale is epitaxial growth; growing the monolayer of graphene on the cat-

alytic substrates by either chemical vapor deposition (CVD) or molecular beam epitaxy (MBE). Graphene grown by this method is recently achieved in enormous substrates such as Ni, Ir, and SiC (Varykhalov et al., 2008; Riedl et al., 2009). Besides, the interesting method related to my study is the element intercalated in graphene, for example, graphene can be obtained by lifting a few layers out of the bulk substrate by hydrogen intercalation. Previous report shows the creation of quasi-freestanding monolayer of graphene on the SiC substrate (Riedl et al., 2009). This method is very promising but it requires new insight gained from the spectroscopic study. Alternatively, a zero band gap behaviour in graphene is inconvenient in the electronics era (semiconductor technologies). Currently, other materials especially in semiconducting TMDs, which exhibit the nature of layered material and optical band gap, gain much attention beyond graphene. Here, the introduction of 2D TMDs especially MoS_2, which is my main study material, will be discussed in the section below.

5.2 Transition metal dichalcogenides

Transition metal dichalcogenides (TMDs) are now the most studied layered materials which gain a lot of sciencitfic attention in the present. TMDs adopt the chemical formula of MX_2, where M = transition metal (Mo, W), and X = chalcogen (S, Se) (Mattheiss, 1973). Each layer of TMDs has thickness of around 6 - 7 $\mathring{A}$ which is similar to graphene. Each in-layer of these materials is bonded with strong ionic bonding while each neighbouring planes are interacted with weak van der Waals (vdW) force with few orders of magnitude weaker than in-plane interaction. In fact, TMD structures fall into two distinct classes: non-layered and layered TMDs. The non-layered TMDs are mostly formed through the combination of group VII and beyond. They typically consist of four types: pyrites, marcasite,

IrSe$_2$, and PdS$_2$. The vdW gap in non-layered TMDs such as NiS$_2$ and CoTe$_2$ has been eliminated leading to the strong X-X pairing on its structure. However, in this study, we are intensely interested in the layered TMDs. Layered TMDs arise from the stacking of hexagonal packed plane with three or six chalcogens around center metal atoms in trigonal prismatic. The weak vdW force between each layer of TMDs leads to marked cleavage property perpendicular in out-of-plane axis.

There are over eighty layered TMD compounds which can exhibit a wide spectrum ranging from insulating to superconducting. For example, HfS$_2$ is a good insulator; HfSe$_2$ and MoS$_2$ exhibit semiconducting property; WTe$_2$ is a semimetal; PdTe$_2$ is metallic; all of Nb-base TMDs present the superconducting (Guo et al., 2014; Wilson and Yoffe, 1969; Wang et al., 2012; Jiao et al., 2014). The bulk TMDs are found in typical structures such as trigonal (1T), hexagonal (2H), and rhombohedral (3R) or other structures (4Ha, 6R) (figure 5.1). The integer indicates the number of X-M-X sandwiches per unitcell along the hexagonal axis. However, in the normal condition, the overlap between metal and chalcogen wave function is optimized in a trigonal prismatic coordination leading to the typical forms of 1T and 2H. 2H structure is typically referred to MoS$_2$ which the anion hexagonal net are A-A stacked. In contrast, 1T structure is called CdI$_2$ with A-B anion stacked as shown in figure 5.2.

In particular, Mo- and W-based TMDs are semiconductors with controllable band gap varied from 1.5 - 2.1 eV (Frey et al., 1998; Kuc et al., 2011) which are the most heavily studied materials beyond graphene. Two-dimensional semiconductors fabricated from ultrathin TMDs hold enormous potential for novel electronic device applications, for example, a strong emission in a visible frequency range is promising in optoelectronics (Wilson and Yoffe, 1969). In contrast with other strong bonding system, the chemical and physical properties in layered

TMDs have been considered as nearly two-dimensional system which exhibit an anisotropic property. For example, the out-of-plane conductivity is less than in-plane conductivity in the order of 10^2. Moreover, the carriers are likely to move by the hopping mechanism rather than the former direction between layers.

As mentioned in the previous section, many scientific researches have attempted to open the gap of graphene (enables electronic switching) but got a little successful (Zhou et al., 2007). So, this provides the optical band gap 2D TMDs to play the dominant roles beyond graphene. Semiconducting TMDs are very promising for existing devices. The optical, physical and electronic properties of TMD monolayers will be presented in the view of our interested TMD compounds. MoS_2 as well as other TMDs such as $HfSe_2$, WSe_2, and $PdTe_2$ are the main materials for the discussion.

The weak vdW force between TMD layers can be achieved by many methods such as mechanical exfoliated or Scotch tape method from few layer of TMDs (Coleman et al., 2011). Molecular beam epitaxy method (MBE) is a good choice for creating freestanding TMD monolayer on different substrates (Zhang et al., 2014c). The quantum confinement and structural symmetry derived from the number of layers held different electrical properties in semiconducting TMDs. Interestingly, several TMDs such as MoS_2, $MoSe_2$, and WSe_2 have been predicted to have the striking crossover from indirect to direct band gap as they are thinned down to a single monolayer (Ellis et al., 2011). The direct observation of this exceptional transition have been observed experimentally. For example, the transition from indirect to direct band gap on MoS_2 monolayer has been recently observed by photoluminescence (Mak et al., 2010). Direct observation of epitaxial grown $MoSe_2$ monolayer has been measured by ARPES (Zhang et al., 2014c).

TMD monolayers hold very promising properties which may be used in
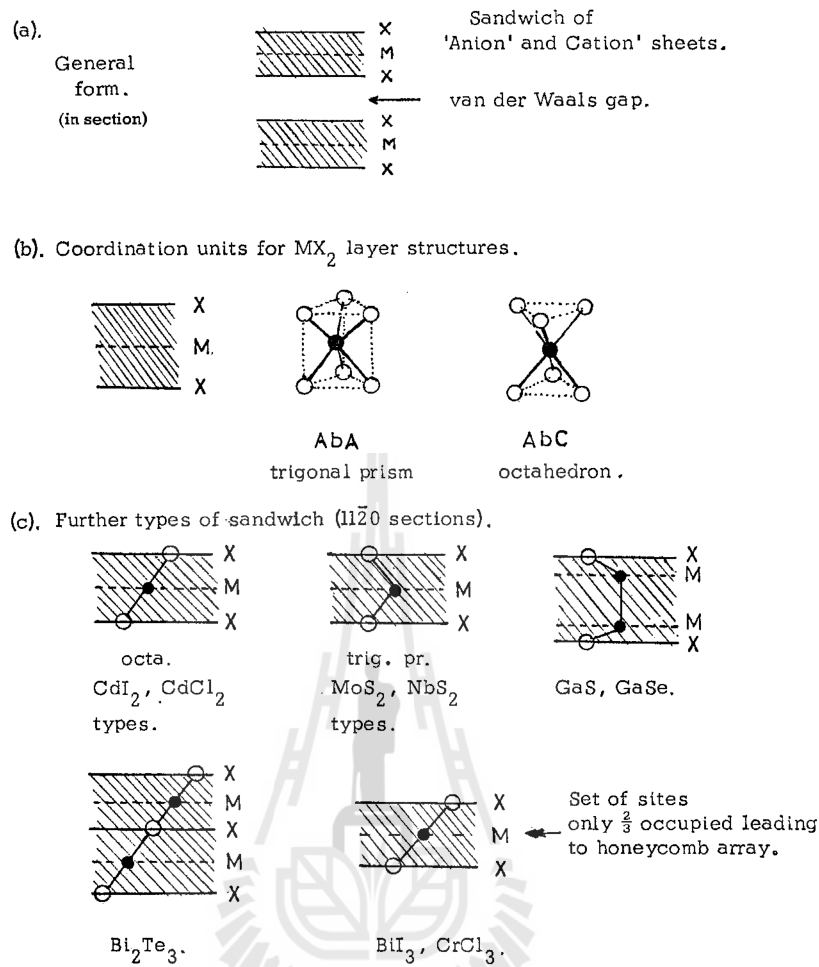
Figure 5.1 Schematic illustration of layered compound with the basic forms (Wilson and Yoffe, 1969)

wide range of applications such as high speed transistor, high efficiency optics as emitters, detectors, and thickness modulated phototransistor (Mak et al., 2010; Splendiani et al., 2010). The exciton, which is the electrically neutral quasiparticle incurred from electron-hole paired when excited electron from photon leaves behind electron hole, is suggested to be a crucial role in the optical transition of ultrathin TMD samples (Mak et al., 2010). Exciton can transport energy without electric charge resulting of repulsive coulomb force in the material (Liang, 1970). The shift of exciton emission peak depends on the strain and surrounding elec-
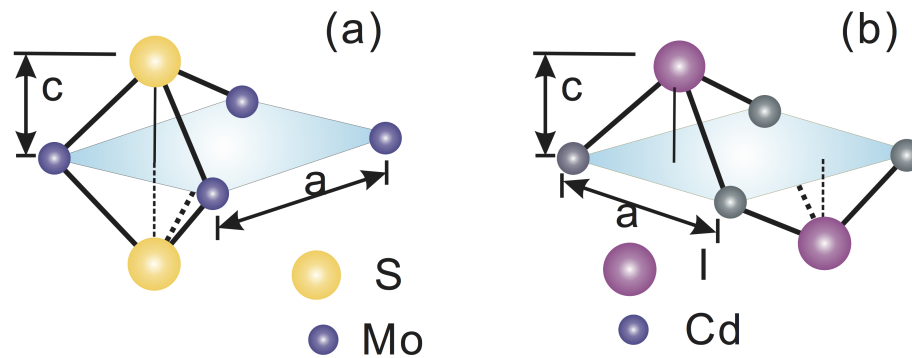
Figure 5.2 Schematic illustration of MoS$_2$- and CdI$_2$- types structure (Zhang et al., 2014a)

tric environment. For example, in MoS$_2$, the two distinct peaks assigned to A and B excitons have been predicted to be as high as 0.5 - 0.9 eV for monolayer and 0.4 eV for bilayer (Mak et al., 2010). Furthermore, TMD monolayers have inversion symmetry breaking which allows the new degree of freedom of charge carriers called k-valley index via applying circular-polarized light. Thus, this opens the new research field in Physics called "valleytronics". As shown in figure 5.3 (a) - (c), the honey comb structure with M and X$_2$ atoms in different corners in TMDs can lift the degeneracy in $\bar{K}$ and $\bar{K}'$ point allowing the charge of opposite spin confined in a particular valley which is in contrast to the states derived in bilayer (Mak et al., 2012). Recently, the discovery of the selective valley population with circular-polarized light in monolayer of MoS$_2$ and WSe$_2$ (Cao et al., 2012; Srivastava et al., 2015) and optical control of valley polarization have been observed in MoS$_2$ (Zeng et al., 2012). Analogues of MoS$_2$, such as a single layer WSe$_2$, have been measured with large spin-orbit splitting of about 500 meV at valence band maximum (Riley et al., 2014). Moreover, the inversion asymmetry in TMD monolayers can induce strong spin-orbit splitting in TMDs in the order of hundreds meV at the valence band and incur the discovery of a single Topolog-

ical Dirac Fermion. This allows us to control the electron spin of TMDs via light exposing applied in spintronics.
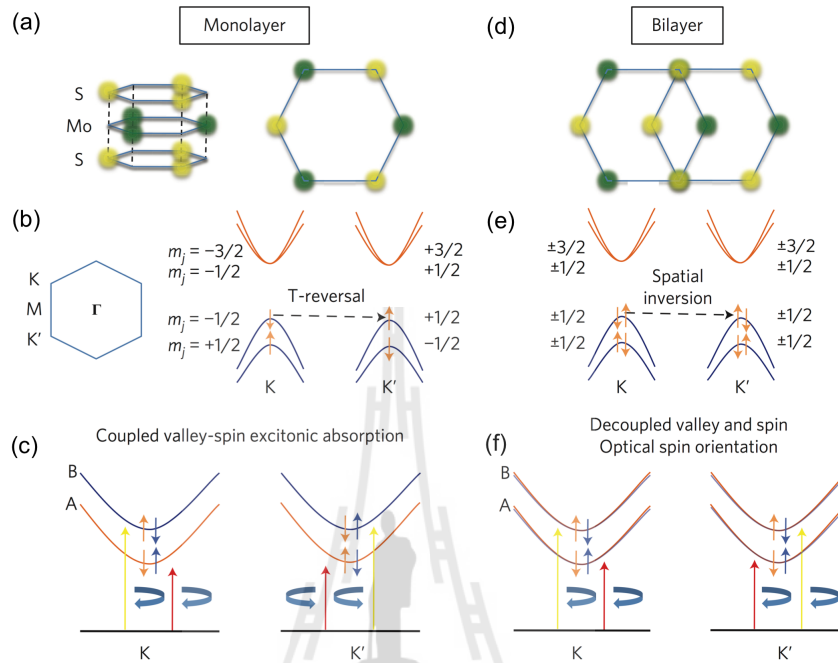
Figure 5.3 Atomic structure and electronic structure at the $\bar{K}$ and $\bar{K}'$ valleys of monolayer a)-c) and bilayer d)-f) MoS_2 (Mak et al., 2012).

5.2.1 Molybdenum disuldfide

MoS_2 gains significant interest among layered TMDs because of its desirable electronic and optical properties. The bulk MoS_2 is well-known for its use as transistor, dry lubricant, and catalyst for the last 40 years (Frindt and Yoffe, 1963; Wilson and Yoffe, 1969). MoS_2 is a silvery black solid which is abundance available in nature known as Molybdenite. Figure 5.4 shows the structure of MoS_2 which is a stack of covalent planes of S-Mo-S atoms closely packed in a hexagonal coordinate (Wilson and Yoffe, 1969). The adjacent planes are held together by vdW interactions which lead to a great possibility of mechanical exfoliation from

bulk crystalline MoS_2 (Novoselov et al., 2005b).

MoS_2 can be formed in three poly types: 1T, 2H, and 3R indicating tetragonal, hexagonal, and rhombohedral unit cell. In this thesis, $2H$-MoS_2 is studied as it is one of the most widely studied form of MoS_2. Bulk MoS_2 has an indirect band gap of around 1.2 eV (Gmelin, 1995). Its band gap is increased when the thickness is thinned down to be lower than 100 nm due to the quantum confinement. The results of quantum confinement and the inversion asymmetry drive a dramatic reconstruction due to the crossover from and indirect to direct band gap in MoS_2 electronic structure (Mak et al., 2010).

MoS_2 single or few layers have been successfully prepared by several techniques such as lithium intercalation, liquid exfoliation, and the cleaving process (Chen et al., 2012; Coleman et al., 2011; Novoselov et al., 2005b). Few layered MoS_2 possesses very good physical properties as it exhibits the interesting features in the absence of dangling bonds and thermal stability up to 1,100 °C. It shows an excellent chemical stability, good mechanical flexibility, and durability. The production cost is low when compared to graphene. The unique optical properties found in MoS_2, such as fast photoresponse and very high light absorption (Xiao et al., 2012), lead to the intensively study in optoelectronic applications, for example, thickness-modulated MoS_2 used as nanosheet phototransistor (Lee et al., 2012), the study of flexible ultrathin photovoltaic with high power densities in MoS_2 (Wi et al., 2014), the enhancement of photocatalyst (Zong et al., 2008), attractive channel and barrier layer for atomic scale transistors (Fontana et al., 2013).

Interestingly, the single layer MoS_2 is a 1.8 eV direct band gap semiconductor which can be obtained by both experiment and calculation (Mak et al., 2010; Ellis et al., 2011). This system holds the strongly entangling of the spin and valley

degrees of freedom which its valley polarization can be controlled optically. From these statements, MoS_2 single layer could be the good candidate for the new generation of tunable valleytronic devices (Zeng et al., 2012; Mak et al., 2012). The superconductivity has been observed in the MoS_2 based-intercalation system, for example, $T_c \approx 6.9$ K have been measured in $Rb_{0.3}MoS_2$ (Woolam and Somoano, 1976). The electric double layer transistor (EDLT), a field effect transistor with a gate dielectric made of a liquid electrolyte, gains much attention to enhance the superconductivity in MoS_2 reported up to 9.4 K (Ye et al., 2012). The electron mobility in MoS_2 can be reached up to 200 $cm^2/$ V.s (Radisavljevic et al., 2011) which is very small compared to graphene (200,000 $cm^2/$ V.s). However, switching circuit in graphene is very difficult and holds lots of power dissipation since graphene does not have band gap. Hence, MoS_2 monolayer is a good candidate for nano transistors because it has a very good ON/OFF current ratio ($>10^7$) and ultralow standby power dissipation compared with graphene (Radisavljevic et al., 2011).
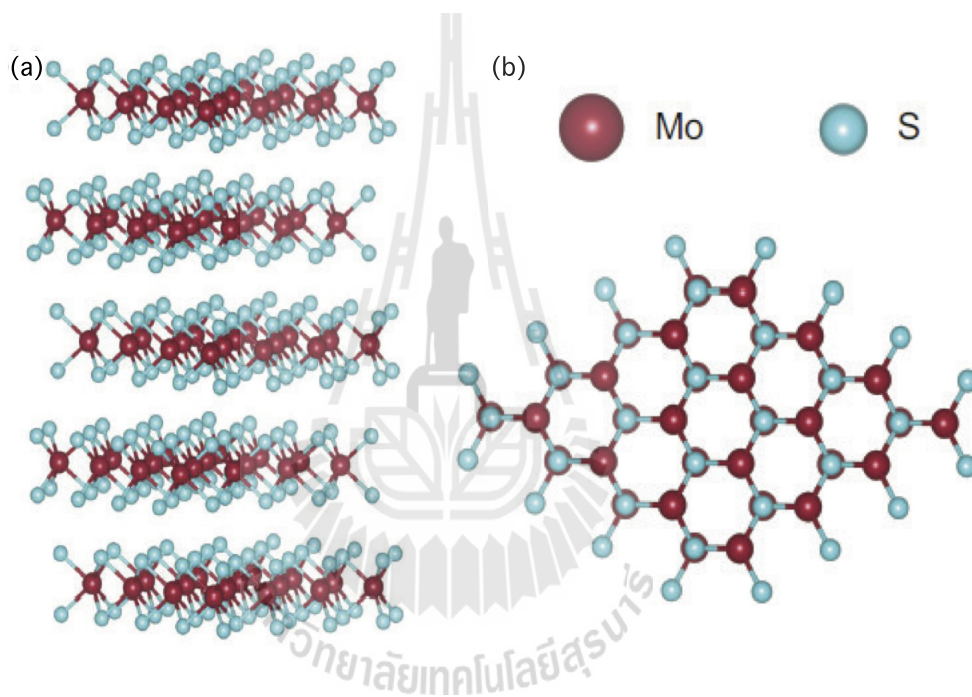
Figure 5.4 MoS$_2$ honeycomb structure constructed by in-plane covalent bonding and vdW bonding in the interlayered a) side view b) top view.

CHAPTER VI

ELECTRONIC STRUCTURE OF A

QUASI-FREESTANDING MOS$_2$

MONOLAYER

The contents in this chapter are from my published work about the study of electronic structure of a quasi-freestanding (QF) MoS$_2$ (Eknapakul et al., 2014). QF introduces the system which behaves like separated layered of the whole system. In contrast with the monolayer like materials, the method to create QF system is more possible to be the new route to create the large scale of 2D material. In general, we realize that to create the monolayer of any layered materials must be from the growth conditions like molecular beam epitaxy or bulk exfoliation. These techniques always give the small lateral-dimensional specimen as introduced by many researches (Novoselov et al., 2005b; Zhang et al., 2014c). In fact, QF is much more attractive to be the new schemes used in the large scale systems. In this chapter, I will introduce the method to create the QF of MoS$_2$ monolayer by potassium intercalation. The scenario of how to create QF of MoS$_2$ will be performed through our ARPES measurement and DFT calculation. This chapter have been divided into two main parts: experiment and calculation. I made a major contribution in the experimental part of ARPES measurement and data analysis while the calculation part has been done by my coauthor.

The details of ARPES experiment will be discussed herein. Single crystals of 2H-MoS$_2$ were grown using the flux method and cleaved in UHV at a pressure

better than 4×10^{-11} Torr to reveal a pristine (0001) surface (samples come from my colleagues). Their electronic structure was performed using ARPES at beamline 10.0.1 of the Advanced Light Source, USA, using photon energies between 40 and 65 eV and a Scienta R4000 hemispherical electron analyzer. The energy and angular resolutions were set at 10 - 20 meV and 0.3°, respectively, and the sample temperature was maintained at 20 K throughout the experiment. Measurements were performed immediately after the cleave, as well as following the deposition of potassium on to the sample surface from a properly outgassed SAES getter source. Density functional theory (DFT) calculations were performed using the VASP code employing the Perdew, Burke, and Erzenhoff (PBE) (Perdew et al., 1996) exchange-correlation function implemented within the projector augmented wave method (Blöchl, 1994).

6.1 Experimental result

6.1.1 Electronic structure of pristine MoS$_2$

The bulk-MoS$_2$ electronic structure has been calculated to be the indirect band gap semiconductor by both experiment and calculation (Ellis et al., 2011; Mak et al., 2010). As mentioned, MoS2$_2$ has a hexagonal unit cell in the real space which can be converted into the hexagonal Brillouin zone in reciprocal space as described in section 3.3. The high symmetry points in bulk and surface of hexagonal Brillouin zone have been illustrated in figure 6.1 (a).

The important direction is located between two high symmetry points of $\bar{\Gamma} - \bar{K}$ which covered the VBM and CBM in this material. From our ARPES measurement, we first measured the electronic structure along $\bar{\Gamma} - \bar{K}$ direction of the surface Brillouin zone of the pristine cleaved- and dosed- sample. Correction
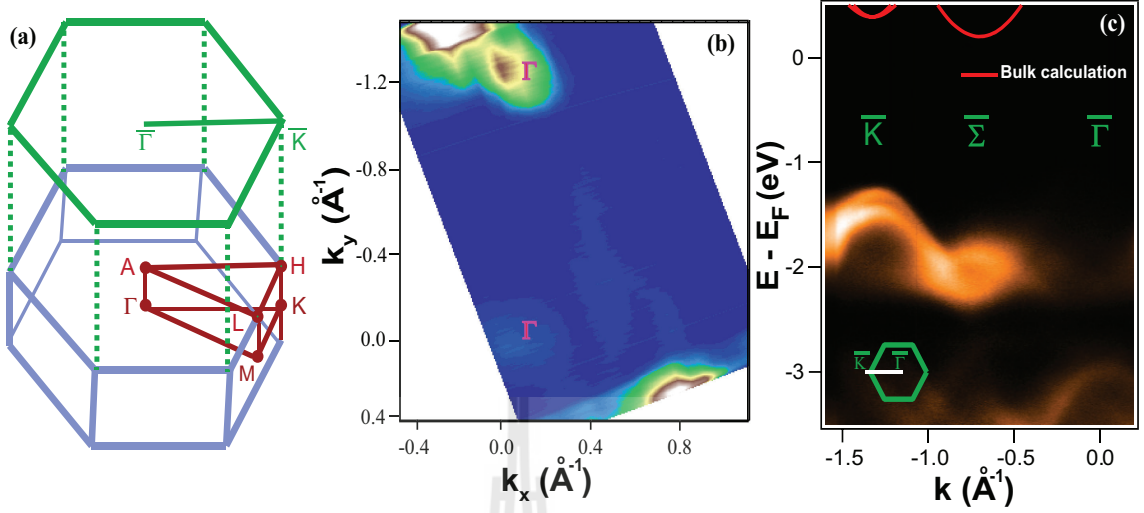
Figure 6.1 The electronic structure of MoS_2 (a) The resulting three-dimensional Brillouin zone and its projection onto the hexagonal surface Brillouin zone. (b) Map at valence band maximum of pristine MoS_2 indicating the right orientation of $\bar{\Gamma}$–$\bar{\Gamma}$. (c) Valence band electronic structure measured along the $\bar{\Gamma}$–$\bar{K}$ direction for the pristine cleaved-surface (adapted from (Eknapakul et al., 2014)).

of orientation along $\bar{\Gamma} - \bar{K}$ have been done using the valence band map which shows the clear VBM at $\bar{\Gamma}$ point (figure 6.1 (b)). We then aligned the sample $30°$ off of the $\bar{\Gamma} - \bar{\Gamma}$ reflecting the $\bar{\Gamma} - \bar{K}$ in the Brillouin zone. For pristine sample, the result shows no spectral weight at the Fermi level as expected for the semiconducting MoS_2 whose chemical potential lies within the band gap (figure 6.1 (c)). By extracting EDC at $\bar{K}$, we observed a clear splitting in the energy of the valence bands at the $\bar{K}$ point of about 170 ± 12 meV, a direct signature of both interlayer interactions and spin-orbit coupling in this compound. This is in quantitative agreement with both quasiparticle self-consistent GW (QSGW) calculations (Cheiwchanchamnangij and Lambrecht, 2012) and the energy splitting

of so-called A and B exciton peaks in optical spectroscopy from bulk MoS$_2$ (Beal and Hughes, 1979).

6.1.2 Electronic structure of potassium evaporated MoS$_2$

After all ARPES information of clean MoS$_2$ were carried out, we then moved the sample to the preparation chamber where the potassium source located. The process of potassium evaporation in UHV has been introduced in section 2.7.5. After potassium has been deposit at the surface of MoS$_2$, the valence bands move to higher binding energy, consistent with electron transfer from potassium to the MoS$_2$, corroborating recent reports from transport of efficient n-type doping by potassium deposition on few layer TMDs (Fang et al., 2013). We find sufficient electron donation to move the Fermi level to the conduction band (figure 6.2 (a)). Interestingly, the Fermi level of doped-MoS$_2$ is located at $\bar{K}$ point which is similar to the previous report of MoS$_2$ monolayer (Ellis et al., 2011). This evidence leads to our conclusion of the QF system which can be pointed out from our XPS and DFT calculation below. By considering the peak fittings extracted from momentum distribution curves (MDCs) to a parabolic effective mass model, we estimate the effective mass at the conduction band pocket to be around 0.67 m_e. This relative high value is larger than predicted by QSGW calculations (Cheiwchanchamnangij and Lambrecht, 2012). This may help to explain the modest mobilities that have been achieved to date in monolayer MoS$_2$ transistors (Zhang et al., 2012).

6.1.3 Fermi surface of potassium evaporated MoS$_2$

The energy contour map can be done by changing the angle (θ) in our experiment. When the θ is changed, the parallel momentum ($k_{//}$) is shifted with a fixed length (explained by equation 2.2). By looking at the constant energy,
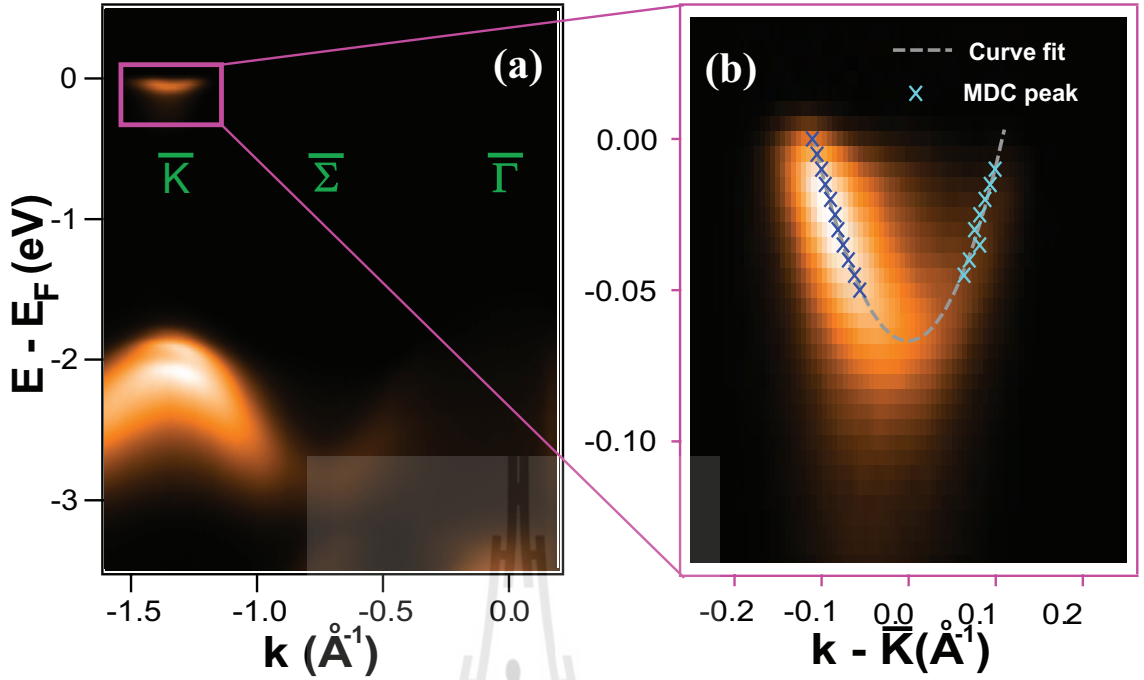
Figure 6.2 (a) Valence band electronic structure measured along the $\bar{\Gamma}$–$\bar{K}$ direction for the potassium dosed-surface. Following potassium dosing, an electron pocket is found at $\bar{K}$, shown magnified in (b) (Eknapakul et al., 2014).

in this case at Fermi level (E - E_F = 0) shown in figure 6.3 (a), the resulting Fermi surface comprises of circular electron pockets at each $\bar{K}$ ($\bar{K}'$) point of the Brillouin zone as well as weak spectral weight associated with secondary band minima approximately mid-way along the $\bar{\Gamma}$–$\bar{K}$ ($\bar{\Gamma}$–$\bar{K}'$) directions (denoted here as $\bar{\Sigma}$). Strikingly, these measurements reveal that the conduction band minima (CBM) are located at the $\bar{K}$ ($\bar{K}'$) points of the Brillouin zone. This is not the case for the bulk electronic structure, where the CBM are known to lie at $\bar{\Sigma}$, that is, away from high symmetry points, (Kuc et al., 2011; Coehoorn et al., 1987; Ellis et al., 2011; Alexiev et al., 2000) but is representative of theoretical expectations for monolayer MoS_2, (Zhu et al., 2011; Ellis et al., 2011) a point we return to below.
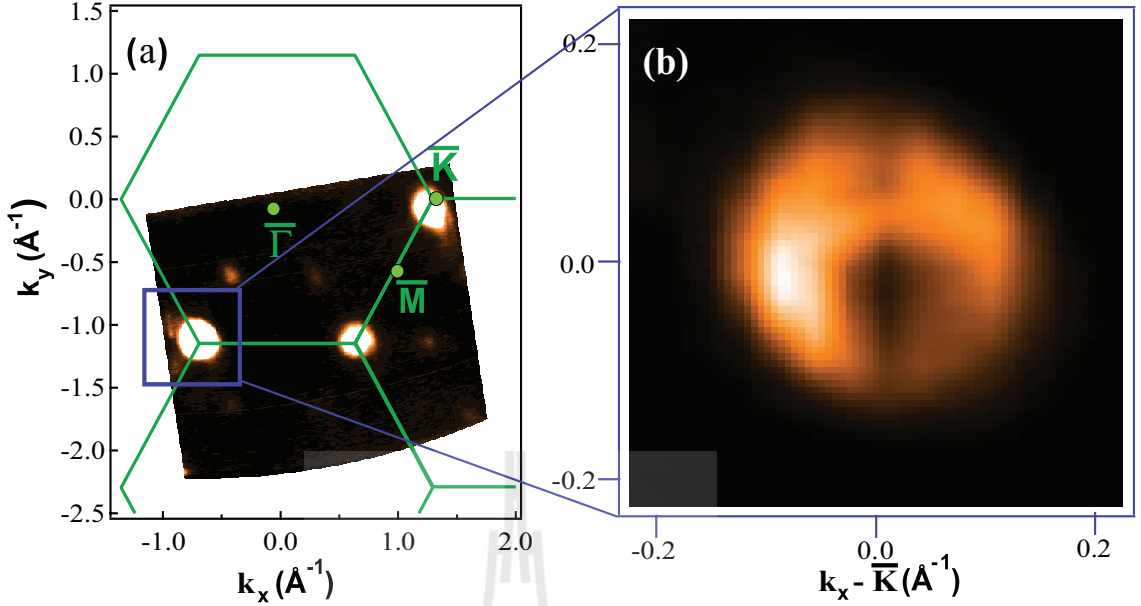
Figure 6.3 (a) The Fermi surface map indicates the equivalent pockets found at each $\bar{K}$ and $\bar{K}'$ point of the surface Brillouin zone, with weak additional spectral weight indicating the presence of a secondary (higher) band minimum along the $\bar{\Gamma}$–$\bar{K}$ line, at the position of the global conduction band minimum in bulk. (b) Magnification of Fermi pocket at $\bar{K}$ indicating the circular shape (Eknapakul et al., 2014).

6.1.4 Photon dependence measurement in our measurement

As describe in section 2.7.1, changing photon energy during ARPES experiment can move the point of measured of k_z along the Brillouin zone (Eq. 2.4). Here, within experimental error, we find that this band does not disperse as we vary the photon energy between 40 - 65 eV (figure 6.4), a change of wavevector along the surface normal (k_z) by approximately 1.5 Brillouin zones. This indicates that the electron pockets formed are two-dimensional nature. Moreover, these measurements do not show occupied states at $\bar{\Sigma}$ for any value of k_z, confirm-
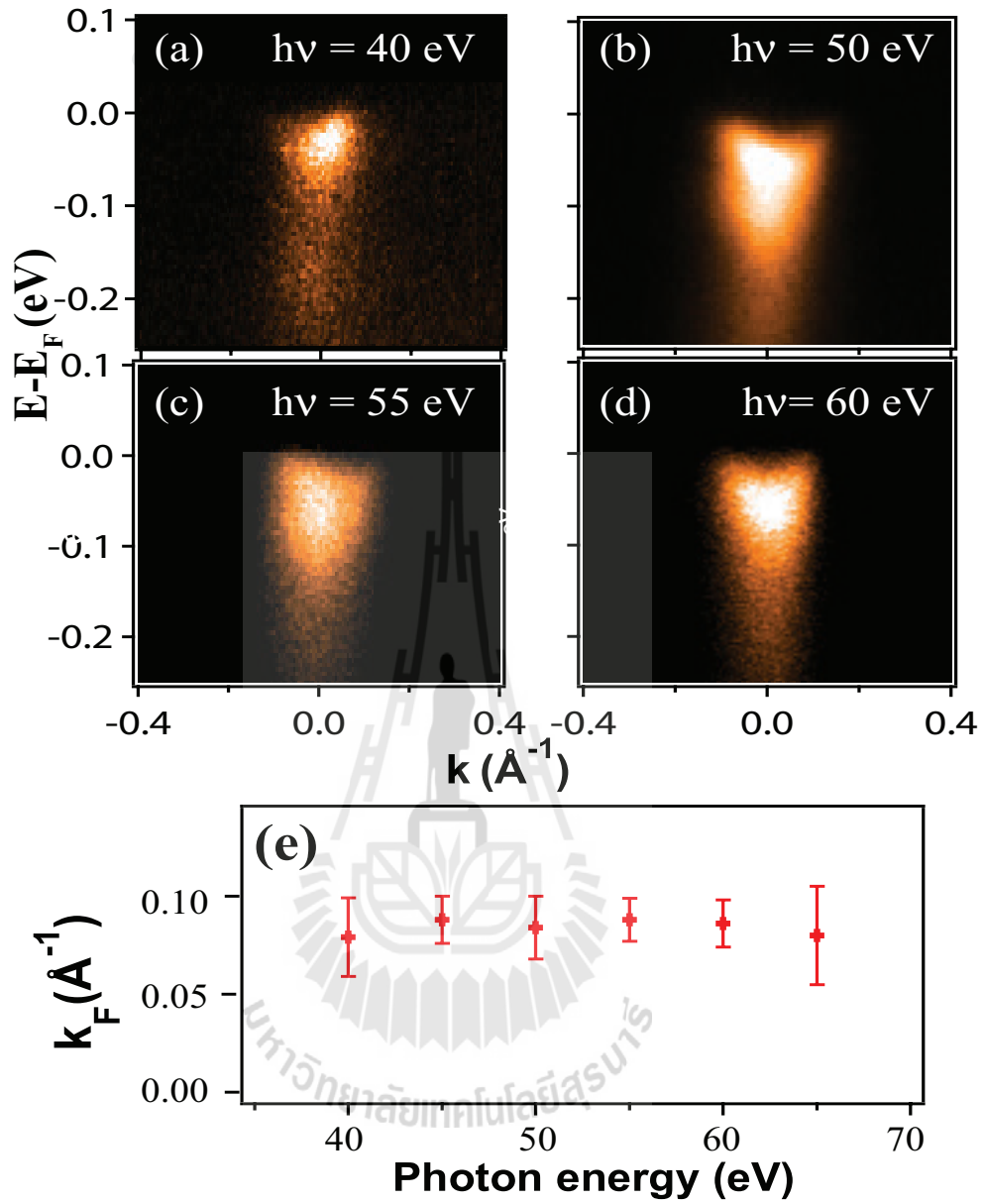
Figure 6.4 (a)-(d) $\bar{K}$-centered Fermi pockets of MoS_2 taken at photon energy of 40, 50, 55, and 60 eV, respectively. (e) Non-dispersive in k_z shown by photon-energy independence of their measured Fermi wavevectors.

ing that the CBM remains at $\bar{K}$ throughout the Brillouin zone, consistent with the expected electronic structure of monolayer MoS_2. We estimate the surface charge density from the Luttinger area of these measured, two-dimensional, Fermi

surface pockets at $\bar{K}$ ($\bar{K}'$) as $n_{2D} = g_v k_F^2/2\pi = 3.8 \pm 0.6 \times 10^{13}$ cm^{-2}, where $g_v = 2$ is the valley multiplicity and $k_F = 0.11 \pm 0.01$ $\mathring{A}^{-1}$ the measured Fermi wavevector, corresponding to be around 0.03 ± 0.005 electrons per surface unit cell.

Although the valence band has weak spectral weight at the zone center, we can estimate from our data that it lies within $50 - 100$ meV from the valence band at the $\bar{K}$ point, indicating an approximately direct nature of the band gap here, as for isolated monolayer MoS_2 (Mak et al., 2010; Splendiani et al., 2010). The direct band gap at the $\bar{K}$ point extracted from our ARPES data is 1.86 ± 0.02 eV, as shown in figure 6.2 (a) and in excellent agreement with the direct band gap of monolayer MoS_2 of 1.88 eV estimated from photoluminescence (Mak et al., 2010). From EDC fits to our measured dispersions, we extract an effective mass for the highest valence band states at $\bar{K}$ to be 0.6 ± 0.08 m_e. This is very similar to the conduction band effective mass at $\bar{K}$ discussed above, leading to a large joint density of states for optical transitions between the band edges. This is likely important to aid understanding and optimizing the high sensitivity of atomically-thin MoS_2 based photodetectors, (Lopez-Sanchez et al., 2013) as well as enabling the efficient optical generation of valley-polarized carrier populations in monolayer MoS_2, (Zeng et al., 2012; Mak et al., 2012; Cao et al., 2012). This is the key to propose optoelectronic and valleytronic applications of this material.

6.1.5   X-ray photoemission spectroscopy of MoS_2

The x-ray photoemission spectroscopy (XPS) is known to be a proper technique to investigate the chemical composition near the surface of the sample. Together with our ARPES data, these findings strongly support that the electronic structure we are probing here is characteristic of monolayer rather than

bulk of MoS_2. To uncover the origins of this, we combine chemical analysis from XPS with DFT calculations. As shown in figure 6.5 (a), a wide binding energy range from 0 to 40 eV includes the MoS_2 valence bands and shallow core levels of molybdenum (Mo 4p, $E_B \approx 35 - 40$ eV) and potassium (K 3p, $E_B \approx 18 - 21$ eV). For the freshly cleaved sample, no potassium signal is detected as expected and sharp valence band and Mo 4p features are observed. After potassium evaporation, these peaks shift to higher binding energy as a result of the electron doping and a clear K 3p peak emerges. From the relative intensity of the Mo and K core levels, we estimate the surface coverage of potassium to be 0.06 atoms per unit cell of MoS_2 (figure 6.5 (b)). Intriguingly, over a timescale of about 10 mins, the intensity of this potassium core-level peak is strongly diminished. Moreover, we observed a partial shift of spectral weight from both the K 3p and Mo 4p peaks to higher binding energy indicating a change in the local environment of the potassium atoms. Desorption seems unlikely at the deposition and measurement temperature of 20 K and the conduction band is degenerately-doped after this transition. Therefore, we attribute these changes in the XPS spectra to the intercalation of potassium into the vdW gap between neighbouring MoS_2 units.

6.2 Calculation part

As mentioned earlier, the calculation part has been done by my coauthor. This result is shown to fulfil the storyline of our measurement and conclusion. In this part, the formation energy which is in very good agreement with our XPS data will be presented. Different attempts of DFT calculation will be shown. The good agreement between ARPES result and the c/a expansion model has been performed. Finally, the overall and conclusion of this work is then followed. Note that more details of the calculation are shown in appendix A.2.
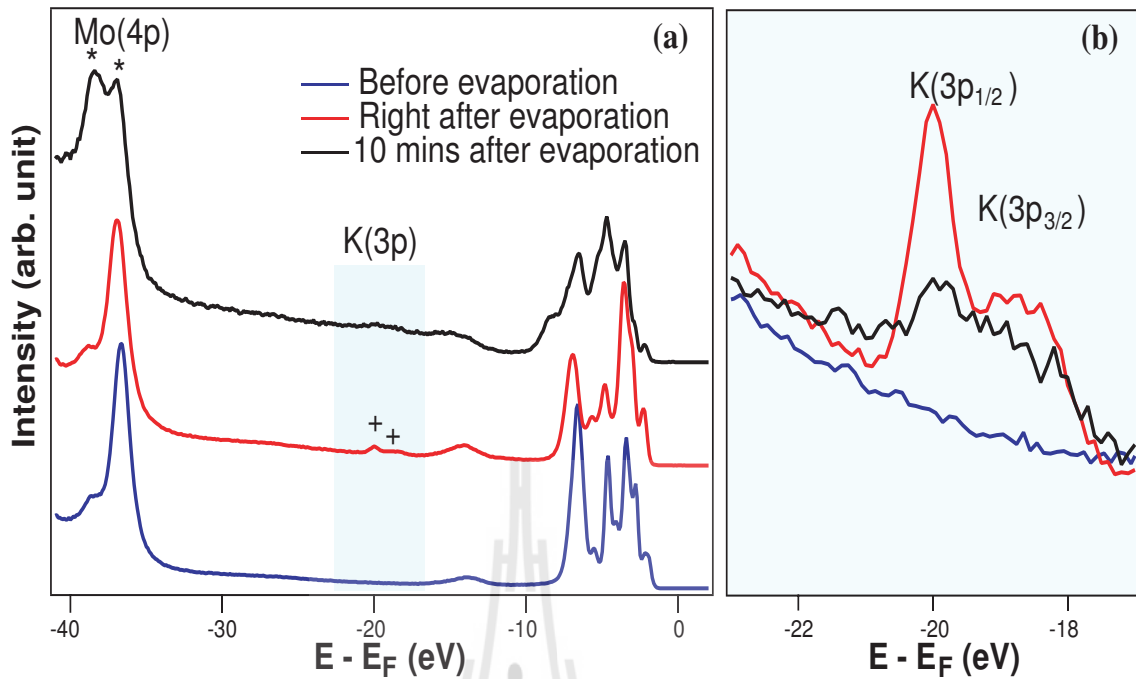
Figure 6.5 (a) XPS spectra of MoS_2 taken before and after potassium evaporation. (b) Magnified view represents the variation of the potassium K 3p core-level photoemission in a function of time (Eknapakul et al., 2014).

6.2.1 Formation energy

Formation energy (E_{form}) is the energy that the system need to form a new system. Firstly, from our model, two separated layers of potassium and MoS_2 are displayed with reference energy of zero (shown by red-dashed line). This means no energy needed to remain in this state. However, if the system is disturbed, for example, if we attach these two layered together, this will possibly lead to many kinds of chemical reaction. In this section, the simple model of potassium adsorption and intercalation is illustrated in figure 6.6 (a) and (b), respectively. More details of formation energy calculation are presented in appendix A.2.5. The lower E_{form} means the system is likely to be in that state while the energy higher than zero is not possible to happen in the model. In figure 6.6 (a), the

E_{form} has been calculated as a function of bond breaking energy referred to the strength of potassium bonding. Here, the E_{form} for intercalation model is lower than adsorption model in the range of our calculation. This is fully supported by our XPS that potassium is intercalated in the first vdW gap rather than to be adsorbed on the surface.
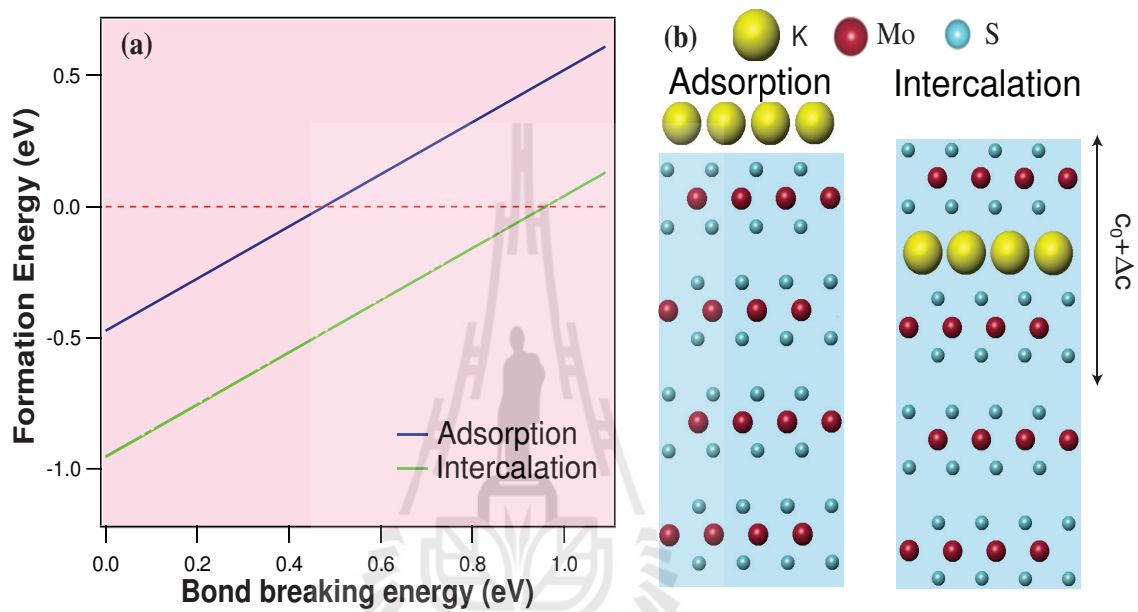
Figure 6.6 a) Formation energies for placing a monolayer of potassium on top of bulk MoS_2 and intercalated within the first vdW gap as derived from supercell DFT calculation. b) Simple model of potassium adsorption (left) and intercalation (right) (Eknapakul et al., 2014).

6.2.2 Possible model of potassium intercalated MoS_2

Many different models are applied to our DFT calculation. The full discussion is included in the appendix A.2. Our calculated bulk MoS_2 which is in agreement with other published calculation (Ellis et al., 2011) is shown in figure 6.7 (a). This model shows the VBM at $\bar{\Gamma}$ and CBM at $\bar{K}$. The potassium dosed-

bulk MoS$_2$ is then performed with a big shift of conduction band to higher binding energy but the VBM and CBM are still at the same position (figure 6.7 (b)). The calculations of intercalation and adsorption with relaxed lattice constant are performed in figure 6.7 (c) and (d). More bands resulted from potassium have been revealed in both calculation. Additionally, the potassium crossed band is represented in the adsorption case indicating metallic behaviour of this model. Finally, these model are not in agreement with our measurement, but at least, they can provide more understanding to our system

6.2.3 The c/a expansion model

From the previous report, we note that vdW gaps expanded as much as 30% have been reported in bulk potassium intercalated-MoS$_2$ (Somoano et al., 1973). Thus, for sufficient increase in interlayer spacing, each MoS$_2$ unit effectively becomes an isolated monolayer. We find good agreement between our theoretical and experimental dispersions here for an increase in the c/a ratio of around 25%. While large, a similar increase of the first vdW gap below the surface therefore seems reasonable here, leading to an isolated quasi-freestanding monolayer at the surface of a bulk MoS$_2$ crystal. Our work also suggests that superconductivity in alkali metal doped-MoS$_2$ (Somoano et al., 1973), with similar vdW gap sizes as for the surface here, emerges from an electronic structure characteristic of a series of stacked monolayers rather than bulk like MoS$_2$. This will likely be key to understanding a putative unconventional dome of superconductivity formed from both electrically-gated and intercalated-MoS$_2$ samples (Ye et al., 2012). Intercalating potassium into this vdW gap would be expected to increase the interlayer spacing, and we propose that this drives a crossover from a bulk- to monolayer like electronic structure in our samples (Mrstik et al., 1977; Kadowaki and Aika, 1993).
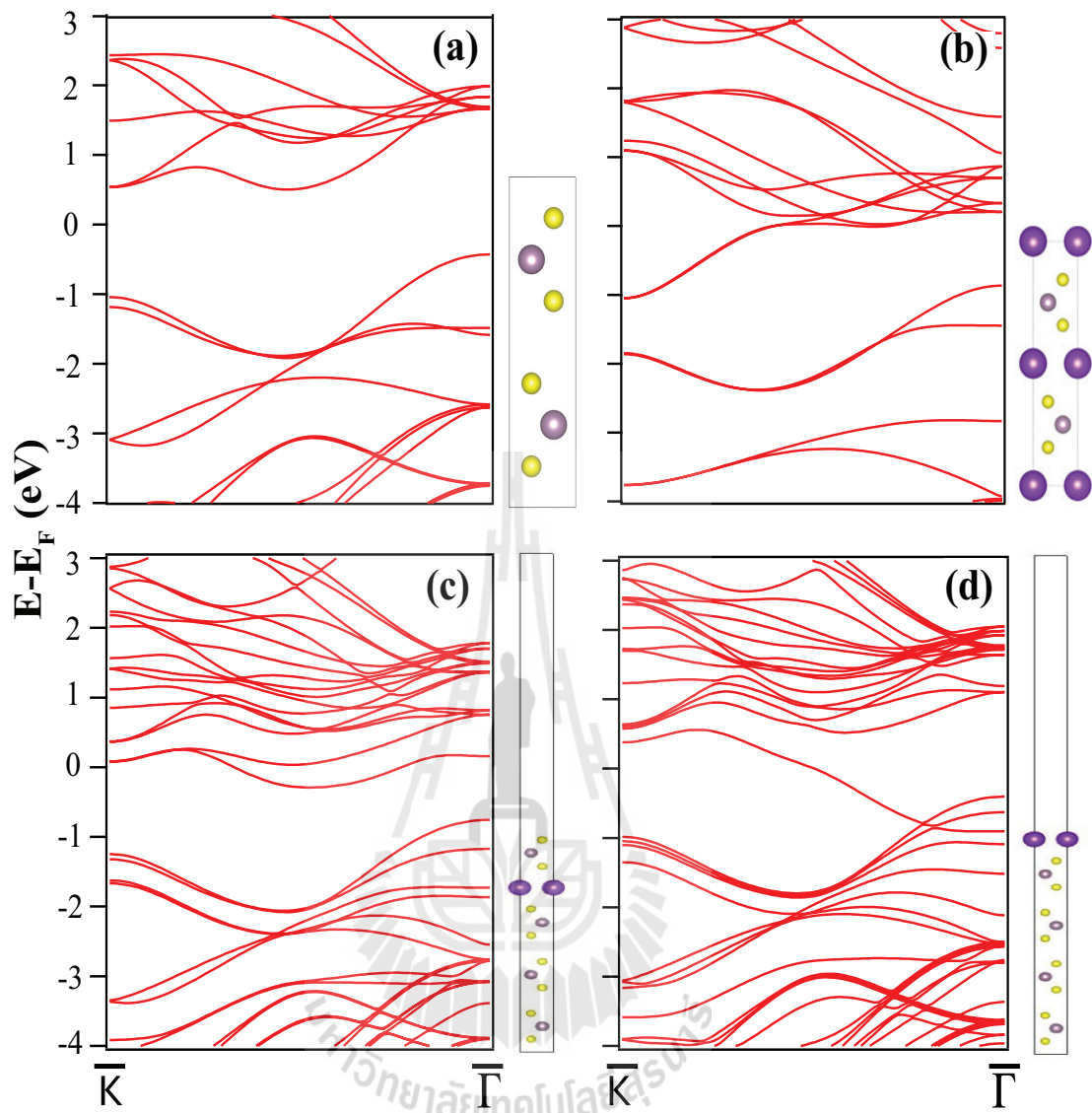
Figure 6.7 The calculated-band structure performing by DFT calculation a) bulk MoS_2 b) Maximum potassium to be dosed into the MoS_2 structure c) intercalation model, and d) adsorption model. The right figures next to each band structure calculations represent the simple calculation model.

Our DFT calculations (figure 6.8) reveal just such a transition with increasing c/a ratio (*i.e.*, expansion of the vdW gap) of a bulk MoS_2 unit cell. These calculations neglect spin-orbit interactions, allowing us to monitor the energy splitting of the valence band maxima at $\bar{K}$ as a metric of the strength of interlayer interactions

in the material. With increasing c/a ratio, this splitting is reduced to near zero, indicating a negligible coupling between neighbouring MoS_2 units along the z-axis for c/a ratios above around 4.9 (vdW gaps is larger than 4.69 $\mathring{A}$). The effects of this are much more dramatically close to $\bar{\Gamma}$ and $\bar{\Sigma}$ where the electronic states have significant S 2p character in contrast to the almost completely Mo d-derived character of the $\bar{K}$ point states. Consequently, the interlayer interaction in bulk is significantly stronger leading to much larger energy splittings (Cappelluti et al., 2013). The weakening of the interlayer coupling by the vdW gap expansion here drives a dramatic reduction of these energy splittings, eventually resulting in an inversion of the ordering of band extrema at $\bar{K}$ and along the $\bar{\Gamma}$–$\bar{K}$ line.

Finally, we note that even for the monolayer like electronic structure we observe here, we still find a splitting in the valence bands at the $\bar{K}$ point (figure 6.1 (c)). The persistent splitting, even with negligible interlayer interactions, reflects a significant influence of spin-orbit coupling on the monolayer like electronic structure, not considered in our DFT calculations above, but permitted by the broken inversion symmetry of the surface monolayer. This confirms the strong potential of MoS_2 and related compounds for spintronic applications. (Morpurgo, 2013) Moreover, it suggests that the prospects for valleytronics offered by monolayer MoS_2 (Xiao et al., 2012; Cao et al., 2012; Zeng et al., 2012; Mak et al., 2012) should also be realized in the quasi-freestanding monolayer created here. Unlike mechanical exfoliation, however, our methodology allows the possibility to continuously tune the electronic structure from bulk- to monolayer-like by controlling the vdW gap expansion by intercalating different quantities of potassium or atoms of different sizes. Moreover, it raises the prospect to reversibly drive this crossover in TMDs by sequential intercalation and deintercalation, as has recently been achieved for graphene (Larciprete et al., 2012). Together, our work establishes

intercalation at the surface of bulk TMDs as an efficient route to generate large area quasi-freestanding monolayers for use in advanced fundamental study and potential practical applications of MoS_2 and other atomic scale transition metal dichalcogenides.
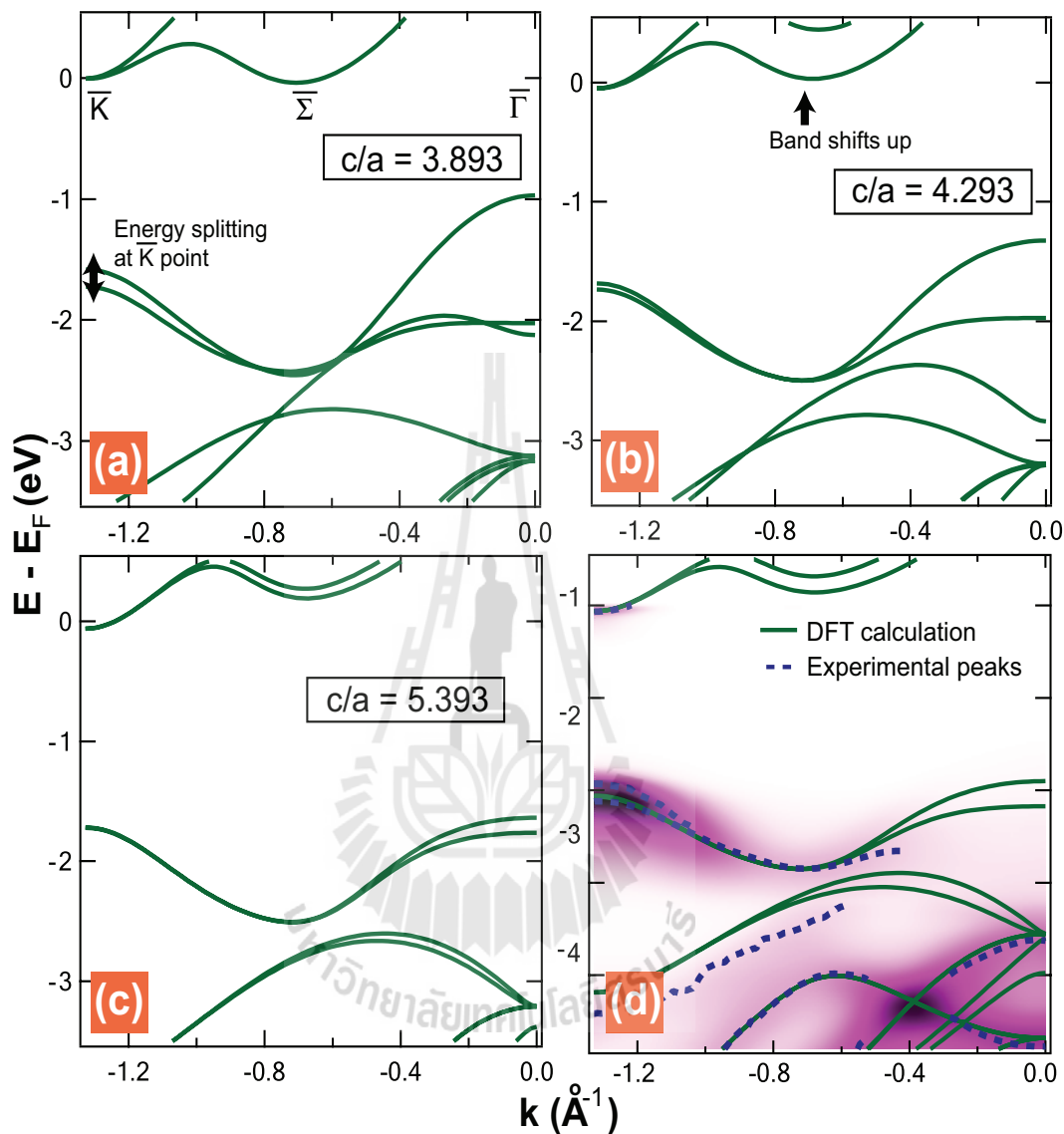
Figure 6.8 (a)-(c) DFT band structure calculations for MoS_2 with different inter-layer spacings indicated by ratio between out-of-plane and in-plane lattice constant (c/a). (d) Comparison between our measured ARPES data, extracted dispersions from fitting EDCs, and the theoretical calculation for c/a = 4.893, showing good agreement (Eknapakul et al., 2014).

CHAPTER VII

RELATED STUDIES OF OTHER

LAYERED-TRANSITION METAL

DICHALCOGENIDES

The layered-TMDs are one of the most popular materials to be used in future nano electronics. Here, I will describe the studies of some layered-TMDs which I am the part of the projects led by Dr. Philip King and Asst. Prof. Worawat Meevasana.

In this chapter, the published results of WSe_2 as well as the preliminary results of $PdTe_2$ and $HfSe_2$ will be presented. Firstly, I will begin with the study of WSe_2 focusing on the negative electronic compressibility (NEC) and tuneable spin splitting by evaporating alkali metal (potassium and rubidium) on the surfaces. I am one of the coauthors in this work contributed in the ARPES experiment (Riley et al., 2015). The key of this work is, the submonolayer deposition of alkali metals at the surface can result to the charge accumulation induced 2DEG (figure 7.1 (a)). This surface electron doping breaks the layer degeneracy giving the splitting of the valence band minimum (figure 7.1 (b)). The smaller band gap in this measurement can be explained by the effect of NEC which drives the stronger downward band bending of the conduction band compared to the valence band.

Next, I will give some preliminary result of $PdTe_2$. $PdTe_2$, the one of layered-TMDs exhibits a very good conducting. Recent observation of superconductivity in strong spin-orbit coupled 4d and 5d transition metal-based compound
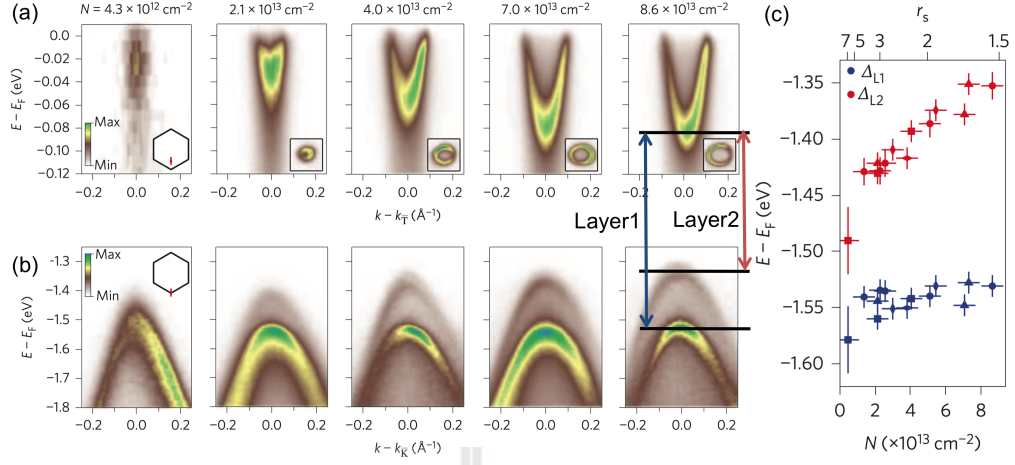
Figure 7.1 Tuneable valley spin splitting a) ARPES measurements of the dispersion of 2DEG formed along the halfway of $\bar{\Gamma} - \bar{K}$ direction. b) The corresponding evolution of VBM at $\bar{K}$. c) Binding energy of the valence states in near-surface layers revealing a pronounced decrease in binding energy with increasing surface-electron density. (Riley et al., 2015)

in $A_x PdTe_2$ (A = Ta, Nb) up to 6 K with high critical field (Jiao et al., 2014). The dramatically change of the band structure in $PdTe_2$ has been expected if they are thinned down to the monolayer. Here, as a result of symmetry protection of p orbital in this system, we observed two interesting bands which are originated from p orbital but separated by different symmetry protection. These two bands lead the way to different novel quantum effects in this material; the 3D-Dirac point and the Inverted Rashba splitting (shown in figure 7.2).

The last layered-TMD which will be discussed in this the is $HfSe_2$. $HfSe_2$ is known to have the CdI_2 structure and exhibits a semiconducting property. This structure is similar to the MoS_2 structure but two chalcogen atoms are located in the opposite site referred to the hafnium atom. This leads to the anisotropic property in this material (Zhang et al., 2014a). This material has an indirect band
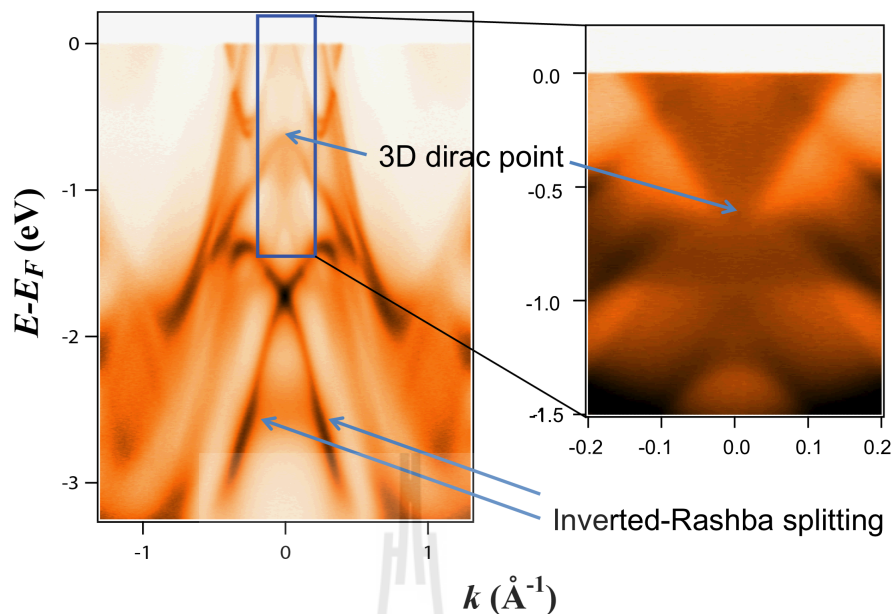
Figure 7.2 a) Electronic band structure of PdTe$_2$ along $\Gamma - K$ direction indicating the sign of 3D Dirac-point at the Γ point, magnified in the right figure. At high binding energy (E$_B$ $\sim$ 1-3 eV), the 2D state demonstrating the feature of the inverted-Rashba splitting has been observed.

gap of 1.13 eV translated from $\bar{\Gamma}$ to $\bar{M}$ of the brillouin zone exhibiting the highest electron mobility among its family (Zhang et al., 2014a). This material has been studied in the uses of photovoltaic application and new class solar cell (Radhakrishnan and Pilla, 2008). We measured the anisotropy conduction pocket in this material. Interestingly, by evaporating huge amount of sodium on their surfaces, the 2D-electronic structure with effective mass around 1 m$_e$ has been observed, indicating the uniformly arrangement and isolation of sodium atoms on the HfSe$_2$ substrate. More measurements are in progress to study the fundamental physics of the HfSe$_2$ electronic structure as well as the arrangement of sodium atoms and other akali metals (shown in figure 7.3).
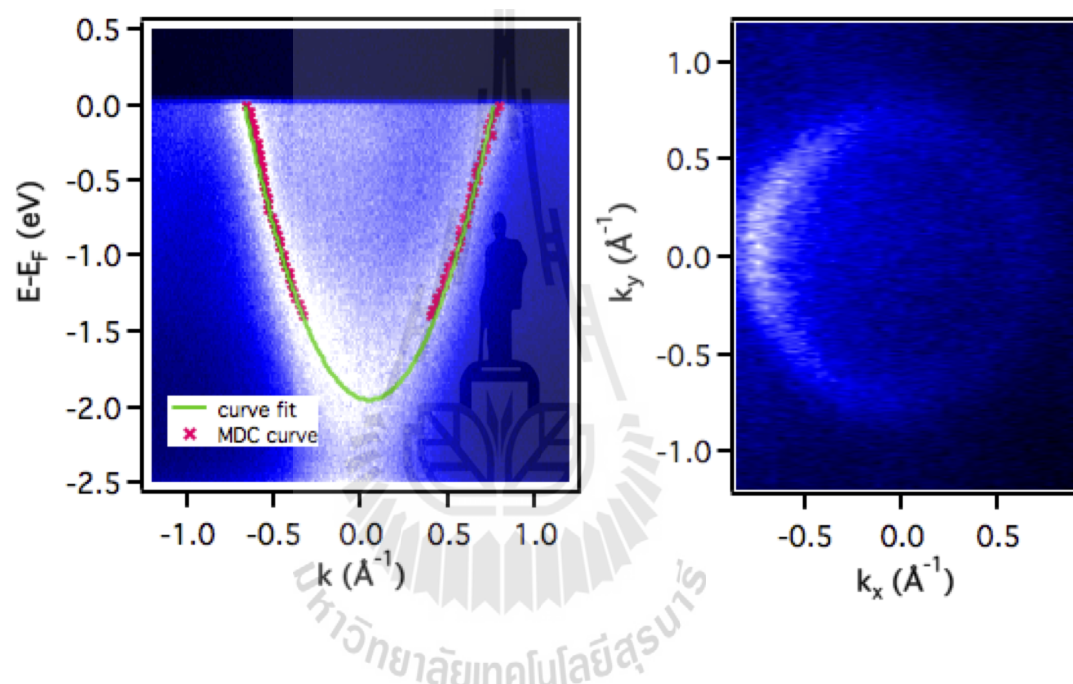
Figure 7.3 a) Conduction pocket measured at the Γ point of the Brilluoin zone of HfSe$_2$. b) Corresponding circular Fermi surface of a). This two-dimensional like band may indicate the surface state of sodium film on HfSe$_2$.

CHAPTER VIII

CONCLUSIONS AND FUTURE DIRECTION

8.1 Conclusion of ARPES studies and relating works

For the works relating to the study of two-dimensional electronic structures at the surfaces of $SrTiO_3$ and $KTaO_3$, which I am one of the coauthors, we learned that the 2D electronic structure can emerge from the electron accumulation at the surfaces; this nature is similar to the nature of quasi-freestanding layer of MoS_2. Besides this, the studies helped me learning how to check the 2D character by using photon energy dependent measurement later used in the MoS_2 study. For the ARPES study of electronic structure of MoS_2, we were able to see the spin-orbit splitting around 176 meV at valence band maximum. This is in agreement with the calculations. We have found the striking cross over from indirect to direct band gap in MoS_2 after potassium dosing, reflecting the quasi-freestanding of monolayer on bulk MoS_2. This argument is apparently seen in the direct band gap of 1.86 eV at $\bar{K}$ point of dosed-sample. We interpret this change as caused by c-axis expansion of vdW gap of MoS_2 affected by the intercalated-potassium. We have also confirmed this hypothesis by performing the quantitative agreement with DFT calculation. As a result, by expanding c-axis of MoS_2 and adding electron comparable with potassium amount, the calculation is very consistent with the optical data. From the DFT calculation, the potassium intercalation also gives the lowest formation energy. Besides these features, we confirmed the 2D character of the conduction band as shown by photon energy dependent measurement.

8.2 Future direction

Apart from our ARPES measurement on MoS_2, we have been studying other related TMDs due to their similarly layered structure. As mentioned before, even in the similar structure, the TMDs exhibit various properties in different compounds in their family (i.e. the transition from semiconducting to conducting by changing elements). We have performed more ARPES measurement of three other different TMD compounds including $PdTe_2$, WSe_2, and $HfSe_2$. These materials have the same geometrical properties (dark silver and shining) but completely different electrical properties. $PdTe_2$ is very good conducting while WSe_2, and $HfSe_2$ are semiconductors. We have presented some published results about spin-polarized electronic structure and negative electronic compressibility on WSe_2. We have given some interesting preliminary results about $PdTe_2$ and $HfSe_2$. In the future, more ARPES studies and more analysis methods to understand the orbital ordering, polarization and photon dependence on these materials will be very interesting and would be my future study.

REFERENCES

REFERENCES

Adelsberger, K. E., Curda, J., Vensky, S., and Jansen, M. (2001a). High-pressure synthesis and electrochemical investigation of $Ag_2Cu_2O_3$. **J. Solid State Chem.** 158: 82.

Adelsberger, K. E., Prigent-Croguennec, L., and Jansen, M. (2001b). Electrochemical deintercalation of Ag_2PbO_2. **Z. Anorg. Allg. Chem.** 627: 2473.

Alexiev, V., Prins, R., and Weber, T. (2000). Ab initio study of MoS_2 and Li adsorbed on the (1010) face of MoS_2. **Phys. Chem. Chem. Phys.** 2: 1815.

Apell, S. P., Hanson, G. W., and Hägglund, C. (2012). High optical absorption in graphene. **arXiv**: 1201.3071.

Balog, R., Jørgensen, B., Nilsson, L., Andersen, M., Rienks, E., Bianchi, M., Fanetti, M., Lægsgaard, E., Baraldi, A., Lizzit, S., Sljivancanin, Z., Besenbacher, F., Hammer, B., Perdersen, T. G., Hofmann, P., and Hornekær, L. (2010). Bandgap opening in graphene induced by patterned hydrogen adsorption. **Nat. Mater.** 9: 315.

Bardeen, J. (1947). Surface states and rectification at a metal semi-conductor contact. **Phys. Rev.** 71: 717.

Bark, C., Felker, D., Wang, Y., Zhang, Y., Jang, H., Folkman, C., Park, J., Baek, S., Zhou, H., Fong, D., Pan, X., Tsymbal, E., Rzchowski, M., and Eom, C. B. (2011). Tailoring two dimensional electron gas at the

LaAlO$_3$/SrTiO$_3$(001) interface by epitaxial strain. **Proc. Natl. Acad. Sci. USA** 108(12): 4720.

Bark, C., Sharma, P., Wang, Y., Baek, S., Lee, S., Ryu, S., Folkman, C. M., Paudel, T. R., Kumar, A., Kalinin, S. V., Sokolov, A., Tsymbal, E. Y., Rzchowski, M. S., Gruverman, A., and Eom, C. B. (2012). Switchable induced polarization in LaAlO$_3$/SrTiO$_3$ heterostructures. **Nano Lett.** 12: 1765.

Beal, A. R. and Hughes, H. P. (1979). Kramers-Kronig analysis of the reflectivity spectra of 2H-MoS$_2$, 2H-MoSe$_2$ and 2H-MoTe$_2$. **J. Phys. C** 12: 881.

Bednorz, J. G. and Muller, K. A. (1988). Perovskite-type oxides: The new approach to high-T$_c$ superconductivity. **Mod. Phys.** 60: 585.

Bert, J. A., Kalisky, B., Bell, C., Kim, M., Hikita, Y., Hwang, H., and Moler, K. A. (2011). Direct imaging of the coexistence of ferromagnetism and superconductivity at the LaAlO$_3$/SrTiO$_3$ interface. **Nature Phys.** 7: 767.

Biagi, R., Fantini, P., Renzi, V. D., Betti, M. G., Mariani, C., and Penino, U. (2003). Photoemission investigation of the alkali-metal-induced two-dimensional electron gas at the Si(111)(1×1) :H surface). **Phys. Rev. B** 67: 155325.

Bianchi, M., Guan, D., Bao, S., Mi, J. L., Iversen, B. B., , King, P. D. C., and Hofmann, P. (2010). Coexistence of the topological state and two-dimensional electron gas on the surface of Bi$_2$Se$_3$. **Nat. Comm.** 1: 128.

Blöchl, P. E. (1994). Projector augmented-wave method. **Phys. Rev. B** 50: 17953.

Bostwick, A., Speck, F., Seyller, T., Horn, K., Polini, M., Asgari, R., MacDonald,

A. H., and Rotenberg, E. (2010). Observation of plasmarons in quasi-Freestanding doped graphene. **Science** 328: 999.

Britnell, L., Gorbachev, R. V., Jalil, R., Belle, B. D., Schedin, F., Mishchenko, A., Georgiou, T., Katsnelson, M. I., Eaves, L., Morozov, S. V., Peres, N. M. R., Leist, J., Geim, A. K., Novoselov, K. S., and Ponomarenko, L. A. (2012). Field-effect tunneling transistor based on vertical graphene heterostructures. **Science** 335: 947.

Buchenberg, W. (2010). **Spintronics**. Faculty of Physics, Albert-Ludwigs-Universität Freiburg.

Bychkov, Y. A. and Rashba, E. I. (1984). Properties of a 2D electron gas with lifted spectral degeneracy. **JETP Lett.** 39(2): 78.

Cabrera, N. and Mott, N. F. (1949). Theory of the oxidation of metals. **Rep. Prog. Phys.** 12: 163.

Cao, T., Wang, G., Han, W., Ye, H., Zhu, C., Shi, J., Niu, Q., Tan, P., Wang, E., Liu, B., and Feng, J. (2012). Valley-selective circular dichroism of monolayer molybdenum disulphide. **Nat. Comm.** 3: 887.

Cappelluti, E., Roldán, R., Silva-Guillén, J., Ordejón, P., and Guinea, F. (2013). Tight-binding model and direct-gap/indirect-gap transition in single-layer and multilayer MoS$_2$. **Phys. Rev. B** 88: 075409.

Catalano, I. M., Cingolani, A., and Minafra, A. (1974). Transmittance, luminescene, and photocurrent in CdS under two-photon excitation. **Phys. Rev. B** 9: 707.

Cen, C., Thiel, S., Mannhart, J., and Levy, J. (2009). Oxide nanoelectronics on demand. **Science** 323: 1026.

Cheiwchanchamnangij, T. and Lambrecht, W. R. L. (2012). Quasiparticle band structure calculation of monolayer, bilayer and bulk MoS_2. **Phys. Rev. B** 85: 205302.

Chen, H. J., Huang, J., Lei, X. L., Wu, M. S., Liu, G., Ouyang, C. Y., and Xu, B. (2012). Adsorption and diffusion of lithium on MoS_2 monolayer: The role of strain and concentration. **Int. J. Electrochem. Sci.** 8: 2196.

Coehoorn, R., Haas, C., Dijkstra, J., and Flipse, C. J. F. (1987). Electronic structure of $MoSe_2$, MoS_2, and WSe_2. I. Band-structure calculations and photoelectron spectroscopy. **Phys. Rev. B** 35: 6195.

Coleman, J. N., Lotya, M., O'Neill, A., Bergin, S. D., King, P., Khan, U., Young, K., Gaucher, A., De, S., Smith, R. J., Shvets, I. V., Arora, S. K., Stanton, G., Kim, H.-Y., Lee, K., Kim, G. T., Duesberg, G. S., Hallam, T., Boland, J. J., Wang, J., Donegan, J. F., Grunlan, J. C., Moriarty, G., Shmeliov, A., Nicholls, R. J., Perkins, J. M., Grieveson, E. M., Theuwissen, K., McComb, D. W., Nellist, P. D., and Nicolosi, V. (2011). Two-dimensional nanosheets produced by liquid exfoliation of layered materials. **Science** 331: 568.

Damascelli, A. (2004). Probing the electronic structure of complex systems by ARPES. **Phys. Scripta** T109: 61.

Damascelli, A., Hussain, Z., and Shen, Z.-X. (2003). Angle-resolved photoemission studies of the cuprate superconductors. **Rev. Mod. Phys.** 75: 473.

Diehl, R. D. and McGrath, R. (1996). Structural studies of alkali metal adsorption and coadsorption on metal surfaces. **Surf. Sci. Rep.** 23: 43.

Dirac, P. A. M. (1928). The quantum theory of the electron. **Proc. R. Soc. A** 117: 610.

Eda, G., Fanchini, G., and Chhowalla, M. (2008). Large-area ultrathin films or reduced graphene oxides as a transparent and flexible electronic material. **Nat. Nanotechnol.** 3: 270.

Eknapakul, T., King, P. D. C., Asakawa, M., Buaphet, P., He, R. H., Mo, S.-K., Takagi, H., Shen, K. M., Baumberger, F., Sasagawa, T., Jungthawan, S., and Meevasana, W. (2014). Electronic structure of quasi-freestanding MoS_2 monolayer. **Nano Lett.** 14: 1312.

Ellis, J. K., Lucero, M. J., and Scuseria, G. E. (2011). The indirect to direct band gap transition in multilayered MoS_2 as predicted by screened hybrid density functional theory. **Appl. Phys. Lett.** 99: 261908.

Engels, G., Lange, J., Schapers, T., and Luth, H. (1997). Experiment and theo-retical approach to spin splitting in modulation-doped $In_xGa_{1-x}As/InP$ quantum wells for B $\rightarrow$0. **Phys. Rev. B** 55: R1958.

Falkovsky, L. A. (2008). Optical properties of graphene. **J. Phys.: Conf. Ser.** 129: 012004.

Fang, H., Tosun, M., Seol, G., Chang, T. C., Takei, K., Guo, J., and Javey, A. (2013). Degenerate n-doping of few-layer transition metal dichalcogenides by potassium. **Nano Lett.** 13: 1991.

Fang, L., Shen, M., and Cao, W. (2004). Effects of postanneal conditions on the di-electric properties of $CaCu_3Ti_4O_{12}$ thin films prepared on $Pt/Ti/SiO_2/Si$ substrates. **J. Appl. Phys.** 95: 6483.

Fang, T. T., Mei, L. T., and Ho, H. F. (2006). Effects of Cu stoichiometry on the microstructures, barrier-layer structures, electrical conduction, dielectric responses, and stability of $CaCu_3Ti_4O_{12}$. **Acta Mater.** 54: 2867.

Fontana, M., Deppe, T., Boyd, A. K., Rinzan, M., Liu, A. Y., Paranjape, M., and Barbara, P. (2013). Electron-hole transport and photovoltaic effect in gated MoS_2 Schottky junctions. **Sci. Rep.** 3: 1634.

Frey, G. L., Tenne, R., Matthews, J., Dresselhaus, M. S., and Dresselhaus, G. (1998). Optical properties of MS_2 (M=Mo, W) inorganic fullerenelike and nanotube material optical adsorption and resonance raman measurements. **J. Mater. Res.** 13: 2412.

Friend, R. H. and Yoffe, A. D. (1987). Electronic properties of intercalation complexes of the transition metal dichalcogenides. **Adv. Phys.** 36: 1.

Frindt, R. F. and Yoffe, A. D. (1963). Optical properties and photoconductivity of thin crystals of molybdenum disulphide. **Proc. R. Soc. Lond. A** 273: 69.

Fujimori, A., Suga, S., Negishi, H., and Inoue, M. (1988). X-ray photoemission and Auger-electron spectroscopic study of the electronic structure of intercalation compounds M_xTiS_2 (M=Mn, Fe, Co, and Ni). **Phys. Rev. B** 38(6): 3676.

Ganal, P., Olberding, W., Butz, T., and Ouvrard, G. (1993). Soft chemistry induced host metal coordination change from octahedral to trigonal prismatic in $1T-TaS_2$. **Solid state Ionics** 59: 313.

Geim, A. K. and Novoselov, K. S. (2007). The rise of graphene. **Nat. Mater.** 6: 183.

Gierz, I. (2011). **Investigation of two-dimensional electron gases with angular resolved photoemission spectroscopy**. Ph.D. thesis, Max Planck Institute for Solid State Research, Stuttgart, Germany.

Gmelin, L. (1995). **Handbook of inorganic and organometallic chemistry**. Berlin: Springer–Verlag.

Grimme, S. (2006). Semiempirical GGA-type density functional constructed with a long-range dispersion correction. **J. Comp. Chem.** 27: 1787.

Grundler, D. (2000). Large Rashba splitting in InAs quantum wells due to electron wave function penetration into the barrier layers. **Phys. Rev. Lett.** 84: 6074.

Guo, H., Lu, N., Wang, L., Wu, X., and Zeng, X. C. (2014). Tuning electronic and magnetic properties of early transition-metal dichalcogenides via tensile strain. **J. Phys. Chem. C** 118: 7242.

Ham, F. S. (1962). Energy bands of alkali metals II. Fermi surface. **Phys. Rev.** 128(6): 2524.

Hasegawa, T., Mouri, S., Yamada, Y., and Tanaka, K. (2003). Giant photo-induced dielectricity in $SrTiO_3$. **J. Phys. Soc. Jpn.** 72: 2003.

H*ü*fner, S. (1995). **Photoemission spectroscopy**. Berlin: Springer–Verlag.

Heine, V. (1965). Theory of surface states. **Phys. Rev.** 138: A1689.

Hertz, H. (1887). Ueber den Einfluss des ultravioletten Lichtes auf die electrische Entladung. **Ann. Phys.** 267: 983.

Imanishi, N., Toyoda, M., Takeda, Y., and Yamamoto, O. (1992). Study on lithium intercalation into MoS_2. **Solid State Ionics** 58: 333.

Jacobson, A. J. and Whittingham, M. S. (1982). **Intercalation Chemistry**. New York: Academic Press.

Jiamprasertboon, A., Okamoto, Y., Hiroi, Z., and Siritanon, T. (2014). Thermoelectric properties of Sr and Mg double-substituted $LaCoO_3$ at room temperature. **Ceram. Int.** 40: 12729.

Jiang, C. S. and Hasegawa, S. (1999). Photoconductivity of the Si(111)- 7×7 and $\sqrt{3} \times \sqrt{3}$-Ag surfaces. **Surf. Sci** 427: 239.

Jiao, W.-H., Tang, Z.-T., Sun, Y.-L., Liu, Y., Tao, Q., Feng, C.-H., Zeng, Y.-W., Xu, Z.-A., and Cao, G.-H. (2014). Superconductivity in a layered $Ta_4Pd_3Te_{16}$ with $PdTe_2$ chains. **J. Am. Chem. Soc.** 136: 1284.

Jin, W., Yeh, P.-C., Zaki, N., Zhang, D., Sadowski, J. T., Al-Mahboob, A., Zande, A. M., Chenet, D. A., Dadap, J. I., Herman, I. P., Sutter, P., Hone, J., and Osgood, R. M. (2013). Direct measurement of the thickness-dependent electronic band structure of MoS_2 using angle-resolved photoemission spectroscopy. **Phys. Rev. Lett.** 111: 106801.

Kadowaki, Y. and Aika, K. (1993). Surface structure of $MoS_2(001)$ determined by coaxial impact-collision ion scattering spectroscopy (CAICISS). **Surf. Sci.** 287: 396.

Kaul, A. (2013). Two-dimensional atomic layered materials and their applications. **SPIE Newsroom** 10.1117: 2.1201310.005093.

Kedesy, H. (1954). Calculation of position and indices of Laue spots on Laue-photographs. **Am. Jour. Sci.** 39: 750.

Kimura, T., Goto, T., Shintani, H., Ishizaka, K., Arima, T., and Tokura, Y. (2003). Magnetic control of ferroelectric polarization. **Nature** 426: 55.

King, P. D. C., Hatch, R. C., Bianchi, M., Ovsyannikov, R., Lupulescu, C., Landolt, G., Slomski, B., Dil, J. H., Guan, D., Mi, J. L., Rienks, E. D. L., Fink, J., Lindblad, A., Svensson, S., Bao, S., Balakrishnan, G., Iversen, B. B., Osterwalder, J., Eberhardt, W., Baumberger, F., and Hofmann, P. (2011). Large tunable Rashba spin splitting of a two dimensional electron gas in Bi_2Se_3. **Phys. Rev. Lett.** 107: 096802.

King, P. D. C., He, R. H., Eknapakul, T., Buaphet, P., Mo, S.-K., Kaneko, Y., Harashima, S., Hikita, Y., Bahramy, M. S., Bell, C., Hussain, Z., Tokura, Y., Shen, Z.-X., Hwang, H. Y., Baumberger, F., and Meevasana, W. (2012). Subband structure of a two-dimensional electron gas formed at the polar surface of the strong spin-orbit perovskite $KTaO_3$. **Phys. Rev. Lett.** 108: 117602.

King, P. D. C., McKeown Walker, S., Tamai, A., de la Torre, A., Eknapakul, T., Buaphet, P., Mo, S.-K., Meevasana, W., Bahramy, M. S., and Baumberger, F. (2014). Quasiparticle dynamics and spin-orbital texture of the $SrTiO_3$ two-dimensional electron gas. **Nat. Comm.** 5: 3414.

Kresse, G. and Furthm$u$ller, J. (1996). Efficiency of ab-initio total energy calculations for metals and semiconductors using a plane-wave basis set. **Comput. Mater. Sci.** 6: 15.

Kuc, A., Zibouche, N., and Heine, T. (2011). Influence of quantum confinement on the electronic structure of the transition metal sulfide TS_2. **Phys. Rev. B** 83: 245213.

Kumar, A., Cs$\acute{a}$thy, G. A., Manfra, M. J., Pfeiffer, L. N., and West, K. W. (2010). Nonconventional odd-denominator fractional quantum Hall states in the second Landau level. **Phys. Rev. Lett.** 105: 246808.

Landau, L. D. (1937). Zur theoric der phasenumwandlungen II. Phys. **Z. Sowje-tunion** 11: 26.

Larciprete, R., Ulstrup, S., Lacovig, P., Dalmiglio, M., Bianchi, M., Mazzola, F., Hornekær, L., Orlando, F., Baraldi, A., Hofmann, P., and Lizzit, S. (2012). Oxygen switching of the epitaxial graphene-metal interaction. **ACS Nano** 6: 9551.

Lee, S. H., Min, S.-W., Chang, Y.-G., Park, M. K., Nam, T., Kim, H., Kim, J. H., Ryu, S., and Im, S. (2012). MoS_2 nanosheet phototransistors with thickness-modulated optical energy gap. **Nano. Lett.** 12: 3695.

Leroux, F., Rabu, P., Sommerdijk, N. A. J. M., and Taubert, A. (2015). Two-dimensional hybrid materials: transferring technology from Biology to Society. **Eur. J. Inorg. Chem.** 7: 1089.

Li, H., Yin, Z., He, Q., Li, H., Huang, X., Lu, G., Fam, D. W. H., Tok, A. I. Y., Zhang, Q., and Zhang, H. (2012). Fabrication of single and multilayer MoS_2 filmbased field effect transistors for sensing NO at room temperature. **Small** 8: 63.

Li, L., Richter, C., Mannhart, J., and Ashoori, R. C. (2011a). Coexistence of magnetic order and two-dimensional superconductivity at $LaAlO_3/SrTiO_3$ interfaces. **Nature Phys.** 7: 762.

Li, T., Xue, R., Hao, J., Xue, Y., and Chen, Z. (2011b). The effect of calcining temperatures on the phase purity and electric properties of $CaCu_3Ti_4O_{12}$ ceramics. **J. Alloys Compd.** 509: 1025.

Liang, W. Y. (1970). Excitons. **Phys. Educ.** 5: 125301.

Liqiang, J., Yichun, Q., Baiqi, W., Shudan, L., Baojiang, J., Libin, Y., Wei, F., Honggang, F., and Jaizhong, S. (2006). Review of photoluminescence performance of nano-sized semiconductor materials and its relationships with photocatalytic activity. **Sol. Energy Mater. Sol. Cells** 90: 1773.

Liu, G.-B., Shan, W.-Y., Yao, Y., Yao, W., and Xiao, D. (2013). Three-band tight-binding model for monolayers of group-VIB transition metal dichalcogenides. **Phys. Rev. B** 88: 085433.

Lopez-Sanchez, O., Lembke, D., Kayci, M., Radenovic, A., and Kis, A. (2013). Ultrasensitive photodetectors based on monolayer MoS_2. **Nat. Nanotechnol.** 8: 497.

Lunkenheimer, P., Bobnar, V., Pronin, A. V., Ritus, A. I., Volkov, A. A., and Loidl, A. (2002). Origin of apparent colossal dielectric constants. **Phys. Rev. B** 66: 052105.

Mak, K. F., He, K., Shan, J., and Heinz, T. F. (2012). Control of valley polarization in monolayer MoS_2 by optical helicity. **Nat. Nanotechnol.** 7: 494.

Mak, K. F., Lee, C., Hone, J., Shan, J., and Heinz, T. F. (2010). Atomically thin MoS_2: a new direct-gap semiconductor. **Phys. Rev. Lett.** 105: 136805.

Masingboon, C., Eknapakul, T., Suwanwong, S., Buaphet, P., Nakajima, H., Mo, S.-K., Thongbai, P., King, P. D. C., Maensiri, S., and Meevasana, W. (2013). Anomalous change in dielectric constant of $CaCu_3Ti_4O_{12}$. **Appl. Phys. Lett.** 102: 202903.

Mattheiss, L. F. (1973). Band structures of transition-metal-dichalcogenide layer compounds. **Phys. Rev. B** 8: 3719.

Meevasana, W., King, P. D. C., He, R. H., Mo, S.-K., Hashimoto, M., Tamai, A., Songsiriritthigul, P., Baumberger, F., and Shen, Z.-X. (2011). Creation and control of a two-dimensional electron liquid at the bare $SrTiO_3$ surface. **Nat. Mater.** 10: 114.

Meevasana, W., Zhou, X. J., Sahrakorpi, S., Lee, W. S., Yang, W. L., Tanaka, K., Mannella, N., Yoshida, T., Lu, D. H., Chen, Y. L., He, R. H., Lin, H., Komiya, S., Ando, Y., Zhou, F., Ti, W. X., Xiong, W., Zhao, Z. X., Sasagawa, T., Kakeshita, T., Fujita, K., Uchida, S., Eisaki, H., Fujimori, A., Hussain, Z., Markiewicz, R. S., Bansil, A., Nagaosa, N., Zaanen, J., Devereaux, T. P., and Shen, Z.-X. (2007). Hierarchy of multiple many-body interaction scales in high-temperature superconductors. **Phys. Rev. B** 75: 174506.

Morpurgo, A. F. (2013). Spintronics: Gate control of spin-valley coupling. **Nature Phys.** 9: 532.

Mrstik, B. J., Kaplan, R., and Reinecke, T. L. (1977). Surface-structure determination of the layered compounds MoS_2 and $NbSe_2$ by low-energy electron diffraction. **Phys. Rev. B** 15: 897.

Nakagawa, N., Hwang, H. Y., and Muller, D. A. (2006). Why some interfaces can never be sharp. **Nat. Mater.** 5: 204.

Nienhaus, H. (2002). Electronic excitations by chemical reactions on metal surfaces. **Surf. Sci. Rep.** 45: 3.

Nitta, J., Akazaki, T., and Takayanagi, H. (1997). Gate control of spin-orbit interaction in an inverted $In_{0.53}Ga_{0.47}As/In_{0.52}Al_{0.48}As$ heterostructure. **Phys. Rev. Lett.** 78: 1335.

Novoselov, K. S., Geim, A. K., Morozov, S. V., Jiang, D., Katsnelson, M. I., Grig- orieva, I. V., Dubonos, S. V., and Firsov, A. A. (2005a). Two-dimensional gas of massless Dirac fermions in graphene. **Nature** 438: 197.

Novoselov, K. S., Jiang, D., Schedin, F., Booth, T. J., Khotkevich, V. V., Morozov, S. V., and Geim, A. K. (2005b). Two-dimensional atomic crystals. **Proc. Natl. Acad. Sci. USA** 102(30): 10451.

Novoselov, K. S., Jiang, Z., Zhang, Y., Morozov, S. V., Stormer, H. L., Zeitier, U., Maan, J. C., Boebinger, G. S., Kim, P., and Geim, A. K. (2007). Room-temperature quantum Hall effect in graphene. **Science** 315: 1379.

Odom, B., Hanneke, D., D'Urso, B., and Gabrielse, G. (2006). New measurement of the electron magnetic moment using a one-electron quantum cyclotron. **Phys. Rev. Lett.** 97: 030801.

Ohtomo, A. and Hwang, H. Y. (2004). A high-mobility electron gas at the $LaAlO_3/SrTiO_3$ heterointerface. **Nature London** 427: 423.

Oura, K., Lifshifts, V. G., Saranin, A. A., Zotov, A. V., and Katayama, M. (2003). **Surface Science**. New York: Springer–Verlag.

Pankove, J. I. (1971). **Optical processes in semiconductors**. Dover.

Papageorgopoulos, C. A. and Jaegermann, W. (1995). Li intercalation across and along the van der Waals surfaces of $MoS_2(0001)$. **Surf. Sci.** 338: 83.

Park, J. W., Bogorin, D., Cen, C., Felker, D., Zhang, Y., Nelson, C., Bark, C., Folkman, C., Pan, X., Rzchowski, M., Levy, J., and Eom, C. (2010). Creation of a two-dimensional electron gas at an oxide interface on silicon. **Nat. Commun.** 1: 94.

Perdew, J. P., Burke, K., and Ernzerhof, M. (1996). Generalized gradient approximation made simple. **Phys. Rev. Lett.** 77: 3865.

Pesin, D. and Balents, L. (2010). Mott physics and band topology in materials with strong spin-orbit interaction. **Nature Phys.** 6: 376.

Ponomarenko, L. A., Schedin, F., Katsnelson, M. I., Yang, R., Hill, E. H., Novoselov, K. S., and Geim, A. K. (2008). Chaotic Dirac billiard in graphene quantum dots. **Science** 320: 356.

Radhakrishnan, K. and Pilla, M. (2008). Semiconducting properties of $HfSe_2$ single crystals grown by CVT technique. **AIP Conf. Proc.** 1004: 283.

Radisavljevic, B., Radenovic, A., Brivio, J., Giacometti, V., and Kis, A. (2011). Single-layer MoS_2 transistors. **Nat. Nanotechnol.** 6: 147.

Ramirez, A. P., Subramanian, M. A., Gardel, M., Blumberg, G., Li, D., Vogt, T., and Shapiro, S. M. (2000). Giant dielectric constant response in a copper-titanate. **Solid State Commun.** 115: 217.

Reshak, A. H. and Auluck, S. (2005). Ab initio calculations of the electronic and optical properties of $1T$-HfX_2 compounds. **Physica B** 363: 25.

Ridley, B. K. (1999). **Quantum processes in semiconductors**. Oxford: Clarendon Press.

Riedl, C., Coletti, C., Iwasaki, T., Zakharov, A. A., and Starke, U. (2009). Quasi-free-standing epitaxial graphene on SiC obtained by hydrogen intercalation. **Phys. Rev. Lett.** 103: 246804.

Riley, J. M., Mazzola, F., Dendzik, M., Michiardi, M., Takayama, T., Bawden, L., Granerød, C., Leandersson, M., Balasubramanian, T., Hoesch, M., Kim,

T. K., Takagi, H., Meevasana, W., Hofmann, P., Bahramy, M. S., Wells, J. W., and King, P. D. C. (2014). Direct observation of spin-polarized bulk bands in an inversion-symmetric semiconductor. **Nature Phys.** 10: 835.

Riley, J. M., Meevasana, W., Bawden, L., Asakawa, M., Takayama, T., Eknapakul, T., Kim, T. K., Hoesch, M., Mo, S.-K., Takagi, H., Sasagawa, T., Bahramy, M. S., and King, P. D. C. (2015). Negative electronic compressibility and tunable spin splitting in WSe_2. **Nat. Nanotechnol.**: doi:10.1038/nnano.2015.217.

Rosencher, E. and Vinter, B. (2002). **Optoelectronics**. Cambridge University Press.

Rossnagel, K. (2010). Suppression and emergence of charge-density waves at the surfaces of layered 1T-TiSe$_2$ and 1T-TaS$_2$ by *in situ* Rb deposition. **New J. Phys.** 12: 125018.

Rouxel, J. (1979). **Physics and Chemistry of compounds with layered structures**. Dordrecht, Netherlands: Reidel Publishing Company.

Schiebold, E. (1932). **Die Laue Methode**. Leipzig.

Schottky, W. (1938). Halbleitertheorie der Sperrschicht. **Naturwissenschaften** 26: 843.

Schulz, H. J. (1995). Fermi liquids and non-Fermi liquids. **arXiv:cond-mat.**: 9503150v2.

Seah, M. P. and Dench, W. A. (1979). Quantitative electron spectroscopy of surfaces: A standard database for electron inelastic mean free paths in solds. **Surf. Interface Anal.** 1: 2.

Sinclair, D. C., Adams, T. B., Morrison, F. D., and West, A. R. (2002). $CaCu_3Ti_4O_{12}$: One-step internal barrier layer capacitor. **Appl. Phys. Lett.** 80: 2153.

Somoano, R. B., Hadek, V., and Rembaum, A. (1973). Alkali metal intercalates of molybdenum disulfide. **J. Chem. Phys.** 58: 697.

Sorokin, A. A., Bobashev, S. V., Feigl, T., Tiedtke, K., Wabnitz, H., and Richter, M. (2007). Photoelectric effect at ultrahigh intensities. **Phys. Rev. Lett.** 99: 213002.

Splendiani, A., Sun, L., Zhang, Y., Li, T., Kim, J., Chim, C.-Y., Galli, G., and Wang, F. (2010). Emerging photoluminescence in monolayer MoS_2. **Nano Lett.** 10: 1271.

Srivastava, A., Sidier, M., Allain, A. V., Lembke, D. S., Kis, A., and Imamoğlu, A. (2015). Valley Zeeman effect in elementary optical excitations of monolayer WSe_2. **Nature Phys.** 11: 141.

Takesada, M., Yagi, T., Itoh, M., and Koshihara, S. (2003). A gigantic photoinduced dielectric constant of quantum paraelectric perovskite oxides observed under a weak DC electric field. **J. Phys. Soc. Jpn.** 72: 37.

Thongbai, P., Yamwong, T., and Maensiri, S. (2009). Electrical responses in high permitivity dielectric (Li, Fe)-doped NiO ceramics. **Appl. Phys. Lett.** 94: 62904.

Varykhalov, A., Sánchez-Barriga, J., Shikin, A. M., Biswas, C., Vescovo, E., Rybkin, A., Marchenko, D., and Rader, O. (2008). Electronic and magnetic properties of quasifreestanding graphene on Ni. **Phys. Rev. Lett.** 101: 157601.

Von Helmolt, R., Wecker, J., Holzapfel, B., Schultz, L., and Samwer, K. (1993). Giant negative magnetoresistance in perovskitelike $La_{2/3}Ba_{1/3}MnO_x$ ferromagnetic films. **Phys. Rev. Lett.** 71: 2331.

Von Klitzing, K. (1985). **The quantized Hall effect**. Nobel lecture.

Wang, H., Liu, F., Fu, W., Fang, Z., Zhou, W., and Liu, Z. (2014). Two-dimensional heterostructures: fabrication, characterization, and application. **Nanoscale** 6: 12250.

Wang, Q. H., Kalantar-Zadeh, K., Kis, A., Coleman, J. N., and Strano, M. S. (2012). Electronics and optoelectronics of two-dimensional transition metal dichalcogenides. **Nat. Nanotechnol.** 7: 699.

Wang, X., Zhi, L., and Mullen, K. (2008). Transparent, conductive graphene electrodes for dye-sensitized solar cells. **Nano Lett.** 8: 323.

Wi, S., Kim, H., Chen, M., Nam, H., Jay Guo, L., Meyhofer, E., and Liang, X. (2014). Enhancement of photovoltaic response in multilayer MoS_2 induced by plasma doping. **ACS nano** 8: 5270.

Wilson, J. A. and Yoffe, A. D. (1969). The transition metal dichalcogenides discussion and interpretation of the observed optical, electrical and structural properties. **Adv. Phys.** 18: 193.

Woolam, J. A. and Somoano, R. B. (1976). Superconducting critical fields of alkali and alkaline-earth intercalates of MoS_2. **Phys. Rev. B** 13: 3843.

Xia, F., Wang, H., Xiao, D., Dubey, M., and Ramasubramaniam, A. (2014). Two-dimensional material nanophotonics. **Nature Photon.** 8: 899.

Xiao, D., Liu, G.-B., Feng, W., Xu, X., and Yao, W. (2012). Coupled spin and valley Physics in monolayers of MoS_2 and other group-VI dichalcogenides. **Phys. Rev. Lett.** 108: 196802.

Xing, J., Zhao, K., Lu, H. B., Wang, X., Liu, G. Z., Jin, K. J., He, M., Wang, C. C., and Yang, G. Z. (2007). Visible-blind, ultraviolet-sensitive photodetector based on $SrTiO_3$ single crystal. **Opt. Lett.** 32: 2526.

Ye, J. T., Zhang, Y. J., Akashi, R., Bahramy, M. S., Arita, R., and Iwasa, Y. (2012). Superconducting dome in a gate-tuned band insulator. **Science** 338: 1193.

Yoo, E., Kim, J., Hosono, E., Zhou, H., Kudo, T., and Honma, I. (2008). Large reversible Li storage of graphene nanosheet families for use in rechargable lithium ion batteries. **Nano Lett.** 8: 2277.

Yoon, Y., Ganapathi, K., and Salahuddin, S. (2011). How good can monolayer MoS_2 transistor be? **Nano Lett.** 11: 3768.

Zeng, H., Dai, J., Yao, W., Xiao, D., and Cui, X. (2012). Valley polarization in MoS_2 monolayers by optical pumping. **Nat. Nanotechnol.** 7: 490.

Zhang, K. H. L., Egdell, R. G., Offi, F., Lacobucci, S., Petaccia, L., Gorovikov, S., and King, P. D. C. (2013). Microscopic origin of electron accumulation in In_2O_3. **Phys. Rev. Lett.** 110: 056803.

Zhang, W. (2014). Voltage-driven spintronic logic gates in graphene nanoribbons. **Sci. rep.** 4: 6320.

Zhang, W., Huang, Z., and Zhang, W. (2014a). Two dimensional semiconductors with possible high room temperature mobility. **arXiv**: 1403.3872v1.

Zhang, X., Liu, Q., Luo, J. W., Freeman, A. J., and Zunger, A. (2014b). Hidden spin polarization in inversion-symmtric bulk crystals. **Nature Phys.** 10: 130.

Zhang, Y., Chang, T. R., Zhou, B., Cui, Y.-T., Yan, H., Liu, Z., Schmitt, F., Lee, J., Moore, R., Chen, Y., Lin, H., Jeng, H.-T., Mo, S.-K., Hussain, Z., Bansil, A., and Shen, Z.-X. (2014c). Direct observation of the transition from indirect to direct bandgap in atomically thin epitaxial MoSe$_2$. **Nat. Nanotechnol.** 9: 111.

Zhang, Y., Ye, J., Matsuhashi, Y., and Iwasa, Y. (2012). Ambipolar MoS$_2$ thin flake transistors. **Nano Lett.** 12: 1136.

Zhang, Z. and Yates, J. T. (2012). Band bending in semiconductors: chemical and physical consequences at surfaces and interfaces. **Chem. Rev.** 112: 5520.

Zhou, S. Y., Gweon, G. H., Fedorov, A. V., First, P. N., de Heer, W. A., Lee, D. H., Guinea, F., Castro Neto, A. H., and Lanzara, A. (2007). Substrate-induced bandgap opening in epitaxial graphene. **Nat. Mater.** 6: 770.

Zhou, X. J., Wannberg, B., Yang, W. L., Brouet, V., Sun, Z., Douglas, J. F., Dessau, D., Hussain, Z., and Shen, Z.-X. (2005). Space charge effect and mirror charge effect in photoemission spectroscopy. **J. Electron. Spectrosc. Relat. Phenom.** 142: 27.

Zhu, Z. Y., Cheng, Y. C., and Schwingenschlögl, U. (2011). Giant spin-orbit-induced spin spitting in two-dimensional transition-metal dichalcogenide semiconductors. **Phys. Rev. B** 84: 153402.

Zong, X., Yan, H., Wu, G., Ma, G., Wen, F., Wang, L., and Li. (2008). Enhancement of Photocatalytic H$_2$ Evolution on CdS by Loading MoS$_2$

as Cocatalyst under Visible Light Irradiation. **J. Am. Chem. Soc.** 130: 7176.
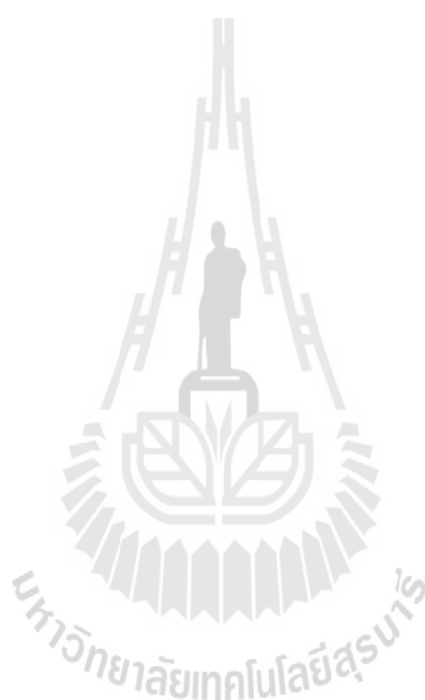
APPENDICES

APPENDIX A

EXPERIMENTAL AND CALCULATION

DETAILS

Some values obtained from ARPES such as electron-phonon coupling (kink), spin-orbit splitting, and band splitting can be measured directly from the experiment. However, we need to have a powerful method to extract these essential value quantitatively. In ARPES, the photoelectron intensity will be varied by their binding energies or elements. In principle, the peaks distribution have always been derived from Lorentzian and Fermi function while other regions such as core-levels are derived in different ways. In this chapter, I would like to express some analysis used for extracting the experimental value in our experiment. The calculation part is based on DFT calculation, the reliable tool to understand the electronic structure. The details of the calculation have been done by my coauthor and discussed extensively in this chapter. In the second part, band structure variations after disturbing the system have been studied and performed.

A.1 Extracted value from the experimental data

The quantitative values from our data are mostly extracted by fitting. The photoemission intensity is generally taken the form of, $I_{ARPES} = [Lorentzian + Fermi] + background$. However, the region near the Fermi energy could be simplified by using only the Lorentzian function. The constant momentum dispersion (MDC) and energy dispersion (EDC) are general collectible and very useful data

obtained from ARPES. Lorentzian function has general formula of

$$f(x) = y_0 + \frac{A}{(x - x_0)^2 + B} \tag{A.1}$$

where x_0 is the center of the peak and B is normally used to describe the full width at half maximum (FWHM). We typically use the high-order polynomial to track the lineshape of data in low-energy region. However, in high range of energy measurement like XPS, required Shirley background to obtain the good fitting. There are some important values need to be mentioned about how to take them from the ARPES. Firstly, the carrier effective masses which generally be extracted at the Fermi pocket or VBM. The effective masses carry the information about the electron mobility by this equation

$$\mu = \frac{q}{m^*} \bar{\tau} \tag{A.2}$$

where $\bar{\tau}$ is the average scattering time, the electron mobility (μ) is inverse proportional to the effective masses (m^*). This has been used to describe the quasiparticle term in electron interacting system. There are two steps to track the band dispersion in this region. Firstly, EDC at each fixed energy has to be fitted by the Lorentzian function which will give us a peak position for any constant momentum. After the single peak has been obtained from EDC, then we have to do linefit continuously over the whole regions of interest. The second step, we have to exploit the parabolic equation to fit among the peaks collected from EDCs. The band dispersion peaks (at VBM or CDM) always behaves like parabola band (in 2DEG system) which are obviously fit through the parabolic equation. The comparison between parabolic equation and nearly-free electron can be expressed as

$$E = \frac{\hbar^2 k^2}{2m^*}$$

$$y = mx^2 \tag{A.3}$$

The crucial value observed in our MoS_2 is the splitting in energy (ΔE) at VBM along $\bar{K}$ point. We extract the corresponding EDCs by fitting this splitting state with two Lorentzian curves and second-order polynomial background. As shown in figure A.1 (c) and (d), the splittings in energy (peak to peak) for the pristine cleaved-surface and a potassium dosed-surface can be extracted to be 170 ± 12 and 176 ± 12 meV, respectively.

Moreover, we have calculated the amount of potassium to be dosed to the MoS_2 by XPS technique. The long energy range covered Mo-4p and K-3p peaks (using photon energy 100 eV) have been preformed. Lorentzian function with Shirley background have been used to fit both of the peaks (Mo-4p and K-3p). The peaks have been weighted and normalized by standard data book which provides a relative intensity of each peaks. By this process, the concentration of potassium covered on MoS_2 surfaces are approximately around 0.06 atoms per unit cell at the 900 seconds of potassium dosing.

A.2   Details of calculation (extension)

Remarks: this part has been done by my coauthor. This section is extended from the discussion in chapter 5. To understand the process of our measurement, the possible model calculations have been provided. The calculations were performed based on the density functional theory as implemented in the VASP code (Kresse and Furthmüller, 1996), within the Perdew, Burke, and Erzenhoff (PBE) (Perdew et al., 1996) functional form of the generalized gradient ap-
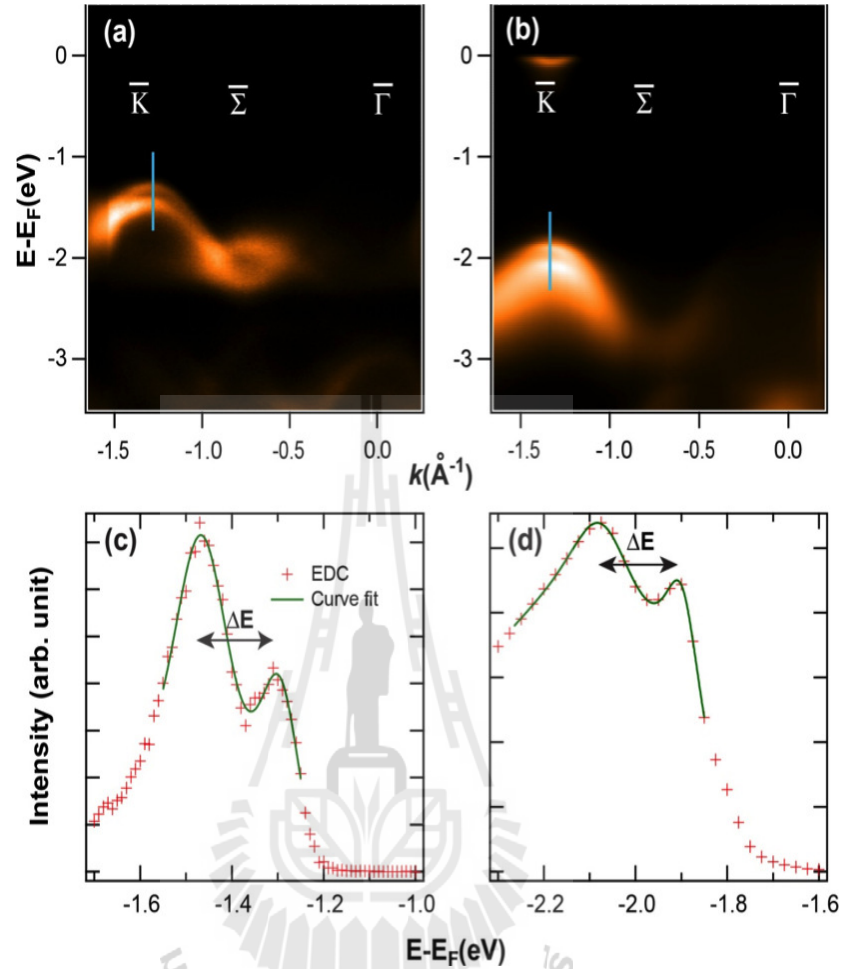
Figure A.1 (a,b) Valence band electronic structure measured along the $\bar{\Gamma}$-$\bar{K}$ direction for the pristine cleaved-surface and a potassium dosed-surface, respectively. The vertical blue lines at the $\bar{K}$ point of (a) and (b) are the EDCs which are taken for extracting spin-orbit energy splitting shown in panel (c) and (d).

proximation (GGA) and the projector augmented wave (PAW) potentials (Blöchl, 1994). The cutoff energy of the plane wave expansion is 600 eV. The Γ-centered Monkhorst-Pack k-mesh of 24×24×5 is used for Brillouin zone integrations. The parameters of dispersion energy correction to van der Waals interactions of layered structure are considered within DFT+D2 approach of Grimme (Grimme, 2006).

Structural relaxation is performed until the force on each ion is below 0.01 eV/$\mathring{A}$. The optimized lattice parameter a and c/a ratio for bulk MoS_2 are 3.189 $\mathring{A}$ and 3.893 which are in good agreement with known experimental value (3.160 $\mathring{A}$ and 3.891 (Somoano et al., 1973)). The conduction bands of bulk MoS_2 have been previously shown in figure 5.1 (c). The effects of electron dosing on MoS_2 electronic structures have been investigated by computing the electronic structures of MoS_2 at different c/a ratio (other structural parameters are taken from relaxation calculation) with 0.04 electron introduced to bulk MoS_2 system. The calculated band structures are shown in Fig 5.8. Many calculated models have been performed. Even most of the calculation are not correct in our system, but after several tries, we gain a lot of information and ideas to improve our calculation. This is led to our accomplished model to describe the exact role in our system.

A.2.1 Layered dependent effect on MoS_2 electronic structure

In this part, the number of layered dependent calculations of MoS_2 have been performed which are good agreement with other calculation (Ellis et al., 2011) (not shown). The shape and energy shifts in MoS_2 band structure have been found apparently. The band structure variation is supposed to be occurred if the number of layer is changed. Our calculated bulk- and bilayer-band structures of MoS_2 are indirect band gap which have the valence band maximum at $\bar{\Gamma}$ point and the conduction band minimum at $\bar{K}$ point. However, only the calculation of MoS_2 monolayer shows the nature of direct band gap which both VBM and CBM located at $\bar{K}$. Our calculation is in agreement with the previous calculation and the experiment confirming the right calculation approach (Ellis et al., 2011; Mak et al., 2010). The direct band gap semiconductor is necessary to improve

the photoluminescence efficiency. For example, in optoelectronics, electrons can be excited effortlessly to the conduction band using only incident photon without momentum (phonon required). So, this dramatically changes of band gap properties could make MoS_2 very interesting for optoelectronic application.

As mentioned before, The effect of potassium evaporated-MoS_2 can be happened in many different ways. Here, by exploiting DFT calculation. The crucial understanding of how potassium interacting with the MoS_2 can be performed. In this section, possible processes of potassium interacted with our system were speculated. Three models including: bulk dosing model, surface dosing model, and c-axis expansion model have been presented.

A.2.2 Electronic structure of various amount of potassium dosing into bulk MoS_2

The bulk potassium dosing was a very first and common model that we performed in the calculation. The bulk MoS_2 is likely to be dosed after potassium evaporation. In this circumstance, the sample surfaces must be covered and interacted with potassium. Because potassium is very reactive, some of them is reacted with the MoS_2 led to the impurities. This is well know as a structural or bulk dosing. Here, we demonstrate the calculation as a function of potassium dosing concentration shown in figure A.2. The potassium concentration ranging from 0, 50 and 100 % have been calculated according to the maximum of two potassium atoms per unit cell to be dosed into the MoS_2 without destroying the original structure of host material. This calculation shows the changing of the electronic structure of MoS_2 after potassium dosing. The knowledge gained from potassium or other alkali metal dosings can shift the E_F towards the conduction band (as n-type semiconductor) in the system. From the calculation, the conduction band
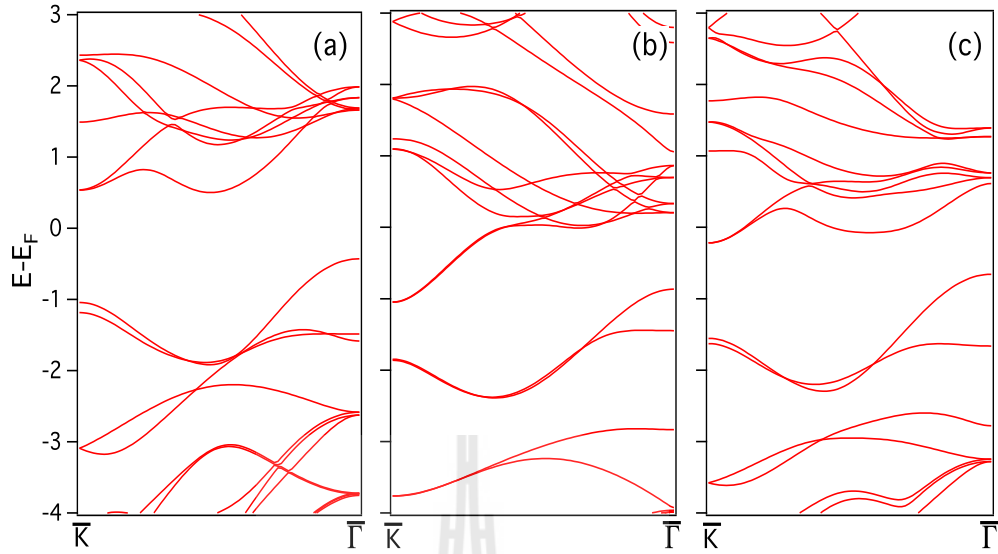
Figure A.2 The calculated bulk band structure performing by DFT calculation a) bulk MoS_2, b) one atom, and c) two atoms of potassium in bulk of MoS_2. Note that the maximum of two potassium atoms added per unit cell will not destroy the original structure of MoS_2.

can be revealed after 50 % dosing and CBM is moved from $\bar{\Gamma}$ to $\bar{K}$ of the brillouin zone. In addition, after adding more potassium concentration, the CBM at $\bar{K}$ is lower, while the VBM at $\bar{\Gamma}$ is going higher. This can be implied that this type of calculation is corrected only half of our measurement.

A.2.3   Electronic structure of different types of potassium surface dosing on MoS_2

In this section, I would like to introduce the surface dosing which is more reliable in layered TMDs. In this model, after potassium evaporation, the potassium atoms have not been expected to enter the bulk but have to locate only near surface of the sample. To simulate this system, the four layers of MoS_2 have been

introduced with an infinite vacuum level. There are two possible effects which can be happened if potassium atoms are located near the surface. Firstly, the potassium intercalation, potassium atoms are penetrated into the deeper layer of MoS_2 rather than located on the surfaces. In the other hand, if the potassium atoms are accumulated on the top of MoS_2, this effect is called as "potassium surface adsorption". Figure A.3 (a) shows the band structure of one potassium atom intercalated on MoS_2 surface. In this case, more bands derived from potassium orbitals have been revealed in this calculation (compared to figure A.2 (a)). The band structure variation have also been observed in this model implying the role of potassium intercalated-system. The potassium adsorption model, as well as co-adsorption and intercalation provide the potassium bands across band gap (shown in figure A.3 (b) and (c), respectively). These crossed-bands can not be observed our the experiment. The non-potassium adsorption in our system is then being concluded by this evidence.

A.2.4   Electronic structure of c-axis expansion of MoS_2

From the literature, some alkali metal intercalated into layered TMDs would expand the layer spacing (c-axis) in this materials (Fujimori et al., 1988). By this reason, the calculated band structures of MoS_2 in various c-axis spacing have been taking into account. This calculation were performed to understand our potassium intercalated system which have been previously shown in figure 5.2 (a). The c/a ratios from 3.893 (optimum) to 5.893 (maximum) have been studied with the optimizing electrons (referred to the number of potassium atoms) filling between expanded layers. The calculated band structures have been shown recently in figure 5.8. By expanding the c/a ratios, two effects of decreasing energy splitting at $\bar{K}$ point and band shifted up at $\bar{\Sigma}$ are pronounced. By this model,
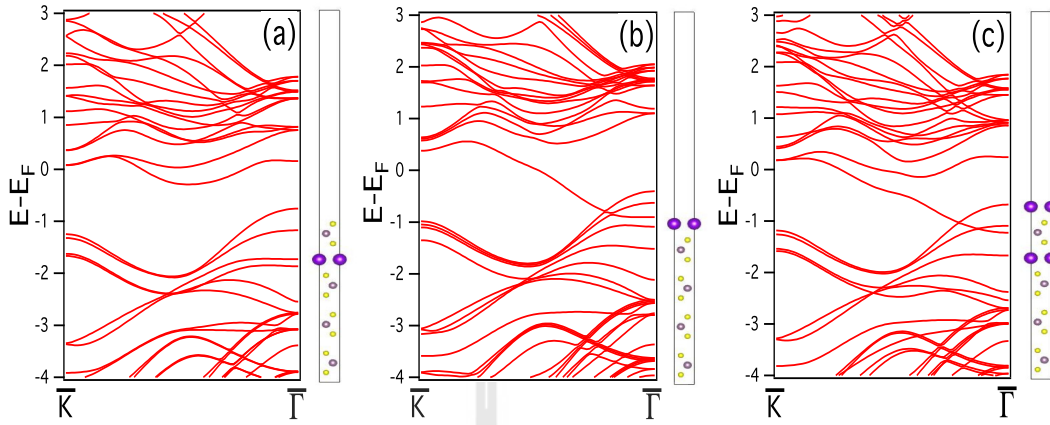
Figure A.3 The calculated band structure induced by various kind of dosing a) intercalation model, b) adsorption and model c) co-intercalation and adsorption model. The four layers of MoS_2 contacting with infinite vacuum level have been determined as a reference electronic structure near the surface.

we have finally obtained the very quantitative agreement result between the calculation and our experimental data (figure 5.8 (d)). The c/a ratio of 4.893 is very similar to the value of MoS_2 monolayer. Hence, this calculation may be used to explain the monolayer like behaviour in our potassium intercalated-system.

A.2.5 Full formation energy calculation

From the c/a calculation in section A.2.4, the results are strongly indicated that potassium atoms are not adsorbed at the surface of MoS_2. To clarify this assumption, extending from section 5.2.1, we have performed the formation energy (E_{form}) calculation giving the possible state in our system. Figure A.4 demonstrates the E_{form} obtained from various models including potassium adsorption and layer intercalation (1st and 2nd referred to the layer position originated from

the surface). In this figure, the potassium favourable can be calculated from the E_{form}. E_{form} refers to the forming possibility to a new bonding. Once again, the probability of new bonding is high if it has lower E_{form}. In case of E_{form} lower than 0, the initial potassium bonding is likely to be destroyed to form a new bonding. The system required curtain amount of E_{form} to break the potassium bonding from the source. Hence, higher formation energy is used to break the bond breaking energy from different potassium source (i. e. atoms or molecules). From the calculation, all cases of adsorption and intercalation give the formation energy lower than 0 (at different bond breaking energy). This refers to the interaction between potassium and MoS_2. Additionally, all cases of intercalation, especially in the $1^{st} + 2^{nd}$ and $2\times$ 1st layer intercalation show the lower E_{form} than other model. This can be implied that potassium is likely to be intercalated to the lower layer of MoS_2. In conclusion, our assumption of potassium intercalation has been claimed by our calculation approaches; the c/a expansion model and potassium favourable.
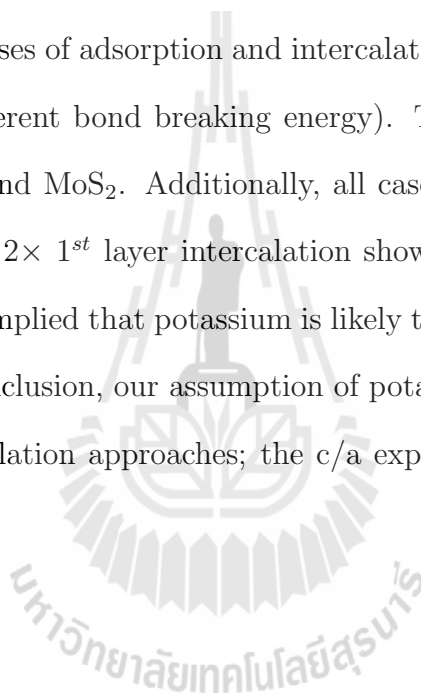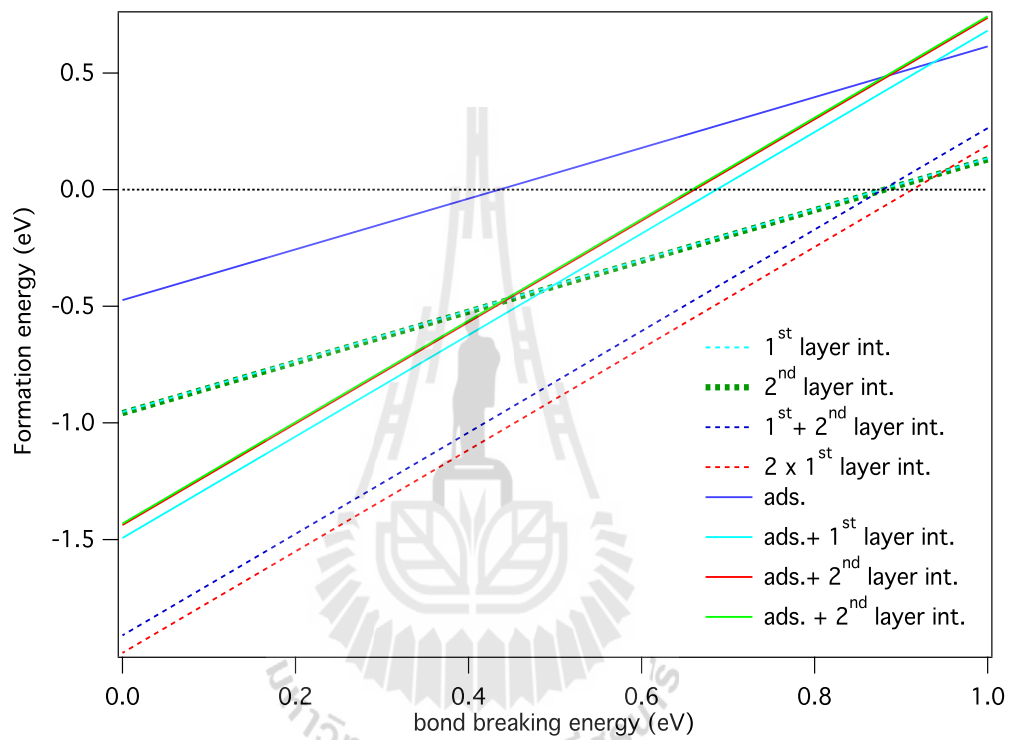
Figure A.4 Formation energy which is calculated from various potassium inter-
acted models on the MoS_2 surfaces. The intercalation processes show a lower
formation energy than adsorption model. This implies that potassium is likely to
be intercalated to the surface rather than adsorbed on the MoS_2 surfaces.

APPENDIX B

OTHER PUBLISHED WORKS

ARPES is used to study the electronic structure of material. This microscopic scale measurement is used to understand the fundamental properties such as electron-phonon, spin-orbit interaction as well as the novel properties through electronic structure. applying the fundamental knowledge to the macroscopic study or application is very challenging. In this part, I would like to present our accomplished work originating from our ARPES study into a macroscopic scale. The enhancement of dielectric constant in $CaCu_3Ti_4O_{12}$ as well as the possibility of transparent light sensor application are represented.

B.1 Anomalous change in dielectric constant of $CaCu_3Ti_4O_{12}$ under violet-to-ultraviolet irradiation

This work has been published recently with me as a coauthor contributed in experimental section including capacitance and photoemission measurement (Masingboon et al., 2013). The perovskite like $CaCu_3Ti_4O_{12}$ (CCTO) is a Ba/Pb-free material which exhibits giant dielectric constants and good thermal stability. CCTO is not ferroelectric but still exhibits a giant dielectric constant in the kilohertz region $\sim 10^4 - 10^5$ (Ramirez et al., 2000). Moreover, it does not undergo any structural phase transitions over a wide temperature range from -173 - 327 ^{o}C, where it maintains its large dielectric constant (Ramirez et al., 2000). Several models, such as the internal-barrier-layer-capacitor model (Sinclair et al., 2002) and the twin or sub-grain model (Fang et al., 2006), have been employed to ex-

plain the giant response in CCTO, and while a full microscopic understanding remains elusive, it is generally thought to be an extrinsic effect related to some form of insulating boundary (Lunkenheimer et al., 2002). The ability to control the electrical property of these insulating boundaries is therefore crucial to modify and enhance the dielectric constant.

Indeed, many studies of polycrystalline samples have already focused on varying the structure of grains and boundaries (for example, by changing calcination temperature (Li et al., 2011b)). Here, we adopt a different approach using light irradiation of polycrystalline CCTO to dynamically tune its dielectric properties. Such light irradiation has previously been used to induce a large enhancement in the dielectric constant of $SrTiO_3$ and $KTaO_3$ at temperatures below 100 K (Takesada et al., 2003; Hasegawa et al., 2003), reportedly occurring due to small polaron formation with photo-excited carriers in the quantum paraelectric phase of these compounds. In this work, we observed a striking light-induced enhancement of the dielectric constant in CCTO. This is pronounced even at room temperature, promising applications in light sensitive electronic devices. We combine spectroscopic and transport measurements performed under different atmospheric conditions to identify the microscopic origin of the capacitance enhancement in this system.

B.1.1 Experimental setup

We fabricated a capacitor with a central CCTO dielectric and a copper back electrode. The front electrode was made of transparent and conductive indium tin oxide (ITO) which was mechanically compressed against the CCTO layer (see the diagram in figure B.1 (c)). The capacitance was then measured using an impedance analyzer outputting an alternating voltage at a frequency (f) of 1 kHz - 100 kHz.

The CCTO surface was then exposed to violet light from a 405 nm laser through the front (i.e. transparent) electrode. The light intensity was set at 0.2 W/cm^2, and the beam profile was circular with a diameter around 4 mm. This photon energy of 3.06 eV (i.e. 405 nm in wavelength) was chosen to be below the optical band gap of ITO (around 4 eV); hence, most of the light would be transmitted by the top ITO electrode. Additionally, as most materials have work functions above 4 eV, this photon energy of 3.06 eV would not be expected to create photoelectrons, which might artificially affect our measured dielectric constants.

B.1.2 Capacitance measurement

Figure B.1 (a) shows the measured capacitance and loss tangent of the CCTO dielectric at 1 kHz. We observed a striking increase of up to 22 % in the capacitance measured with f = 1 kHz and 10 kHz under laser light illumination (shown in figure B.1 (b)). In both cases, the capacitance smoothly increased and then saturated after approximately 200 s. When the light was switched off, the capacitance decayed back to the original value with a relatively long time constant of 2 - 3 min. This same behaviour could be repeated through many cycles of light illumination. We observed a decreasing relative change in the saturated capacitance with frequency, even becoming negative for frequencies of f = 100 kHz. The maximum enhancement of the capacitance shows a dependence on the intensity of the light illumination in our measurement. Moreover, this suggests that a threshold intensity should be reached before changes in the dielectric constant start to occur, indicative of a chemical change rather than a purely electronic (such as photo doping) origin of the enhanced capacitance, consistent with our discussions below. These observations already suggest application of CCTO in light sensitive tuneable capacitance devices.
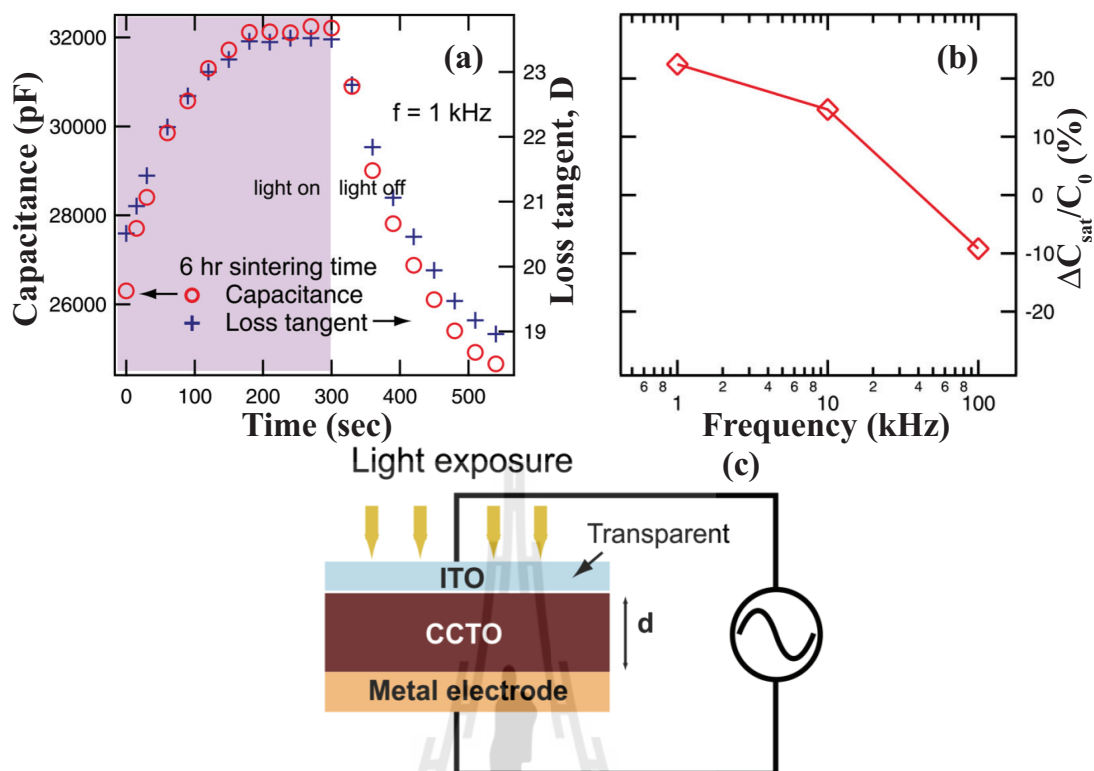
Figure B.1 (a) Measured capacitance and loss tangent at frequency of 1 kHz as a function of light exposure time, of CCTO dielectric materials with sintering time of 6 h. (b) The summary of the percentage changes in capacitance at saturation upon the light exposure for all the frequency inputs. c) The diagram of capacitance measurement with CCTO as dielectric material where the light exposure can go through the top transparent gate (Masingboon et al., 2013).

B.1.3   Photoemission and resistance measurement

In this section, we attempt to uncover the microscopic mechanism that drives the capacitance enhanement effect. Firstly, we measured the evolution of the electronic structure of the CCTO samples upon illumination using PES. As shown in figure B.2 (a), the photoemission spectra of the freshly-fractured-sample shows a valence band characteristic of occupied O_{2p} states at a binding energy
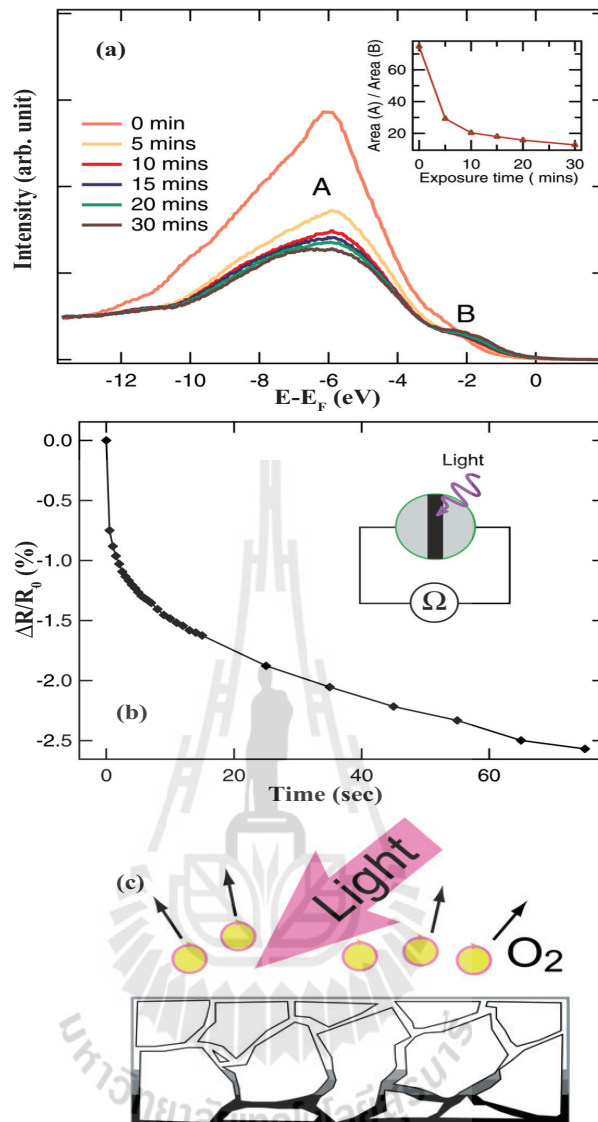
Figure B.2 a) Evolution of VB of a CCTO ceramic from the pristine- to the UV irradiated-surface. Inset shows the ratio between areas of region A and region B as a function of time. b) The time dependence of the CCTO resistance upon exposure to synchrotron light at 2.02×10^{-7} millibar. c) Schematic diagram of oxygen vacancy rich surface during UV exposure at low pressure (Masingboon et al., 2013).

of around 4 - 8 eV. In addition, a small shoulder (marked in figure B.2 (a) as peak B) is observed above the valence band edge, within the band gap. With

increased exposure to the intense 60 eV synchrotron light, the PES spectra showed a large depletion of spectral weight from the O_{2p} states (region A), accompanied by an increased weight of the in-gap state (region B). This decrease in relative weight of the A and B peaks with increasing exposure time is shown inset to figure B.2 (a). We performed transport measurements in vacuum as a function of UV light exposure. To enable this, we fabricated two silver electrodes with a 1 mm-wide bare surface region in between to be exposed to the incident light (see inset of figure B2 (b)). At atmospheric pressure, the measured resistance was approximately 160 kΩ. This dropped to 128 kΩ when the sample was held at a pressure of 5×10^{-8} millibar, already suggesting some potential oxygen loss in vacuum. Moreover, as shown in figure B.2 (b), upon UV light exposure, the resistance showed an initial rapid decrease, followed by a slower decrease with increasing exposure time (corresponding to increased integrated irradiation dose), reaching a decrease of around 2.5 % after 1 h. This increase in conductivity agrees well with the development of oxygen vacancy-induced-states observed in the photoemission, which should induce metallicity at the sample surface via the chemical reaction O (neutral)$\rightarrow V_0^{++}$ (oxygen vacancy)$+ 2e^- + \frac{1}{2}O_2$ (Fang et al., 2004). Such oxygen vacancy creation has previously been suggested to occur upon light irradiation in other oxides such as $SrTiO_3$ (Meevasana et al., 2011) and ZnO (Liqiang et al., 2006). The similarity in the functional form of the resistivity change and the change in relative spectral weight observed in the photoemission (inset of figure B.2 (a)) strongly suggests that this oxygen vacancy creation is occurring here and driving surface metallicity, while the slightly more rapid initial onset in the resistive measurements is consistent with the higher light intensity used than during photoemission.

B.1.4   Oxygen vacancy recovery and conclusion

To confirm the hypothesis of oxygen vacancy recovery, we monitored the evolution of the resistance, following light irradiation, while the sample was held in different oxygen partial pressures, as shown in figure B.3 (a). While the reduced resistance induced by light illumination remained fairly stable when the sample was held in vacuum conditions, it showed an increasingly-rapid-increase with increasing oxygen partial pressure, entirely consistent with the filling of near-surface oxygen vacancies. The similar rate of resistance recovery for the sample held at the highest partial pressure to the rate of decay of the capacitance back to its original value following light illumination (figure B.1 (a)) suggests an intimate link between the oxygen vacancy-induced conductivity in CCTO and the dramatic enhancement of its capacitance. A control experiment using similar pressures of Ar revealed negligible resistance recovery. We note that a similar healing of surface oxygen vacancies by exposure to O_2 gas was also recently demonstrated to reduce surface metallically in In_2O_3 (Zhang et al., 2013). As shown schematically in figure B.2 (c), oxygen vacancies induced by irradiation could make some parts of these insulating boundaries become conducting, hence reducing their thickness and enhancing their capacitance. This may be further mediated by oxygen vacancy creation near the sample surface metalising this region. Healing such vacancies with oxygen exposure would result in a return to the original measured capacitance, consistent with our experiment (figure B.3 (b)). In summary, we have found pronounced changes in capacitance when a CCTO dielectric material is exposed to intense violet light. Both measurements of electronic structure and conductivity point to a significant role of oxygen vacancies, induced by the light exposure. Moreover, our observations suggest an exciting route for dramatically and reversibly altering the electrical and dielectric properties of CCTO using light exposure, which may

be used for in light-sensitive electronic devices.
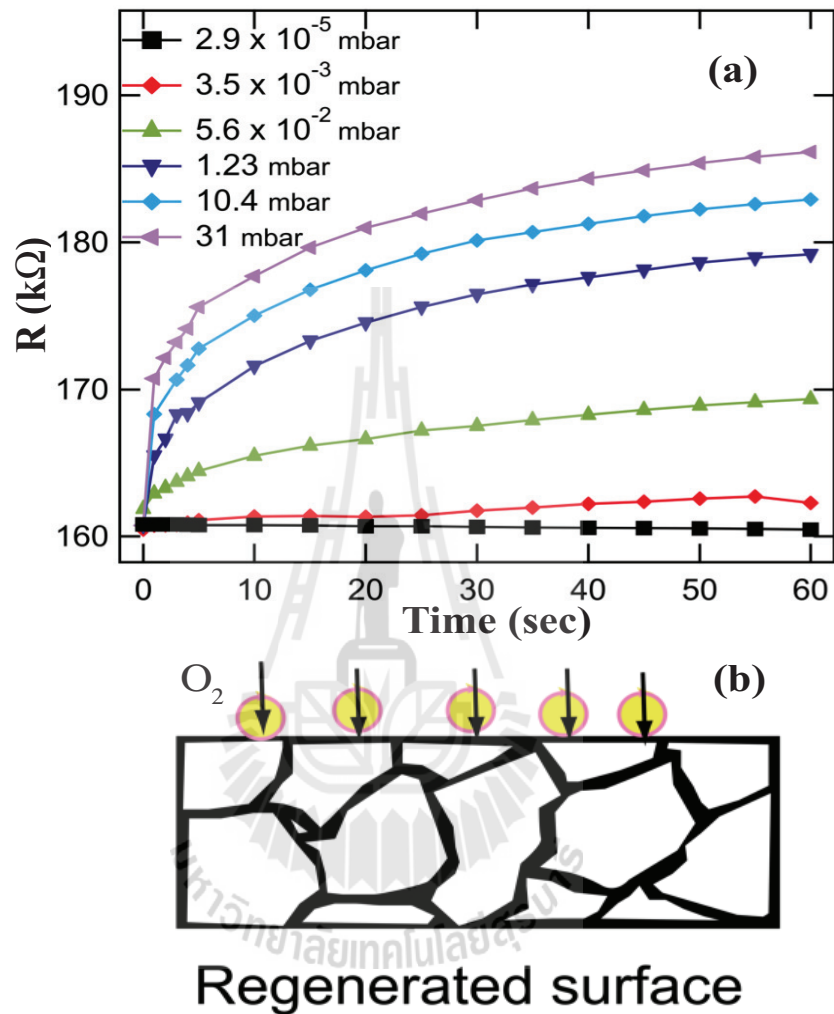
Figure B.3 a) The time dependence of the CCTO resistance at oxygen pressures between 2.9×10^{-5} and 31 millibar. b) Schematic diagram of regenerated oxygen vacancy at the surface which may result to the resistance recovery (Masingboon et al., 2013).

B.2 Resistivity change in $SrTiO_3$ upon irradiation and its application in light sensing

In our previous ARPES study, we realize that the 2DEG can be created at the surfaces of the perovskite materials such as $SrTiO_3$ and $KTaO_3$ by light irradiation (Meevasana et al., 2011; King et al., 2012). This effect occurs because of the electron accumulation at the surface which makes the surface of these materials becoming more conducting. The $SrTiO_3$ which has a large band gap around 3.2 eV and transparent is a good candidate to be a new type of light sensing. This kind of light sensor is expected to be replaced the opaque commercial light sensing made from small band gap semiconductor (e.g. CdSe, CdS) in new functional applications.

B.2.1 sample preparation and experimental setup

In this work, I am a coauthor contributing in sample preparation and resistance measurement. The $SrTiO_3$ samples measured in the work (Crystal Base Co., Japan) were single crystals with (100) crystal orientation and $5 \times 5 \times 0.5$ mm^3 in dimension. The samples were cleaned and then gold electrode patterns were created on the sample's surfaces by using a DC sputtering coater. The $SrTiO_3$ surface was covered with gold films except in the middle part whose width was around 147 μm. This middle area of the $SrTiO_3$ surface, which was initially insulating without any excitation, would later be exposed to various types of irradiation, including a violet laser (405 nm), green laser (530 nm), red laser (650 nm), ultraviolet light emitting diode (LED), deuterium lamp (Ocean Optics DH-2000, Ocean Optics Inc., Dunedin, FL, USA), halogen lamp (Ocean Optics DH-2000), and sunlight. To observe the change at the $SrTiO_3$ surface after being irradiated,

the surface resistance was measured by an Agilent source meter (model: B2901A, Agilent Technologies, Santa Clara, CA, USA). The setup diagram was shown in the inset of figure B.4 (a) and figure B.4 (d). For sunlight, the change under both normal and focusing conditions was also measured. A magnifying glass with 14 cm in diameter was used to focus the sunlight; the size of the partially focused spot was around 0.8 cm in diameter.
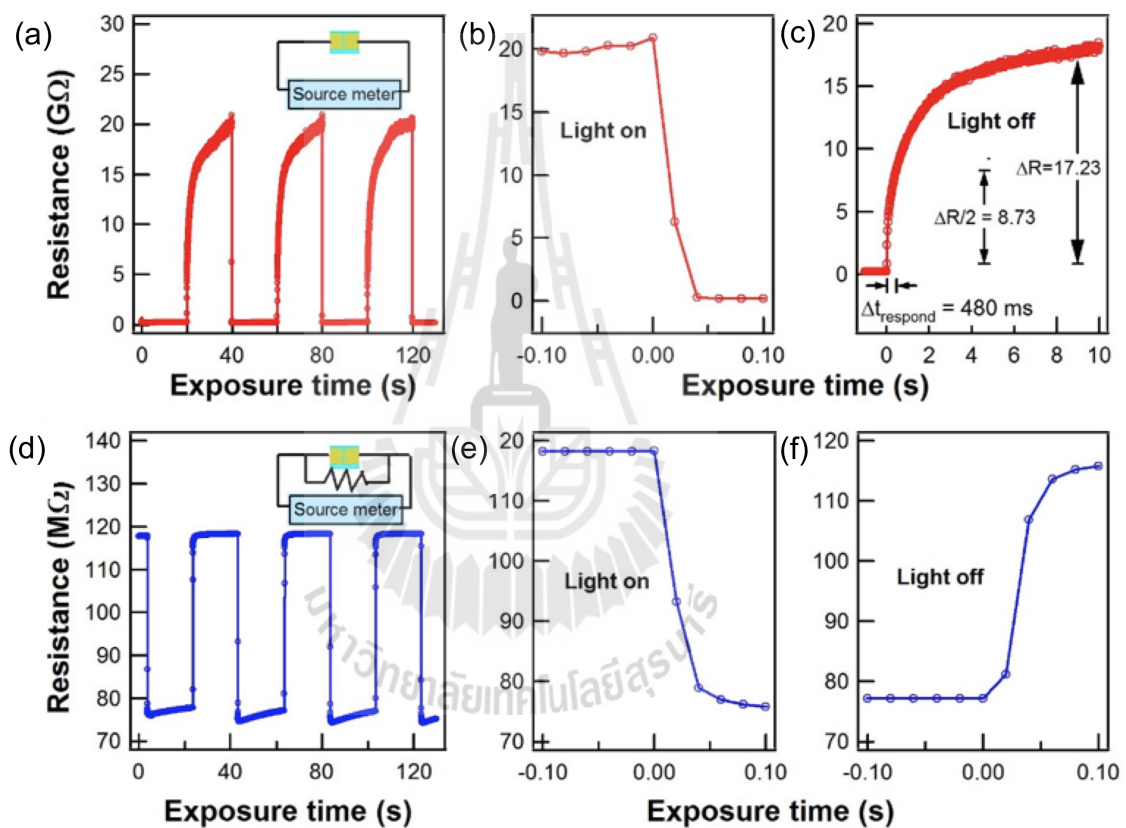
Figure B.4 a) The resistance before and after violet laser exposure on $SrTiO_3$. The inset shows measurement setup in series. (b-c) The corresponding zoom-in periods when violet laser is on and off. (d) The resistance before and after violet laser exposure on $SrTiO_3$ with 118 $M\Omega$ resistor added in parallel (see inset). (e-f) The corresponding zoom-in periods when violet laser is on and off (S. Suwanwong et al., SJST, in press).

B.2.2 Results and discussion

Figure B.4 (a) and (d) show the pronounced change in surface resistance when the sample was exposed to the violet laser with the intensity around 710 W/m^2 (measured by lux meter). The resistance is rapidly changed from around 20 GΩ to 200 MΩ after shining the violet laser and then recover back close to the original value with a slower rate after the light is off. The response time which is defined to be the period from saturated resistance to the half way were extracted to be around 11.9 ms and 480 ms after light is on and off, respectively (shown in figure B.4 (b) and (c)). With the same techniques but connected the 118 MΩ resistance in parallel to the circuit, we then have the smoother graph which can be read with the multimeter between of 70 to 120 MΩ with the response time of 14.4 ms and 24.8 ms when the light is on and off as shown in figure B.4 (d) - (f). The role of the dropping of resistance when the light was on could be caused by several effects separated by quick and slow process. The quick process may be resulted from photoconductivity (Jiang and Hasegawa, 1999) and photoelectric effect (Sorokin et al., 2007) which the resistance suddenly change after the light is on and off. The slow process could be from the oxygen vacancies generated by light exposer which last for a long time even the light is on. This effect can be proved in the change of resistance in the different oxygen partial pressure whose resistance recover slower in less pressure. Both of these effect could happen in the system, however, the oxygen vacancies seem to be the major role obtained in our researches. Besides the irradiation from the violet laser, we also irradiated the SrTiO$_3$ samples by using other various light sources, including red laser, green laser, UV LED, deuterium lamp, halogen lamp, and sunlight. The intensity spectra of these light sources as a function of wavelength by spectrometer (Model: Ocean Optics HR4000) are shown in Figure B.5 (a). The responses in resistance after turning on and off the light

sources are shown in Figure B.5 (b); note that each change in resistance along the y-axis (in log scale) was normalized by the overall intensity of each light source. The changes in resistance per overall intensity are high when using the deuterium lamp and UV LED. This suggests that the resistance change of $SrTiO_3$ is more sensitive in the UV range. The deuterium lamp has a large spectral weight of a wavelength below 387 nm, i.e. a photon energy higher than the band gap of 3.2 eV. Note that the halogen lamp also has some spectral weight of a wavelength below 387 nm but may be hard to visualize in Figure B.5 (a); this part of the spectrum could be the main contribution to the change of resistance shown in figure B.5 (b) for the halogen lamp. For the violet laser, the wavelength is around 405 nm or 3.06 eV (just below the band gap); it can be seen that the change per intensity is relatively much lower compared to the two light sources above; this corresponds quite well with the onset of the spectral response of $SrTiO_3$ (Xing et al., 2007). For the red and green lasers, the changes are much lower, at least three orders of magnitude lower compared to the UV LED, but still finite. While these finite changes should be checked further, possible reasons may be due to two photon excitation (Catalano et al., 1974) or local heating. In this research, we showed that the surface resistance of transparent $SrTiO_3$ material could be reduced largely under irradiation from various light sources, especially the deuterium lamp and UV LED. The intrinsic response times, when the light is on and off, can be different by around one order of magnitude but this difference can be adjust externally. We also show that the resistance change can also largely depend on the sunlight intensity. These results show the promise of the light-sensing application of this transparent $SrTiO_3$ material.
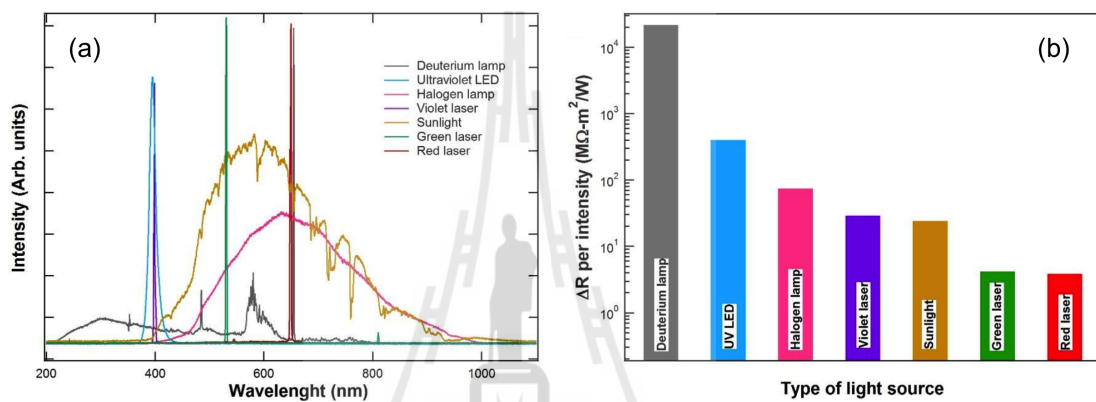
Figure B.5 (a) The intensity spectra of various light sources, including the deuterium lamp, UV LED, halogen lamp, violet laser, sunlight, green laser, and red laser as a function of wavelength (the overall intensity for each light source is adjusted to fit in the graph). (b) The responses in resistance after turning on and off the light sources; note that each change in resistance is normalized by the overall intensity of each light source (S. Suwanwong et al., SJST, in press).

APPENDIX C

PROGRAMMING

In this chapter, I would like to express the programming that can be used to communicate with the equipment, for example, the temperature controller and source meter. There are two different programs represented in this chapter: LabVIEW and C++. These two programs are very well-known and used in many industrials and facilities. Each program has its own advantages. Understanding how to use programs to operate the equipment can help in management and safety in the lab. Here, I will focus only the equipment that use the RS-232 as a communicating cable.

C.1 LabVIEW programming in low temperature measurement

LabVIEW is a system-design platform and development environment for a visual programming language from National Instruments (NI) which is widely used in many industries and organization. It has been designed for using in data acquisition and instrument control. LabVIEW is easy to learn and develop because they provide the suitable packages in wide range of equipments (i. e. Lakeshore and Agilent companies). LabVIEW consists of two man windows: block diagram which is used to write the commands and front panel which is used to interface between user and computer. Block diagram uses the graphical programming where we can simply drag and drop shortcuts (functions, variables, nodes) and wires (dataflow) in the program without codings. Figure C.1 shows the front panel used

to measure the real time temperature (Lakeshore temperature controller model 331) and resistance (Agilent B2901A) in our cryostat system.

However, because the LabVIEW is ready-made program, it is quite difficult to modify or write the new function in one program. For example, connecting many equipments in one block diagram will result to the very complex program which leads to the frequent crashing. Thus, using more controllable program would be better if we need more stable and accurate data acquisition. Hence, the C++ programming will be a good choice in this case.
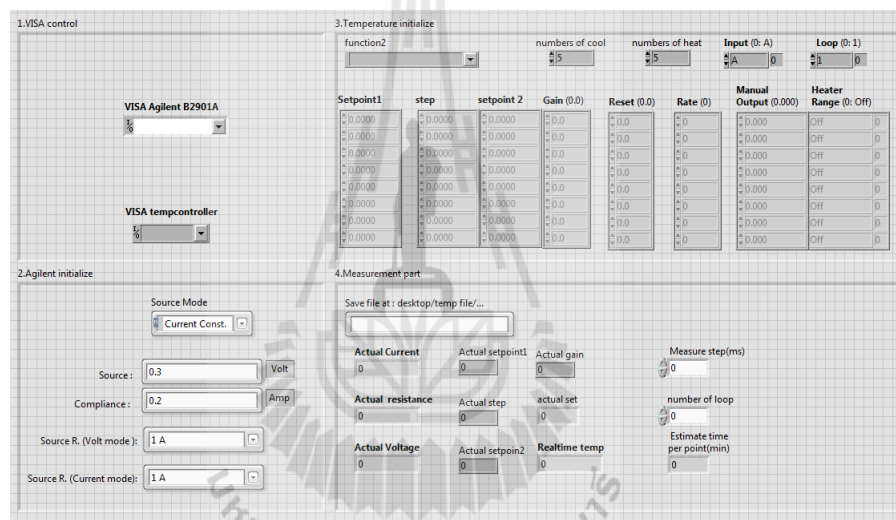
Figure C.1 Prototype of LabVIEW front panel using to measure resistance in our cryostat setup.

C.2 The C programming using to monitor the scientific instrument

The C++ program is known as a low-level programming language which allows us to manipulate the instrument from the low-level memory. There are many major implementations such as Intel C++ Compiler and Microsoft Visual

C++. Here, I used Microsoft Visual Studio 2012 which has the advantage of lots of existing libraries and available informations to develop the interface program. The windows application allows the control from user interface which is an increment of the console C++. It consists of five important parts: global definition (i.e. #include <stdio.h>), external function (i.e. void(), int()), body (i.e. static and edit boxes), process (i.e. timer and command), and main windows (i.e. size and tab control of the windows). Figure C.2 shows the Windows application to monitor the pressure and temperature written using Visual Studio 2012. This program is faster and easy manageable but required more knowledge compared with LabVIEW. Due to the advantages of the above, I would like to apply my ability in the C++ programming to use in either our low temperature system (short term) or other organisation (i. e. SLRI).
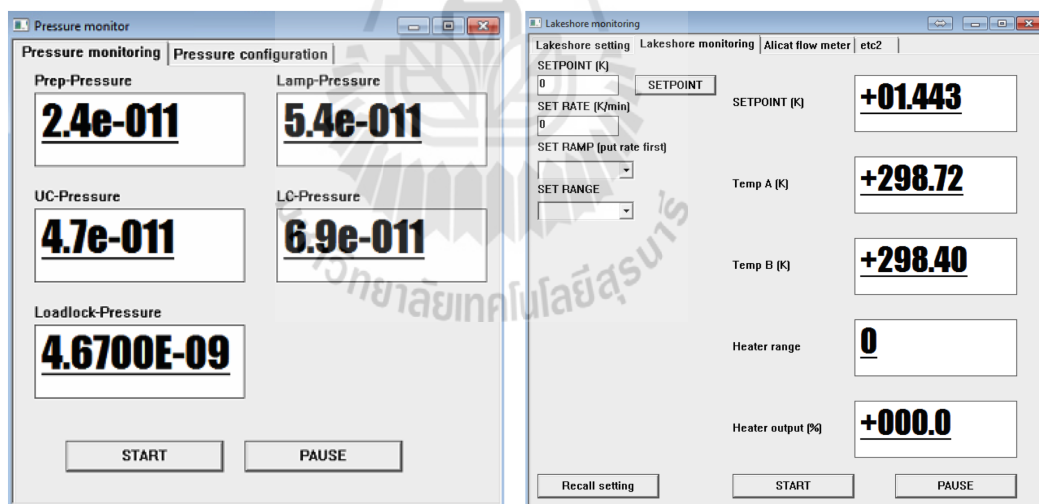
(a) Pressure monitor (b) Temperature monitor

Figure C.2 Windows application written by Visual Studio 2012 (C++) a) Pressure monitor. b) Temperature monitor.

CURRICULUM VITAE

NAME   Mr. Tanachat Eknapakul

DATE OF BIRTH   April 2, 1988

PLACE OF BIRTH   Nakhon Panom, Thailand

PERSONAL ADDRESS 79 Taneesopsant Rd., Muang District,

Nakhon Phanom 48000, Thailand

Mobile. 66-84-5101972

E-MAIL   tanachat88@gmail.com

EDUCATIONS

PhD candidate (2010 - present)

School of Physics, Suranaree University of Technology, Nakhon Ratchasima, Thailand

Title of Thesis: Study of electronic structures at the surfaces of metal dichalcogenides by photoemission spectroscopy

Supervisor: Asst. Prof. Dr. Worawat Meevasana

Bachelor of Science (2007 - 2010)

Department of Physics, Faculty of Science, Khonkaen University, Khonkaen, Thailand

Advisor: Prof. Dr. Santi Maensiri